

Aus dem Institut für Anatomie und Zellbiologie

Institut der Ludwig-Maximilians-Universität München

Vorstand: Prof. Dr. med. Christoph Schmitz

Mechanism of actin polymerization with yeast formin

**Bni1p: effect of the KCl concentration on the FH2
mediated actin nucleation**

Mechanismus der Aktinpolymerisation mit Hefeformin

**Bni1p: Effekt der Kaliumchloridkonzentration auf die
FH2-vermittelte Aktinnukleation**

Dissertation

zum Erwerb des Doktorgrades der Medizin (Dr. med.)

an der Medizinischen Fakultät der

Ludwig-Maximilians-Universität zu München

vorgelegt von

Dipl.-Chem. Hans Koss

aus

Ahlen

2012

Mit Genehmigung der Medizinischen Fakultät
der Universität München

Berichterstatter: _____

Mitberichtserstatter: _____

Dekan: Prof. Dr. med. Dr. h.c. Maximilian Reiser, FACR, FRCR

Mitbetreuung durch den

promovierten Mitarbeiter: Dr. rer. nat. Roland Wedlich-Söldner

Tag der mündlichen Prüfung: _____

Ehrenwörtliche Erklärung

Ich erkläre ehrenwörtlich, dass ich diese der Medizinischen Fakultät der Ludwig-Maximilians-Universität München zur Promotionsprüfung eingereichte Arbeit am Max-Planck-Institut für Biochemie in Martinsried unter Betreuung durch Prof. Dr. Michael Schleicher, Institut für Anatomie und Zellbiologie, Institut der Ludwig-Maximilians-Universität München, und Mitbetreuung durch Dr. Roland Wedlich-Söldner, Max-Planck-Institut für Biochemie, Martinsried, ohne sonstige Hilfe selbst durchgeführt und bei der Durchführung der Experimente und Abfassung der Arbeit keine anderen als die in der Dissertation aufgeführten Hilfsmittel oder Einrichtungen genutzt habe. Ich habe bisher an keinem in- oder ausländischen Medizinischen Fachbereich ein Gesuch um Zulassung zur Promotion eingereicht. Ich habe bisher weder die vorliegende noch eine andere Arbeit als Dissertation vorgelegt.

London, 20. Februar 2012

Dipl.-Chem. Hans Koss

Acknowledgements

I would like to express my gratitude to the following persons:

Prof. Dr. Michael Schleicher (thesis supervisor). He accepted me as a doctoral candidate and gave me the opportunity to write this thesis under his general supervision.

Dr. Roland Wedlich-Söldner (group leader at the Max-Planck-Institute for Biochemistry, Martinsried). He gave me the opportunity to perform the experiments in his laboratory. His door was literally open: He was always willing to discuss questions and proposals as they arose. I deeply appreciate the space and liberties I was given in the laboratory; that experience substantially contributed to my decision to continue working in science.

Dr. Alvaro H. Crevenna Escobar (group member). He showed me several experimental techniques, shared much of the material which I used in this work and took time to answer every single question I asked. Dr. Crevenna also gave very helpful comments on a preliminary version of this thesis.

Gisela Beck (group member). She provided unfailing technical support and was an experienced, friendly and helpful advisor, especially in cloning issues.

Felix Spira, Nils Kulak, Dr. Jerry Haochen Yu and Julia Dominguez Escobar (group members). They shared their experimental knowledge and gave me advice during cloning or protein expression attempts, and also were involved in some less project-centred hours outside the lab.

Tina Freisinger, Dr. Nikola Müller, Anoop V. Cherian and Dr. Julia Riedl (group members). They gave me helpful advice and were part of a group which generated an atmosphere in which it was a pleasure to work.

Dr. Michael Rehman (group of Dr. T. Walter). He taught me Western Blotting and gave me access to the Semi Dry Blotter.

Claudia Franke (Core Facility). She ran many test expressions and the large-scale FH2 expression. I am also grateful for the discussions on formin construct expression problems.

Dr. Sabine Suppmann (Core Facility). I thank her for the kind support and helpful discussions.

Dr. Stefan Uebel (Core Facility). He gave me partial access to the Core Facility laboratories and permitted me to use the freeze dryer.

Prof. Dr. Don Lamb (LMU Chemistry). He helped me to do parts of the experimental work during my medical studies and gave me the biophysical foundations during my chemistry studies.

Dr. Jie Li. I thank her for English language advice.

Table of contents

1	Introduction.....	- 7 -
1.1	Actin	- 7 -
1.2	Actin-binding proteins, nucleators and elongators.....	- 9 -
1.2.1	Structure and function of formins	- 13 -
1.3	Electrostatics and electrolyte conditions	- 17 -
1.3.1	Electrolyte conditions in human and yeast.....	- 17 -
1.3.2	Effect of electrostatics and electrolyte conditions on actin polymerization without and with formin.....	- 18 -
1.3.3	Other possible implications of a salt effect	- 20 -
1.4	Formins and disease	- 20 -
1.5	Drugs targeting interactions between FH2 and actin.....	- 22 -
1.6	Aim of this work.....	- 24 -
2	Results and discussion.....	- 25 -
2.1	Formin constructs for structure-function analysis of the FH1 domain	- 25 -
2.1.1	Overview	- 25 -
2.1.2	Cloning and expression of reference and control constructs	- 27 -
2.1.3	Cloning and expression of (P) _x -FH2 and (GS) _x -FH2 constructs.....	- 29 -
2.1.4	Cloning of Lifeact-FH2 and WH2-FH2	- 29 -
2.2	Effect of salt on actin polymerization with or without FH2	- 30 -
2.2.1	Overview	- 30 -
2.2.2	Effect of salt on actin polymerization in the absence of FH2	- 32 -
2.2.3	Effect of salt on FH2 mediated actin polymerization.....	- 37 -
2.3	Effect of salt on electrostatic binding free energies and calculation of solvent accessible surface areas (SASAs).....	- 46 -
3	Summary and Outlook	- 51 -
4	Experimental	- 54 -
4.1	Materials	- 54 -
4.1.1	Enzymes, proteins and chemicals.....	- 54 -
4.1.2	Kits, vectors and strains	- 55 -
4.1.3	Buffers, media and solutions	- 56 -
4.1.4	Oligonucleotides	- 62 -
4.2	Molecular cloning	- 64 -
4.2.1	General procedure	- 64 -
4.2.2	Specific technical protocols	- 66 -
4.3	Expression of formin constructs	- 70 -
4.4	Actin purification, labelling, storage and handling	- 73 -

4.5	Pyrene assays.....	- 74 -
4.6	Fluorescence microscopy	- 77 -
4.7	Calculation of electrostatic energies and calculation of solvent accessible surface areas (SASAs).....	- 79 -
5	Appendix	- 82 -
5.1	Matlab code for processing pyrene assay data.....	- 82 -
5.2	List of figures.....	- 85 -
5.3	List of tables.....	- 86 -
5.4	Abbreviations	- 86 -
5.5	Abstract	- 88 -
5.6	Zusammenfassung in deutscher Sprache	- 89 -
5.7	Curriculum vitae	- 90 -
6	References	- 92 -

1 Introduction

1.1 Actin

Actin has been discovered together with myosin in muscles as a filamentous structure in 1942 [1, 2]. Actin was found to be present in most eukaryotic cells and is highly conserved [3]. Actin filaments play key roles in cell adhesion[4], endocytosis[5], intracellular trafficking [6], maintenance of cell shape[4], polarity[7, 8] and cell motility [9, 10]. Filament building proteins with a high structural homology to actin were recently found to be present in prokaryotic systems [11].

Actin exists in a filamentous form (F-actin) and in a globular form (G-actin). F-actin is a polar polymer of G-actin with a pointed (-) and a barbed (+) end (figure 1). One filament is composed of two proto-filaments which form a right-handed double helix. The actin monomers in each proto-filament are assembled in a head-to-tail manner. G-actin is an ATPase and can exist in four different forms: nucleotide-free, ATP-bound, ADP-P_i bound and ADP-bound. Typically ATP-actin is incorporated into actin filaments because the critical ATP-actin concentration is much lower than the critical ADP-actin concentration (depending on experimental conditions) [12]. Nucleotide-free actin (NFA) has an even lower critical concentration [13]. However, the NFA concentration is normally below this critical concentration; moreover, NFA filaments are not stable without stabilizing agents.

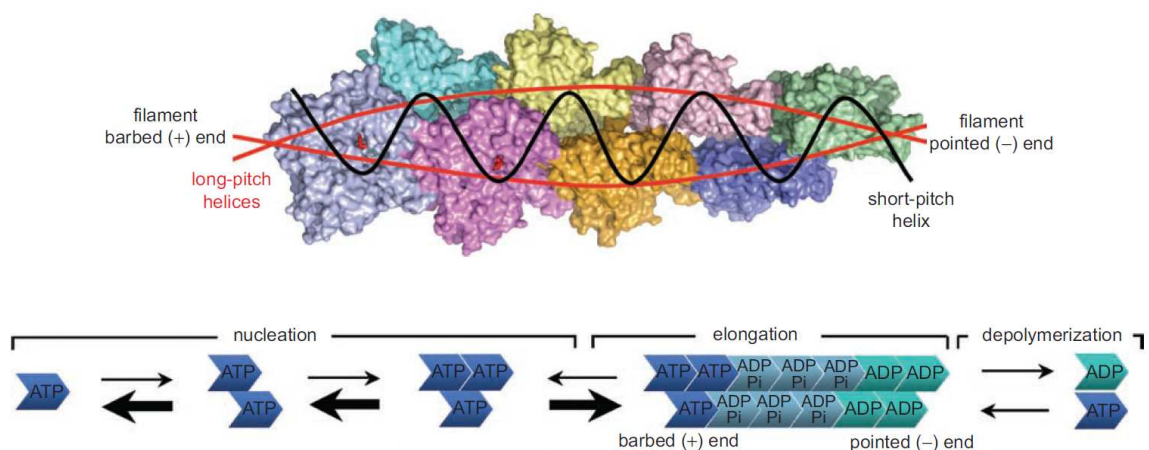


figure 1: Structure of the actin filament and actin polymerization. Top: Actin is a polar polymer composed of two actin proto-filaments. These filaments form a right-handed double helix (long-pitch helices). The actin subunits in the proto-filaments are linked in a head-to-tail manner. Bottom: The nucleation phase until the formation of actin tetramers is energetically unfavourable, while the elongation phase takes place spontaneously above a certain critical concentration. At steady state, monomers are added at the barbed (+) and removed at the pointed (-) end. This so called “tread milling” process leads to a stable filament length. Filament aging leads to transformation of ATP-actin subunits to ADP-actin subunits. From [14].

Actin polymerization kinetics follows a curve with a sigmoid-like shape (figure 30), which suggests a cooperative actin polymerization mechanism [15]. Actin polymerization can be divided into two phases: nucleation and elongation (figure 1) [16]. The nucleation kinetics is very complex [17], while the elongation phase can be described by an exponential kinetic model [18].

Nucleation includes the formation of actin dimers and trimers and is an energetically unfavourable process; the dimer formation is preceded by a lag phase. Starting with the formation of a tetramer, elongation is energetically favourable and occurs spontaneously at actin concentrations above a certain critical concentration. After reduction of G-actin due to filament growth, an equilibrium state is reached.

At typical physiological pH values, G-actin with its isoelectric point of 5.2 - 5.4 (α -skeletal muscle actin) [19, 20] is negatively charged. At pH = 7.4 it bears four negative charges. Therefore large parts of the surface are negatively charged; local extent of the charge depends on the specific amino acids present at the protein surface. Nucleation and elongation can be triggered by K^+ , Mg^{2+} or Ca^{2+} which are known to partially neutralize this surface charge [21-23]. Upon addition of salt, actin undergoes a conformational transition which enables G- to F-actin transition; a structural description of this conformational transition was proposed only recently [24]. Ca^{2+} and Mg^{2+} are thought to bind to several high- and moderate-affinity divalent cation binding sites [25]. Mg^{2+} is known to strongly promote actin nucleation, while Ca^{2+} has been linked to nucleotide exchange. Low-affinity binding sites (also for monovalent cations like K^+) are important for elongation. Critical concentrations of Ca^{2+} and Mg^{2+} for induction of actin polymerization are roughly 100 times lower than the critical K^+ concentration [22]. If the Ca^{2+} ions associated with G-actin in a solution with low Ca^{2+} concentration are replaced by Mg^{2+} ions, actin polymerization by K^+ is greatly accelerated [21]. Critical K^+ , Mg^{2+} and Ca^{2+} concentrations, which are needed for the existence of F-actin at equilibrium, have also been described [26].

G-actin can associate with and dissociate from both the barbed (+) and the pointed (-) ends of actin filaments. Dissociation constants have been measured by electron microscopy [27]. At typical actin concentrations between 0.1 μ M (75 mM KCl, 1-5 mM $MgCl_2$) [28] and 5 μ M (50 mM KCl, 1 mM $MgCl_2$), ATP-actin associates with F-actin, while ADP-actin dissociates from it [12]. ATP-actin associates faster to the pointed (+) than to the barbed (-) end. After ATP-actin association to the barbed (+) end, ATP-actin undergoes a filament aging process: ATP-actin is hydrolyzed and P_i is released, resulting in the ADP-actin form of older filament subunits. At typical G-actin concentrations the dissociation of this ADP-actin at the pointed (-) end is faster than its association. This process can therefore be described as a treadmilling process, in

which the filament grows at the barbed (+) end and shrinks at the pointed (-) end, leading to apparent movement of the filament towards its barbed (+) end. Actin association is a second order reaction depending on G-actin concentration while dissociation is rate limited. Therefore an equilibrium state with stable filament length is reached after the elongation phase due to decreased G-actin concentration.

1.2 Actin-binding proteins, nucleators and elongators

Actin dynamics *in vivo* is regulated by many actin binding proteins (ABPs). They can bind G-actin (for example profilin, cofilin, Srv2/CAP, thymosin, see below) or/and F-actin. Capping proteins are an important group of proteins binding to F-actin. They block the actin filament from both polymerizing and depolymerising by binding either to the barbed (+) end (CapZ) or the pointed (-) end (tropomodulin). ABPs of the Gelsolin family can sever actin filaments and subsequently bind to the barbed (+) end. ABPs can organize actin filaments by bundling (actinin) or crosslinking them (filament, fimbrin). They are also involved in complex tasks of f-actin organization and stabilization, as for example in muscle function (tropomyosin, myosin II). It is also possible to group many ABPs by conserved structural domains or common actin binding sites [29]. It is noteworthy that profilin and thymosin B4, which will be discussed below, bind to different actin sites; therefore, a profilin:actin:thymosin B4 complex may form under certain conditions [30].

Cofilin, a member of the ADF/cofilin family, is a side-binding ABP which destabilizes f-actin. It inserts between two ADP-actin subunits of one side of a filament, leading to a twist on the filament and instability of the filament lattice [31]. Cofilin therefore promotes depolymerization at the pointed (-) end and keeps ADP-actin out of the cycling actin pool being available for polymerization (figure 2). ADP-actin can dissociate easier from cofilin upon cofilin phosphorylation.

Profilin is ubiquitous and thymosin B4 is present in most eukaryotic cells. Thymosin B4 slows actin addition at both the barbed (+) and the pointed (-) end, while the function of profilin is more complex to describe: polymerization at the barbed (+) end can be either promoted or slowed. Several functions of these ABPs have to be considered: (1) Both thymosin B4 and profilin have, together with cofilin, an effect on actin turnover (figure 2). Thymosin B4 inhibits the exchange of ADP for ATP in G-actin. Profilin, in contrast, accelerates this actin turnover and thus promotes actin assembly. Profilin recruits ATP-actin by binding to a complex of Srv2/CAP-ATP-actin and by subsequent release of exchange factor Srv2/CAP [32]. This exchange factor Srv2/CAP has a higher affinity to ADP-Actin and binds to ADP-actin before nucleotide exchange.

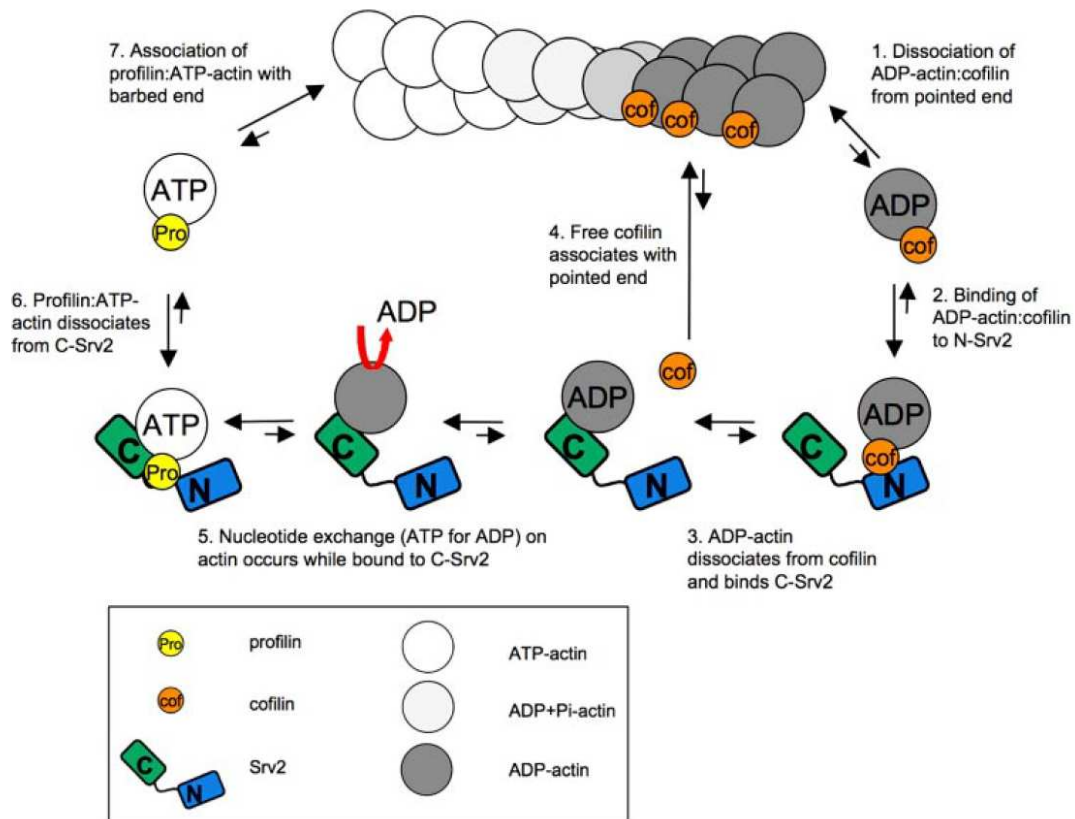


figure 2: Roles of profilin, cofilin and Srv2 in actin turnover. From [32].

(2) The interaction between the ATP-actin-profilin complex and actin monomers or the barbed (+) end is sterically hindered; the polymerization rate of profilin-ATP-actin is therefore slower than the rate of profilin-free ATP-actin. (3) Both profilin and thymosin B4 are ATP-actin monomer sequestering proteins and thus reduce the total actin pool available for polymerization of profilin-free ATP-actin. This explains the high ratio of G-actin : F-actin *in vivo*. PIP and PIP₂ can stimulate the dissociation of profilin from actin; thus profilin can be considered a transmitter of cell membrane signals to the actin cytoskeleton. (4) However, an ATP-actin-profilin complex can speed up elongation at the barbed (+) end dramatically in the presence of formin: the FH1 domain of formin proteins being bound to the barbed (+) ends of f-actin can recruit this complex (more about formins below).

Actin nucleators (figure 3) promote actin nucleation by reducing the energy barrier for the formation of actin dimers or trimers (chapter 1.1). They can either stabilize actin dimers / trimers, or they can mimic an actin tri- / tetramer and thus enable directly the energetically favourable elongation process. There exist three nucleator classes [33]:

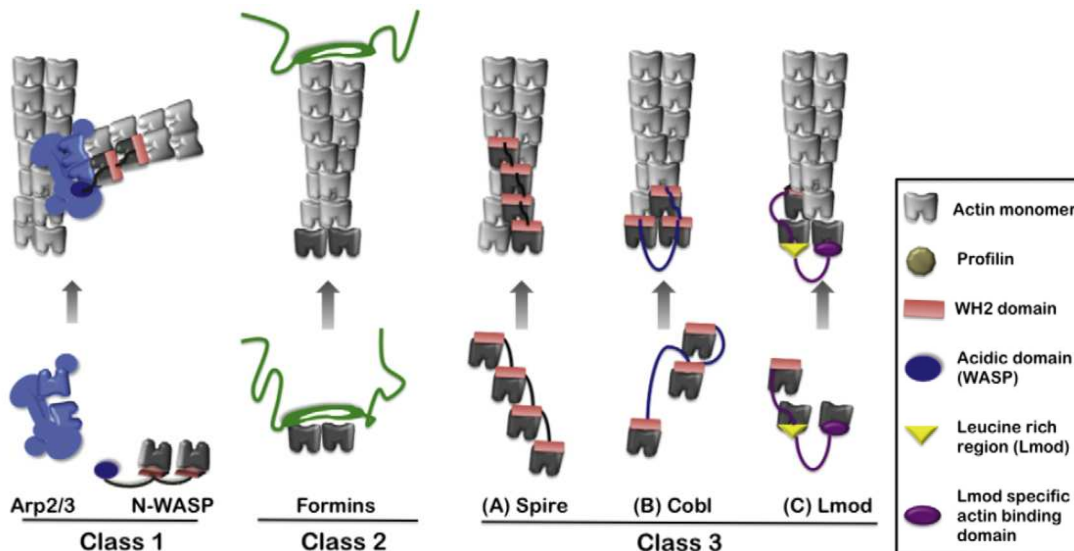


figure 3: Classification of nucleation factors. Class 1 nucleation factors need nucleation promoting factors (NPF)s like N-WASP for proper function. From [33].

Class 1: Arp2/3. These proteins nucleate actin as new side branches from pre-existing f-actin. They work together with Nuclear Proliferation Factors (NPFs), which induce conformational changes in Arp2/3 and recruit actin monomers. NPFs are WASP, NWASP, WAVE (also known as SCAR), WASH, WHAMM, JMY, Cortactin and HS1. After nucleation, Arp2/3 remains at the pointed (-) end, but is later released from aged filaments. Cofilin catalyzes this Arp2/3 and branch dissociation [31].

Class 2: Formins are known to promote actin nucleation with their dimerized FH2 domain. The FH2 dimer promotes actin nucleation[34, 35] probably by bridging two linear actin monomers, leading to the formation of unbranched actin filaments [34, 36]. The formin dimer remains associated with the barbed (+) end of the nucleated filament.

Class 3. WH2 containing proteins [33]. The WASP-homology 2 domain (WH2) domain binds G-actin. In Class 3 nucleators, at least two WH2 domains are linked. Together with recruited actin monomers, they mimic an f-actin nucleus and therefore promote actin polymerization from this nucleus. Examples for Class 3 nucleators are Spire, Cobl and Lmod.

The variety of nucleators offers the tools for a differential regulation of actin dynamics in several contexts of cellular function (figure 4).

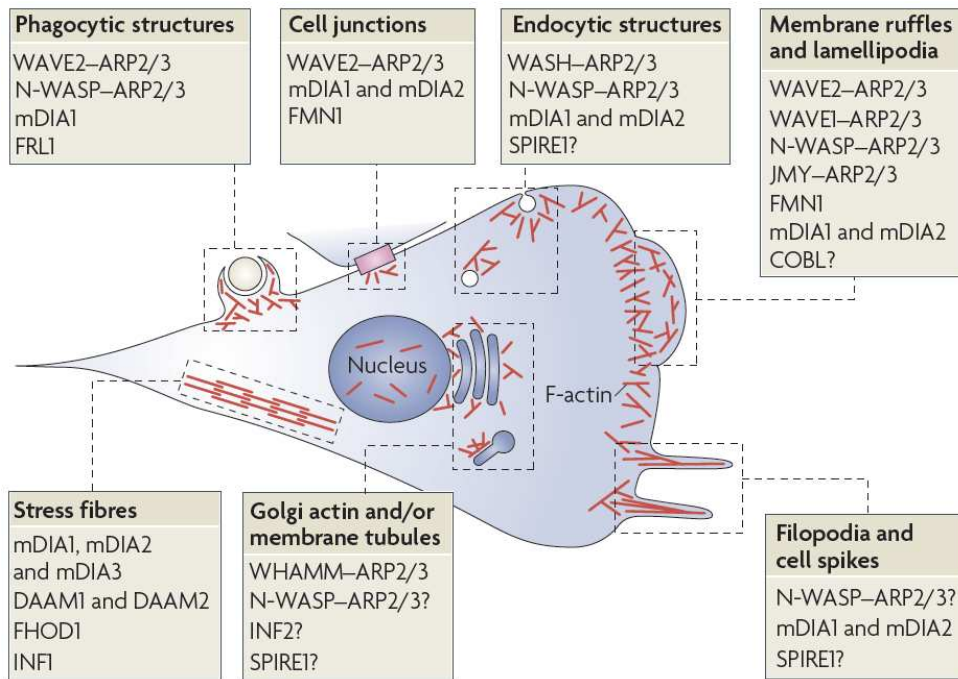


figure 4: Function and localization of f-actin and its nucleators in mammalian cells. ARP2/3 promotes filament branching and requires nucleation promoting factors (NPF)s like WASH and WAVE. *mDia1*, *mDia2*, *mDia3*, *FRL1*, *FMN1*, *FHOD1*, *INF1*, *INF2*, *DAAM1* and *DAAM2* are formins (see chapter 1.2.1). From [37].

Formins also can serve as elongators; they remain associated with the barbed (+) end during elongation. Details will be discussed in the following subchapter. Other actin elongation factors are Ena/VASP proteins; they recruit profilin-actin, similar to the formin FH1 domain [33]. Clustered VASP proteins form tetramers and can greatly accelerate elongation [38]. They exhibit only negligible nucleation activity at physiological salt concentrations [39].

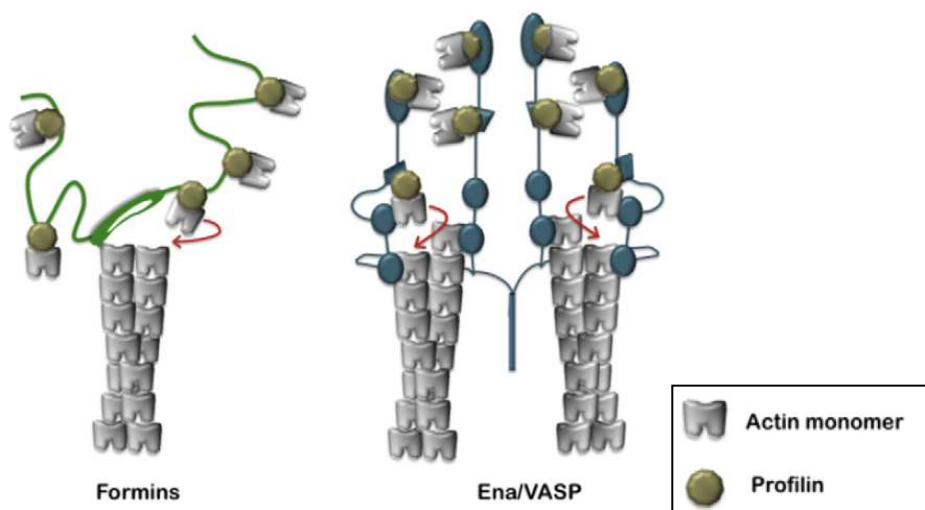


figure 5: Classification of elongation factors. Formins can also serve as nucleators (Class 2, see figure 3). From [33].

1.2.1 Structure and function of formins

The term “formins” was introduced in 1990 for a group of proteins that typically contain > 1000 amino acids encoded by different transcripts of the murine limb deformity (*LD*) gene [40]. The FH2 (formin homology 2) domain, usually 400-500 amino acids long, defines the formin family and is used for phylogenetical classification [41, 42]. Formins can be grouped into yeast formins (budding and fission yeast), plant formins, non-yeast fungi formins and metazoans. Currently the following metazoan formin classes are described: Diaphanous (DIA), Dishevelled-associated activators of morphogenesis (DAAMs), formin-related proteins in leukocytes (FRLs), formin homology domain proteins (FHODs), formins (FMNs), inverted formins (INFs) and Delphinin. About 15 different formins have been identified in mammals [37, 43]. Budding yeast expresses two formins, Bni1p and Bnr1p [44]. X-ray structures of FH2 domains of yeast Bni1p[45], human Daam1[46] and mDia1[47] show that the atomic FH2 structure is highly conserved. Therefore it is not surprising that the FH2 domain is the molecular centre of formin function. It has been shown that the FH2 domain of Bni1p alone can catalyze actin polymerization *in vitro* [48]. However, even though the atomic FH2 structures of homologous formin proteins are similar, their effect on actin polymerization varies greatly [43]. It is an open question which (minor) structural features are responsible for these (probably kinetic) differences.

The FH1 (formin homology 1) domain is less conserved than the FH2 domain [49]. However, the only known formin without a FH1 domain is ForC in *Dictyostelium discoideum* [50].

A diaphanous inhibitory domain (DID) and a diaphanous auto-regulatory domain (DAD) are part of mammalian mDia1 and mDia2 formins (figure 6). Similar domains can also be found in other formins like FRLs and DAAMs. The DID domain can interact with the DAD domain and thus block formin activity. Rho family GTPases like mammalian RhoA can bind to the formin (to the GBD) and prevent the DID from interacting with DAD, leading to the activation of formin [51]. In yeast, several GTPases including Rho1p, Rho3p, Rho4p and Cdc42p have turned out to play key regulatory roles in the spatiotemporal regulation of the actin cytoskeleton [52-54]. A dimerization domain (DD) C-terminal to the DID domain can dimerize; it is involved in autoinhibition in mDia1 [55].

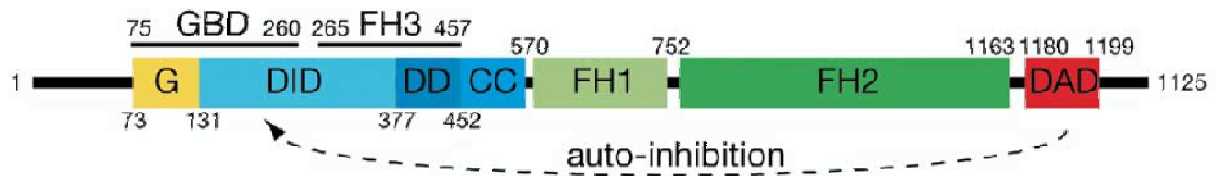


figure 6: Domains of mammalian mDia1. Domain name abbreviations: **G**: GTPase binding region for RhoA binding; **DID**: Diaphanous Inhibitory; **DAD**: Diaphanous autoinhibitory domain; **DD**: dimerization domain; **CC**: coiled coil; **FH1 - FH3**: formin homology 1 - 3; **GBD**: GTPase binding domain. GBD and FH3 are structural domains. FH3 is not established. From [56].

The FH2 domain of yeast formin Bni1p is structurally and functionally well characterized (figure 7). It is therefore a good model protein; in the following part of this subchapter, structure-function relationships of formin domains will be discussed in detail, with a focus on the FH2 and FH1 domains of yeast formin Bni1p. The dimerization of its FH2 domain is highly stable: analytical ultracentrifugation shows that the FH2 dimer is very stable even at $c(\text{NaCl})=200 \text{ mM}$ [57]. An electrophoretic mobility assay confirmed the stability of the FH2 dimer [45]. The dimerization takes place in a head-to-tail manner: The “post” subdomain of one FH2 domain interacts with the “lasso” subdomain of the other FH2 domain (figure 7). The dimer is often described as a donut-shaped ring. It was reported that truncated yeast formins (Bni1p, FH2 and FH1-FH2 constructs) can form tetramers in solution (SLS analysis) [58]. FH1-FH2 constructs of mDia1 were also found to oligomerize [59].

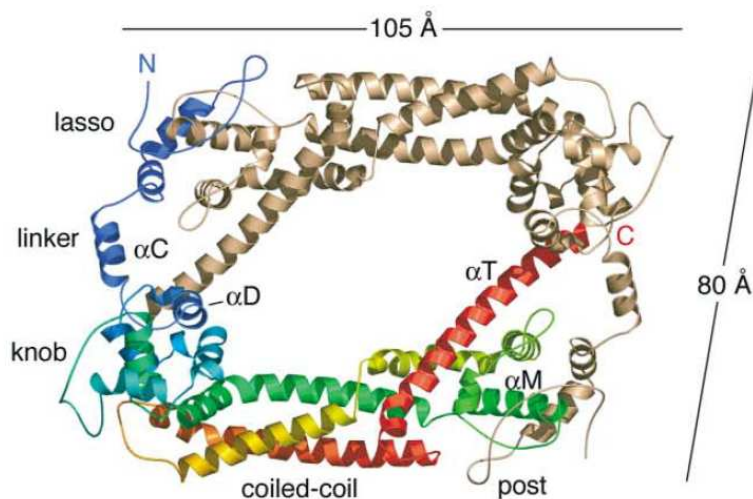


figure 7: Structure of the dimerized Bni1p FH2 domain. One of the FH2 monomers is printed in colour. The N-terminal lasso subdomain of one FH2 monomer is in contact with the C-terminal lasso subdomain of the other FH2 monomer: The dimerization takes place in head-to-tail manner. From [45].

Formins also function as elongators. The FH1 domain recruits profilin-actin and is the main elongation factor because it promotes elongation greatly. The role of the FH2 domain is ambiguous. On one hand, the FH2 domain competes with capping proteins for filament barbed (+) ends and can thereby facilitate elongation. On the other hand, FH2 domains can themselves limit the accessibility of the barbed (+) ends and thereby inhibit elongation to a variable extent [51]. During elongation, the FH2 domain is responsible for keeping the FH1 domains close to the barbed (+) end. This constant barbed end association is made possible by a processive mechanism [60, 61]: There are two different hypotheses as to how FH2 can stay at the barbed (+) end during filament elongation [62]. In the both hypotheses, the FH2 domain can adapt an “open” or a “closed” conformation. A flexible linker subdomain between the N-terminal “lasso” subdomain and the “knob” subdomain allows the FH2 dimer to adapt these conformations (figure 8). The “stair-stepping” hypothesis explains processive formin association with only two alternating states. During the closed state, the FH2 dimer is bound to three terminal actin subunits with both its knob and post sites. The trailing FH2 subunit “steps” to the end of the filament, so that its post binding site becomes exposed (“open state”); the FH2 dimer is then bound only to two actin subunits. By addition of an actin monomer, the FH2 changes to the “closed” state again. In this “stair-stepping” hypothesis, the FH2 domain “steps” off the actin filament prior to actin addition. In the other hypothesis, called “step second” hypothesis, the FH2 domain steps forward only after the actin monomer addition. The FH2 dimer is thought to be in a rapid equilibrium between two states with an energetically favourable closed confirmation or an energetically unfavourable open confirmation. In contrast to the other model, this open state is accessible already prior to the movement of the FH2 domain. Addition of an actin monomer to such an unfavourable open state leads to a third state in which the favourable closed FH2 confirmation is inaccessible; that promotes the stepping of the FH2 dimer to the end of the filament so that the closed confirmation is accessible again.

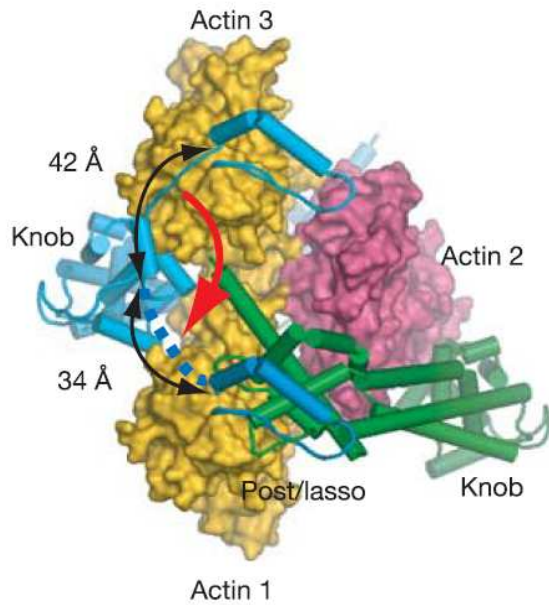


figure 8: Structure of the FH2-actin complex and flexibility of the FH2 dimer. Three actins are bound to two FH2 monomers (coloured cylinders). The flexibility of the linker between the lasso and knob region is illustrated. From [36].

The FH1 domain promotes elongation by the addition of profilin-actin to the growing barbed end [35]. Recent kinetic model for FH1FH2 mediated actin elongation might explain how excessive free profilin can slow elongation: profilin can remove actin subunits from the barbed (+) end and thus slow elongation [63]. Figure 9 shows two alternative elongation mechanisms: one FH1-dependent by addition of profilin-actin, and one FH1-independent by “classical” direct addition of ATP-actin or profilin-actin to the growing barbed (+) end.

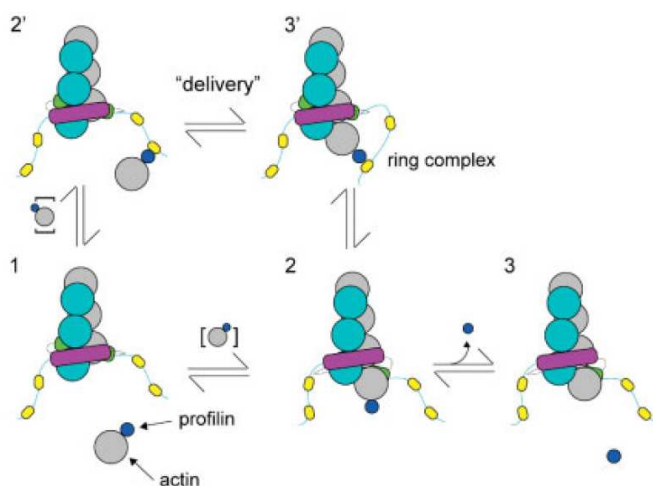


figure 9: FH1-dependent and independent actin subunit addition pathways. FH1-dependent pathway: 1-2'-3'-2-3. FH1-independent pathway: 1-2-3. F-actin substrands are coloured in light blue and grey. Actin monomer: grey. Profilin: dark blue. FH2 domain: violet. Proline-rich profilin binding sites of the FH1 domains: yellow. The FH1-independent elongation pathway can also take place in the absence of profilin. From [62].

The FH1 domain has several polyproline tracks which can bind SH3 domains of profilin. FH1 domain structure and activity varies between species. It has been shown that the number of polyproline tracks in an FH1 domain is correlated with elongation rates [48]. This number can range from one (Fus1p in *Schizosaccharomyces pombe*) to 14 (mDia1 in *Mus musculus*) [62]. It can vary within a single cell type; *Dictyostelium discoideum* has 10 formins with 1 - 8 polyproline tracks in their FH1 domains [49].

The number of prolines within one track usually also varies within and between species. For example, the four Bni1p polyproline tracks contain between 5 and 13 prolines [48]. The k_D between profilin and a polyproline depends highly on its length [64]. However, the mechanistic impact of the different polyproline track lengths within one FH1 domain is still not understood.

The FH1-dependent addition of profilin-actin to the barbed end can be governed by the FH1 domain in two kinetically distinguishable ways: On the one hand, repeated profilin-actin recruitment and release by polyproline domains could increase the local profilin-actin concentration at the barbed (+) end (diffusion limited kinetics). On the other hand, the polyproline domain could effectively deliver the profilin-actin complex to the barbed (+) end; a ring complex is formed (concentration limited kinetics) [62]. The formation of a ring complex requires flexible linkers between the FH2 domain and the polyproline track delivering the profilin-actin complex. It is not clear, how much each of these mechanisms contributes to formin function, and how sensitive formin function is to structural variations impeding or promoting these mechanisms.

1.3 Electrostatics and electrolyte conditions

1.3.1 Electrolyte conditions in human and yeast

Before discussing the impact of electrostatics and electrolyte conditions on actin polymerization, a short overview of *in vivo* electrolyte conditions in human and yeast will be given in this subchapter.

The homeostasis of intra- and extracellular salt concentrations is a central aspect in human physiology [65]. Potassium is the predominant cation in the cell, its intracellular concentration is 155 mmol/l, the extracellular concentration is 4 mmol/l. Strong deviations from this value are dangerous [66]. Sodium concentration distribution is virtually inverse: the intracellular concentration is 12 mmol/l and the extracellular concentration is about 145 mmol/l. Proteins have the by far biggest contribution to intracellular negative charge, while chloride is the predominant anion in extracellular space (120 mmol/l).

The electrolyte conditions in *Saccharomyces cerevisiae* are different because yeast is very adaptive to many conditions; variable electrolyte concentrations can be found inside the cell depending on the concentrations outside [67]. Reported intracellular concentrations depend on the strain [68, 69] and on experimental conditions. The intracellular pH value in yeast cells is usually around 6 [70]; therefore cationic ammonium is abundantly present. The most abundant intracellular metallic cation is potassium. Its intracellular concentration range was reported to be 8 - 56 mmol/100 g [67]. Therefore it is not surprising that yeast cells tolerate media with KCl concentrations from 2 μ M to 2 M [71]. Unfortunately, intracellular salt concentrations using the unit mol/l are rarely reported; the intracellular potassium concentration range that can be found in literature is 200-330mM [71, 72]. However, in a 1 M NaCl solution, intracellular potassium can drop to 92 mM, while sodium concentration rises from negligible concentrations to 283 mM [72]. Intracellular anionic concentrations can vary remarkably. A chloride concentration range reported in one publication was 11-140 mmol/100g; in the same publication, the phosphate range was mentioned to be 40-65 mmol/100g; other quantitatively important ions were sulphate and magnesium [67].

1.3.2 Effect of electrostatics and electrolyte conditions on actin polymerization without and with formin

Dissociation and rate constants are essential for modelling the kinetics of the actin polymerization process [63]. The determination of rate constants and dissociation constants was useful for evaluation of specific interactions, which have been discussed to take place during actin nucleation (study in the absence of formin) [17].

Kinetics and thermodynamics of molecular interactions are related by the equation

$$[1] \quad \Delta G_b = RT \ln(K_D) = RT \ln\left(\frac{k_-}{k_+}\right)$$

ΔG_b is the binding free energy. A major part of the binding free energy is the electrostatic binding free energy. For example, the interaction of two oppositely charged protein surfaces is often favourable because of a negative electrostatic binding free energy. The electrostatic binding free energy of a protein complex depends on the interactions of the protein complex and on the electrostatic part of the solvation energy: A reduced total protein surface implies less interaction between the solvent and the proteins. Therefore the interaction of oppositely charged protein surfaces is not necessarily favourable in terms of the electrostatic binding free energy.

The salt concentration can have an impact on electrostatics; salt can cover protein surfaces and effectively reduce their charge. It can change the electrostatic part of the solvation energy likewise. In order to understand the impact of electrostatics on actin polymerization it is therefore necessary to investigate the impact of electrolytes on actin polymerization.

The electrolyte conditions in *S. cerevisiae* can vary remarkably, as mentioned in the previous subchapter. An impact of salt on actin polymerization *in vitro* would therefore almost certainly have consequences *in vivo*. Electrostatics of actin polymerization in the absence of formin has been studied extensively: electrostatics plays an important role in the actin nucleation mechanism (without formin) [17]. However, a salt effect in terms of a change of nucleation kinetics has been observed only for very low or very high KCl concentrations. The KCl-triggered actin polymerization speed in the absence of formin is constant at $20 \text{ mM} < c(\text{KCl}) < 150 \text{ mM}$, provided that Mg^{2+} ions are present [21, 22, 73]. Below the critical concentration $c(\text{KCl}) = 10 \text{ mM}$, there is practically no actin polymerization observable [26]. Instead, aggregates of ATP-actin appear at $c(\text{KCl}) = 7.5 \text{ mM}$; they are different from the nuclei needed for the formation of F-actin [74]. Above 150 mM, the actin polymerization becomes slower with increasing KCl concentration. There is a pronounced pH effect on actin polymerization in the absence of formin: a lower pH accelerates actin polymerization [21, 25]. The pH effect was explained (for $6 < \text{pH} < 8$ only) with the stabilization of dimers and with the induction of the salt-induced conformation by protons [25]. In this context, it could be worth considering the recently published structural description of the conformational transition from G- to F-actin [24]. An effect of temperature on actin polymerization has also been reported [75].

The effect of electrostatics on formin and FH2 function has not been investigated yet. A salt effect on formin mediated actin polymerization would imply that electrostatic forces are mechanistically important for formin function in actin polymerization. Experiments taking advantage of a salt effect could furthermore be used for the validation of thermodynamic and kinetic models of specific formin-mediated actin polymerization steps.

Experiments addressing the presence or absence of a salt effect on FH2 mediated actin polymerization will be performed in this work. Moreover, electrostatic energies will be calculated by the Poisson Boltzmann equation. Such calculations could support the (non)impact of electrostatics and salt concentration on FH2 function.

1.3.3 Other possible implications of a salt effect

Apart from the impact of electrolyte conditions on formin mediated actin polymerization via electrostatics, there would be other important implications arising from a salt effect on formin mediated actin polymerization.

- A salt effect could partially explain structural and functional differences of formin proteins - in particular of the FH2 domain - between organisms.
- A regulator like salt is often more readily available than a protein. The energy spent for synthesis of a regulatory protein and the energy needed for protecting its genetic material from damage would be saved. Salt would be a reasonable regulator for a complex salt regulating system via modulation of formin mediated actin polymerization: Regulation of ion uptake and output in yeast involves several channels and even transport systems [68, 71, 76, 77].
- If salt has an impact on the function of yeast formin, it might also have an impact on *in vitro* research and could help to explain different results yielded from *in vitro* and *in vivo* experiments [78].
- For discovery of specific drug inhibitors of the FH2 domain (chapter 1.5), knowledge about the presence or absence of a salt effect is crucial.

1.4 Formins and disease

In order to evaluate the possible role of formins in human disease, the different critical functions of formins in mammals have recently been reviewed and linked to more or less specific disease mechanisms by DeWard et al (specific associations of human formins: table 1) [79]. Defects in cytokinesis can contribute to cancer genesis [80]. Formins play a key role in cytokinesis because they organise the contractile actin ring during cell division [41] and they stabilize microtubules [81] during cell division. Formins probably also play an important role in cancer cell migration and invasion [82]: mDia1 is involved in polarization and migration of cancer cells and is regulated by Rho GTPases [52, 83]. It also takes part in focal adhesions of migrating cancer cells [84]. The involvement of mDia2 in cancerous processes is less established, but more specific [79]. mDia2 seems to prevent membrane blebbing by control of cortical actin assembly [85, 86]. Blebbing is part of the amoeboid migration mode and a related microvesicle formation process of prostate and cervical cancer cells. A recent study provides evidence that mDia2 is involved in the genesis of murine and human metastating prostate cancer based on these mechanisms [87].

table 1: Specific associations of human formins to disease. Modified from [79].

Name	Chromosome	Disease relevancy
mDia1 / <i>DIAPH1</i>	5q31	5q- Myelodysplastic syndrome DFNA1 non-syndromic deafness
mDia2 / <i>DIAPH3</i>	13q21.2	Chromosome deletion in metastatic prostate cancer
mDia3 / <i>DIAPH2</i>	Xq21.33	Premature ovarian failure
FMNL1	17q21	Increased expression in lymphoid malignancies and peripheral blood leukocytes from CLL patients
FMNL2	2q23.3	Increased expression in colorectal cancer

From a pathophysiological perspective, cellular migration and adhesion are important for other processes than cancer as well. Macrophage migration, cell spreading and lamellipodia formation are influenced by the Formin-related gene in leukocytes (FRL) protein, another formin [88]. In light of this finding, it is of interest that the expression of FMNL-1, a protein of the FRL group, is elevated in blood leukocytes from CLL patients and in human lymphoid cancer cell lines [89]. Another formin, mDia1, seems to be involved in T cell development, proliferation and emigration [79]. Similarly, mDia1 also plays a role in neutrophil migration and activation [90]. Other processes in the hematopoietic system in which formins reportedly play a role include the enucleation of maturing erythrocytes [91] and actin assembly in activated thrombocytes [92].

Hematopoietic diseases, in which the involvement of mDia1 is discussed very specifically, are the myelodysplastic syndromes (MDS) del(5q). Myelodysplastic syndromes are a heterogeneous group of bone marrow diseases associated with an ineffective haematopoiesis in terms of quantity and quality, peripheral cytopenia, cell-rich dysplastic bone marrow, and oftentimes presence of blasts [93]. MDS del(5q) are low-risk variations of MDS according to the International Prognostic Scoring System (IPSS) [94]. 5q deletions similar to those of MDS del(5q) can also be found in related proliferative disorders, including variations of acute myeloid leukaemia (AML), myeloproliferative neoplasms (MPN) and overlap syndromes. Lenalidomide, a derivative of thalidomide, is effective particularly in MDS del(5q) [95]. MDS del(5q) is characterized histopathologically by an increased presence of megakaryocytes. mDia1, which is coded by *DIAPH1* on chromosome 5q, was found to be less expressed in mice with MDS del(5q) [96]. In the same publication, it is reported that Δ mDia1 knockout mice showed a marked increase in haematopoietic progenitor cells and other symptoms accounting for a role of mDia1 in MDS del (5q). Together with the knowledge of Rho GTPase dependent mDia1 activity and some other nearby deletions, a comparatively detailed mechanism for pathogenesis of this disease has been

proposed. The involvement of Rho GTPases is corroborated by the finding that additional knockout of RhoB leads to a more severe disease [97].

In order to discuss the role of formins in developmental disorders, it is useful to briefly recall their role in key cellular processes. The role of mDia1 and mDia2 has been discussed in the context of cancer in the beginning of this subchapter. Another formin being an important candidate for human developmental disorders is the dishevelled-associated activator of morphogenesis-1 (DAAM1). The formins Fmn1-IV and dDia2 are non-human analogues of this protein. The importance of these proteins for cellular migration and adhesion has been demonstrated [98, 99]. A defect in Fmn1-IV, for example, ultimately leads to kidney aplasia in mice [100]. Initially, *Fmn* (formin) genes were discussed as candidates being responsible for an observed limb deformity in mice [40]. It turned out later that in fact the *Gremlin* gene accounted for this defect [41]. However, a very rare human syndrome, which was claimed to be related to the limb deformity disorder, but might in fact be related to the Fmn1-IV defect in mice, is the severe Acro-Renal-Uterine-Mandibular syndrome [101].

Few specific human developmental disorders related to formin dysfunction have been identified until now. In a population with autosomal dominant non-syndromic deafness (DFNA1) a frameshift in the *DIAPH1* gene was observed; this leads to the expression of a truncated mDia1 protein [102]. Due to the truncation of the C-terminal part of mDia1 and possible interruption of the DAD-DID interaction, a gain-of-function mechanism can be considered. Premature ovarian failure (POF) may be related to a breakpoint in the gene of mDia3 [103]. However, experimental proof for this hypothesis is still lacking. Actin skeleton defects in oocytes might, for example, be studied with methods allowing the undisturbed observation of actin filaments *in vivo* [104].

1.5 Drugs targeting interactions between FH2 and actin

In recent years, the development of inhibitors targeting actin nucleators and elongators has made progress [105]. Those inhibitors can, as a first step, find application in experimental research. With a growing number of known nucleators and elongators, they could help to understand the complex system of actin nucleators and elongators, especially under *in vivo* conditions. However, the development of drugs targeting protein-protein interactions is a challenging task [106, 107]. Binding of drugs to active centres of enzymes is often stronger than to protein-protein interaction sites. Protein-protein interaction sites are often large, with low interaction energies (“anchors”) [108]. According to the “rule of five” [109], the size of a drug is limited because a high molecular weights reduces its bioavailability.

The Arp2/3 complex can be inhibited by CK-666 and related compounds [110]. Small molecules have been also been developed for the inhibition of formin-mediated actin polymerization (figure 10). The “Small molecule inhibitor of formin homology 2 domains” (SMIFH2) inhibits the FH2 domain of diverse formins, namely mDia1, mDia2, Bni1p, Fus1, Cdc12p and CYK-1 [111]. The compound has undergone several tests including *in vivo* experiments and is commercially available. It interrupts the interaction between actin and the FH2 domain. Interestingly, it could be confirmed that the compound probably interacts with the FH2 domain and not with actin. However, due to lacking specificity, the compound is far from any medical application [112]. In another recent study, two other compounds and their derivatives were found to block FH2 activity [113]. Studies were performed *in vitro* only. One of the two main compounds (Beryllon II, figure 10.b) was found to inhibit mDia1, mDia2 with an $IC_{50} \leq 0.5 \mu\text{M}$, and mDia3 with an IC_{50} of only $3.1 \mu\text{M}$. The other compound (figure 10.c) was found to inhibit mDia1 and mDia2 with an IC_{50} of $2.1\text{-}2.2 \mu\text{M}$, while mDia3 was not inhibited. It also inhibited INF2 and FRL1 with less affinity.

It is of interest to understand how these drugs bind to FH2 domains, which has a known atomic crystal structure. Better functional understanding of these FH2 domains and more structural knowledge about their interactions with actin would help to make informed speculations about molecular interactions of FH2 domains that have no atomic structure available. Those speculations might be possible because the secondary and atomic FH2 structures of different FH2 homologues seem to be similar [46, 47]. Together with knowledge about the interaction of small molecule inhibitors with the FH2 domain, it could be possible to rationally develop inhibitors of specific formin isoforms. By the time these inhibitors are developed, several clinical applications might be within sight. The concept of multidrug targeting [114] might find application to increase drug specificity; for this approach, detailed understanding of protein and drug interactions will be required again. For *in vitro* drug discovery and for understanding the binding properties of the FH2 surface, it is important to know how salt influences the electrostatic properties and the function of the FH2 domain.

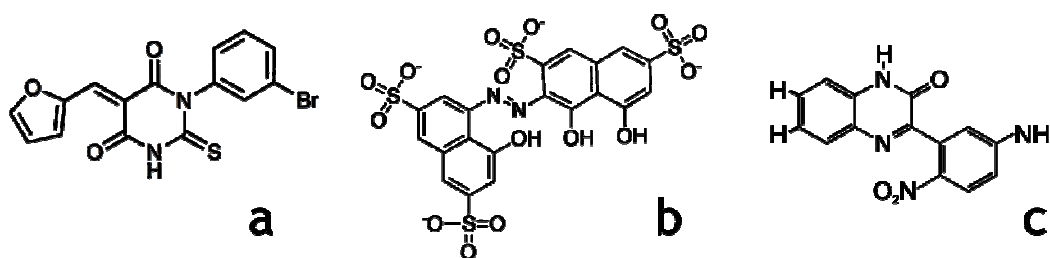


figure 10: Inhibitors of formin-mediated actin polymerization. All compounds were found to inhibit FH2. a. SMIFH2, modified from [111]; b. Beryllon II, modified from [113]; c. another inhibitor from the same study.

1.6 Aim of this work

The aim of this work is to understand formin structure-function relationships better. *In vitro* experiments should be based on cloned and expressed constructs derived from yeast Bni1p (*Saccharomyces cerevisiae*).

1. The FH1 domain typically contains polyproline tracks. The size and number of tracks differ between and within species. The linker length between the tracks is also variable. In this work, different constructs containing the structurally well-characterized FH2 domain and a tailor-made FH1-like linker and polyproline track should be cloned and expressed. Their linker and polyproline track length should be varied. If the constructs can be expressed, pyrene and TIRF assays could be used to experimentally investigate the influence of polyproline track length and linker length on formin function. The constructs should be suited for mathematical modelling so that an experimental evaluation of mathematical models of both diffusion and concentration limited actin polymerization kinetics is possible.

2. The impact of salt concentration on FH2 function should be addressed in this work. A construct containing only the structurally well-characterized Bni1p FH2 domain will be cloned and expressed. The expressed protein will be subject to biophysical experiments (pyrene assays, epifluorescence microscopy) in order to investigate the presence or absence of a salt effect on FH2 function on actin polymerization. A salt effect would account for a major role of electrostatics in the interaction between FH2 and actin. Electrostatic interaction between FH2 and actin will therefore also be addressed computationally for different KCl concentrations: Electrostatic binding energies will be calculated and the electrostatic surface potential will be visualized. The FH2 domain has recently become a target for inhibitors of formin mediated actin polymerization. An area of actin-FH2 interaction, which might be sensitive to a salt effect, will be identified. Such area might also be sensitive to inhibitors if these inhibitors turn out to interfere with the electrostatic protein-protein interaction between FH2 and actin. In order to evaluate whether the identified area is a good protein-protein inhibitor binding site candidate, solvent accessible surface areas (SASA) will also be calculated.

2 Results and discussion

2.1 Formin constructs for structure-function analysis of the FH1 domain





2.1.1 Overview

All constructs to be cloned and expressed contain the functionally important Bni1p FH2 domain. Most constructs should also contain one polyproline track or variations thereof. The linker between the FH2 domain and the polyproline track should be tailor-made. The linker and polyproline track length should be varied. It was intended to perform pyrene and TIRF assays with the expressed constructs to analyze the effect of these structural variations on formin function. All constructs will be HIS-tagged.







The cloning / expression constructs (figure 11) can be grouped into

- (1) Reference and control constructs: These constructs equal to a FH2 domain with or without a truncated Bni1p FH1 domain. A construct very similar to the FH2 construct was reported in literature (1349 - 1766, also HIS-tagged) [48]. The crystal structures of similar constructs were reported (1Y64 [36] residues 1327-1769 in complex with actin, 1UX5 [45] residues 1350-1760). The 1228-FH1FH2 (Bni1p residues 1228-1769) and the 1312-FH1FH2 construct were both reported in literature before and used for functional studies [48]. Construct 1321-FH1FH2 is similar to 1312-FH1FH2, but more comparable to other constructs of in this work.
- (2) $(P)_x$ -FH2 constructs: These constructs contain one polyproline domain ($4 \leq x \leq 14$), connected to the Bni1p FH2 domain. They should be used in order to study the impact of polyproline track length on formin function. $(P)_x$ -FH2 constructs would be good candidates for biomathematical modelling: The interaction of polyproline with profilin has been quantitatively described [64].
- (3) $(GS)_x$ -FH2 constructs: These constructs contain one polyproline domain with 6 prolines, connected to the Bni1p FH2 domain with a $(GS)_x$ linker of variable length ($3 \leq x \leq 15$). They should be used in order to study the impact of linker length on formin function. It is possible to model the $(GS)_y$ linker with a wormlike chain model [115]. Therefore development of biomathematical models in order to fit the results should be possible.
- (4) Other constructs: Lifeact-FH2 and WH2-FH2. Lifeact[116] and WH2 both bind actin, therefore the target proteins Lifeact-FH2 and WH2-FH2 might mimic FH1-FH2, in which FH1 binds profilin-actin (and not actin).






Reference and control constructs:

Construct	expected amino acid sequence	exp. MW	
success			
FH2	MQIKSAV(...)	51.42590 kDa	
1321-FH1FH2	MPPAPPMPASQIKSAV(...)	52.40314 kDa	
1312-FH1FH2	MLSSTDGVI PPAPPMPASQIKSAV(...)	53.26309 kDa	
1228-FH1FH2	MLSTQSSVLSSQPPPPPPPPVPAKLFGESLEKEKKSDDT VKQETTGDSPAPPPPPPPPPMALFGKPKGETPPPPPLPS VLSSTDGVI PPAPPMPASQIKSAV(...)	61.89731 kDa	



(P)_x-FH2 constructs

Construct	expected amino acid sequence	exp. MW	
(P) ₄ -FH2	MPPPPASQIKSAV(...)	51.97255 kDa	
(P) ₆ -FH2	MPPPPPPASQIKSAV(...)	52.16679 kDa	
(P) ₈ -FH2	MPPPPPPPPASQIKSAV(...)	52.36103 kDa	
(P) ₁₀ -FH2	MPPPPPPPPPPASQIKSAV(...)	52.55527 kDa	
(P) ₁₂ -FH2	MPPPPPPPPPPPPASQIKSAV(...)	52.74951 kDa	
(P) ₁₄ -FH2	MPPPPPPPPPPPPPPASQIKSAV(...)	52.94375 kDa	

(GS)_x-FH2 constructs

Construct	expected amino acid sequence	exp. MW	
(GS) ₃ -FH2	MPPPPPGSGSGSQIKSAV(...)	52.44101 kDa	
(GS) ₆ -FH2	MPPPPPGSGSGSGSGSQIKSAV(...)	52.87340 kDa	
(GS) ₉ -FH2	MPPPPPGSGSGSGSGSGSQIKSAV(...)	53.30579 kDa	
(GS) ₁₂ -FH2	MPPPPPGSGSGSGSGSGSGSQIKSAV(...)	53.73818 kDa	
(GS) ₁₅ -FH2	MPPPPPGSGSGSGSGSGSGSQIKSAV(...)	54.17057 kDa	

other constructs

Construct	expected amino acid sequence	exp. MW	
Lifact-FH2	MMGVADLIKKFESISKEEASQIKSAV(...)	53.49032 kDa	
WH2-FH2	MSGKAALLDQIREGAQLKKVEQNASQIKSAV(...)	54.07697 kDa	




<p>FH2 region: highlighted yellow</p> <p>Linker region: highlighted cyan</p> <p>Polyproline track: highlighted green</p>	<p> cloning + expression successful</p> <p> only cloning successful</p> <p> cloning + expression not successful</p>
--	--

figure 11: Cloning and expression of formin constructs in this work.

All constructs but Lifact-FH2 and WH2-FH2 were cloned successfully (figure 11). However, the FH2 domain is the only protein successfully expressed in this work; it was needed for the experiments to investigate a salt effect on FH2 (chapter 2.2). Without the expression of the other construct, studies on the effects of FH1 structure variations on formin function are not possible. In the next part of this chapter, expression results will be discussed further.

2.1.2 Cloning and expression of reference and control constructs

30.8 mg of FH2 protein were successfully expressed using only a part of the available biomass for lysis and purification. Final concentration was 2.80 mg/ml at a purity of 98%. The expected mass in LC-MS was 51424.6 D, the measured mass was 51424.1 D. FH2 was subsequently used in pyrene assays confirming the functionality of the protein.

Attempts to express 1321-FH2, 1312-FH2 and 1228-FH2 failed largely. 1312-FH2 (one polyproline track) and 1228-FH2 (entire FH1 domain) have been successfully expressed in literature [48]. With the same conditions described therein [48, 61, 117] expression was not successful in this work.

The specific *E. coli* BL21 Codon Plus DE3 RP strain with a FH2 construct in a PQE-70 vector, which was successfully used by the core facility to produce FH2 protein, was used as a control for own test expressions. This control was positive (figure 12) in a Western Blot (“own test expression” protocol in chapter 4.3) (figure 12). This FH2 construct underwent extensive cloning procedures including cloning into another substrain (again *E. coli* BL21 DE3 CodonPlus RP). The protein expression level was extremely low without and with induction, as shown in the Western Blot (figure 12). The expression of the derived 1312-FH2 construct was also very low, but the band showed the correct molecular weight, which is slightly higher than the molecular weight of FH2.

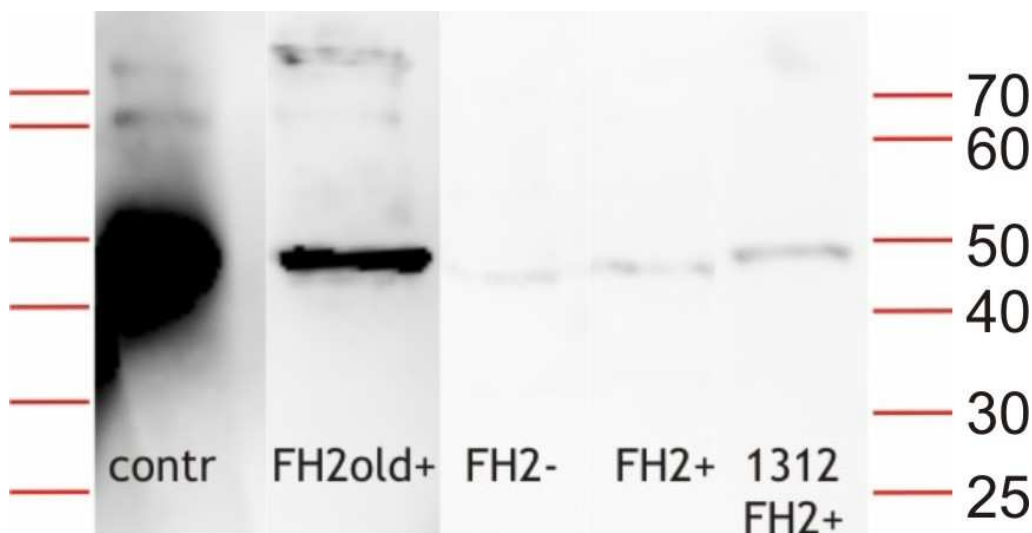


figure 12: Western Blot of a formin test expressions. Primary antibody: Mouse anti-HIS. Sizes in kDa. Only selected lanes are shown (reshuffled), marker bands are drawn, based on markings in the membrane. **contr:** purified, functional FH2 protein. **FH2old+:** control, expressed from the original culture which was used for larger scale expression. **FH2-:** non-induced, new culture. **FH2+:** induced, expressed from new culture. **1312 FH2+:** induced 1312-FH2 construct, expressed from new culture.

Sequencing results rule out a mutation within the constructs. Some constructs show a weak band (figure 12) of the correct molecular weight Western Blotting. This means that the construct itself is not erogenous.

In some attempts, another strain (E. coli BL21 Codon Plus RP, i.e. non-DE3) was used because expression of the GOI in the PQE-70 vector is driven by a non-T7 promoter. For other tried conditions see chapter 4.3.

One arising hypothesis concerned the high number of prolines in the beginning of the constructs. Bases -4 - +37 are particularly sensitive to secondary structure formation by mRNA [118]. A high amount of G and C bases (by which proline is coded) is particularly unfavourable (personal communication by Sabine Suppmann and Louise Rafty, DNA2.0, Menlo Park, CA 94025, USA). However, in construct 1312-FH2, the GC content is only 41 % until base 28 and 54% until base 37. This construct and proline-rich 1228-FH2 have both been expressed by other groups successfully [48]. Moreover, even the proline-poor FH2 construct (figure 12) was not always successfully expressed in test expressions performed in our lab or by the Core facility.

For future expression of the constructs, the following aspects should be considered:

- The group that developed the expression protocols on which this work is largely based recently switched from using HIS-tagged to Maltose-binding-protein tagged FH2 constructs (personal communication Dr. Kovar). This accounts for an unspecific problem grounded in a limited ability of the E. coli BL21 CodonPlus RP strain to express HIS-tagged formin constructs in PQE-70 vectors. The GOI could be amplified by PCR and subsequently used for SLIC in order to test other tags, including maltose-binding tags. All constructs share the same 3' end, and many have a similar sequence at the 5' end so that the number of primers for SLIC cloning would be limited.
- A mutation in the PQE-70 vector was in discussion as a reason for the occurring problems. However, expression of the 1228-FH2 construct (entire FH1 domain) also had failed. Cloning of this construct was entirely independent of the other experiments; therefore it is unlikely that a mutation in the PQE-70 vector is the reason for expression problems. However, the GOI could be transferred into a new PQR-70 vector.
- The "successful" E. coli BL21 substrain could be stripped of the PQE-70 vector with the FH2 construct (using only Chloramphenicol). Then, another PQE-70 vector with the construct of interest could be transformed into the substrain.

2.1.3 Cloning and expression of (P)_x-FH2 and (GS)_x-FH2 constructs

Cloning of (P)_x and the (GS)_x constructs was successful, while expression was not (for a discussion see chapter 2.1.2).

In addition, a “batch” cloning experiment was performed successfully: Different (P)_x and (GS)_x constructs have been generated simultaneously by using a mix of different annealed primer pairs. Interestingly, nearly all possible constructs appeared (in different colonies) on plate. In order to determine the nature of a specific colony on a plate, sequencing was necessary; sequencing of multiple colonies is, however, necessary in any case. The purpose of these experiments was to find a simple way to later generate mixed (P)_x(GS)_y-FH2 constructs in a simple batch way.

The specific procedure would be a two-piece ligation: Digest several (GS)_y-FH2 constructs with SphI and XmaI. Keep the vector, remove the small fragment. Ligate the vector with annealed primer pair (ccc)_{x-1}c / ccggg(ggg)_{x-1}catg.

The obtained construct would then be:

5'→3': (...)gcatg|(ccc)_{x-1}c|ccgg(*tc*gg)_{y-1}|gtcccAAATCAAATCAGCTGTAA|CtagtCC(...)

3'→5': (...)c|gtac(ggg)_{x-1}gggcc|(*ag*cc)_{y-1}cag|ggTTTAGTTTAGTCGACATTGatc|aGG(...)

Its translation is: M(P)_x(GS)_yQIKSAV(...)

The GOIs are the same at the beginning and at the end of the construct (exception: very small polyproline tracks), therefore these constructs would be good candidates.

2.1.4 Cloning of Lifeact-FH2 and WH2-FH2

Neither Lifeact-FH2 nor WH2-FH2 could be cloned. Numerous cloning attempts always resulted in mutations, typically leading to a stop codon within the region coding the FH2 domain. A very low constitutive expression level of Lifeact-FH2 and WH2-FH2 might be lethal or highly unfavourable for E. coli. A constitutive expression of constructs was also observed in test expressions of FH2, even upon addition of glucose in order to reduce “leakiness” of the PQE-70 vector.

The stop codon was behind the WH2 and Lifeact genes; the expression of these peptides alone is obviously not lethal. The FH1-FH2 construct and the FH2 construct alone are not lethal for E. coli: Only the spatial or functional proximity of the FH2 domain and the WH2 resp. Lifeact domain seems to be highly unfavourable. It could be speculated about an interaction of WH2-FH2 or Lifeact-FH2 with a bacterial actin analogue.

2.2 Effect of salt on actin polymerization with or without FH2

2.2.1 Overview

The impact of salt concentration on FH2 function will be addressed in this chapter. A construct containing only the structurally well characterized Bni1p FH2 domain was cloned and expressed (see chapter 2.1.2). Pyrene assays and fluorescence microscopy were performed at different KCl concentrations.

In a first step (chapter 2.2.2), actin polymerization experiments were performed in the absence of FH2 in order to confirm that there is no salt effect on actin polymerization present at a salt concentration range between 20 mM $\leq c(\text{KCl}) \leq$ 150 mM. Outside this concentration range, actin polymerization became slower or did not happen. NaCl was added to some assays. Fluorescence microscopy was done for different KCl concentrations in order to confirm that the filament length distribution is the same within this range.

In chapter 2.2.3, similar experiments in the presence of FH2 are shown. The KCl concentration was varied between 10 and 90 mM. A salt effect was found. The experiments were performed at two different actin concentrations. In order to further characterize the salt effect, filament length distribution was measured with fluorescence microscopy at different salt concentrations. The filament length distribution shows that the FH2 mediated actin nucleation is impeded by KCl in the observed concentration range. In some experiments, NaCl was added as a second salt, which further reduced polymerization speed.

The experiments were very sensitive on experimental conditions. Several test assays were necessary to establish the reaction and protein handling conditions that give the most reproducible results (see chapter 4.4 and 4.5 for details). As no TIRF assays were performed, numerous parameters were extracted from the pyrene assays as described therein.

All conditions and results of the pyrene assays are listed in table 2. They will be discussed in the following two chapters. The product of the pyrene assays was sometimes used for further analysis by fluorescence microscopy.

table 2: Pyrene assays - overview of conditions and results. The first three columns show the key assay conditions. The experiments are grouped depending on FH2 concentration and presence/absence of NaCl. The **number of measurements** equals to the number of assays done under the conditions mentioned in this line. In some cases, fewer measurements (in brackets) were used for respective $t_{1/2}$ and m values (also in brackets). Standard deviations are only given when more than 2 datasets were available. k_p , m , t_{lag} and $t_{1/2}$ are results of data analysis (see chapter 2.2.3 and chapter 4.5). A single value, two values, or a mean result with a standard deviation are given in these columns. The actin concentration was always 3 ± 0.1 mM. Pyrene actin concentration was normally $0.59 - 0.60$ μ M (in assays with NaCl: 0.52 ± 0.02 μ M).

c(FH2) nM	c(KCl) mM	c(NaCl) mM	Number of meas.	k_p $10^{-4} s^{-1}$	t_{lag} s	$t_{1/2}$ s	m $10^{-4} s^{-1}$
0	2	0	2 [0]	0.51, 1.09	1786, 2305	N/A	N/A
0	5	0	2 [1]	0.44, 1.13	999, 2886	[7106]	[0.60]
0	10	0	2 [1]	0.67, 2.50	620, 2410	[3410]	[1.28]
0	20	0	3	3.78 ± 1.22	654 ± 497	2609 ± 1056	1.94 ± 0.61
0	30	0	3	3.55 ± 1.10	499 ± 284	2621 ± 1105	1.80 ± 0.58
0	40	0	2	3.62, 5.04	249, 1495	1609, 3427	1.86, 2.57
0	50	0	9	4.91 ± 1.03	499 ± 445	1989 ± 802	2.51 ± 0.54
0	60	0	5	3.94 ± 0.92	614 ± 377	2389 ± 861	2.01 ± 0.46
0	70	0	4	3.49 ± 1.20	423 ± 279	2610 ± 1072	1.77 ± 0.64
0	80	0	2	3.62, 4.79	380, 626	1839, 2527	2.11, 2.42
0	90	0	10	3.85 ± 0.80	556 ± 172	2453 ± 521	2.02 ± 0.40
0	125	0	5	3.21 ± 0.71	549 ± 161	2812 ± 561	1.68 ± 0.37
0	250	0	4 [3]	2.68 ± 1.11	587 ± 400	[3072 \pm 2086]	[1.41 \pm 0.61]
0	390	0	4 [2]	2.07 ± 1.12	454 ± 117	[2673, 3164]	[1.38, 1.61]
0	50	60	1	5.1	243	1565	2.74
0	50	150	2	1.8, 3.5	400, 727	2391, 4578	0.92, 1.85
5.4	40	0	1	79	24	120	41
5.4	50	0	7	76 ± 24	35 ± 16	138 ± 36	38 ± 8
5.4	60	0	2	24, 48	0, 62	224, 258	14, 23
5.4	70	0	3	31 ± 10	75 ± 17	326 ± 76	16 ± 4
5.4	80	0	2	16,38	73, 98	267, 547	9, 16
5.4	90	0	1	16	121	558	7
13.6	10	0	2	192, 211	59, 61	98, 104	71, 76
13.6	20	0	1	97	47	130	47
13.6	30	0	1	144	64	116	61
13.6	40	0	3	74 ± 39	84 ± 13	205 ± 46	32 ± 14
13.6	50	0	5	74 ± 44	58 ± 42	200 ± 55	32 ± 17
13.6	60	0	3	20 ± 5	121 ± 81	479 ± 146	11 ± 3
13.6	70	0	4	24 ± 17	87 ± 57	613 ± 423	12 ± 8
13.6	80	0	3	24 ± 16	140 ± 43	612 ± 420	12 ± 8
13.6	90	0	3	12 ± 6	202 ± 187	872 ± 376	6.0 ± 3.6
13.6	50	15	1	57	120	249	23
13.6	50	60	1	12.1	281	861	6.2
13.6	50	150	2	1.37, 1.98	0, 1000	4459, 4982	0.74, 1.05

2.2.2 Effect of salt on actin polymerization in the absence of FH2

Actin polymerization experiments were performed in the absence of FH2 in order to confirm that there is no salt effect on actin polymerization at a salt concentration range between $20 \text{ mM} \leq c(\text{KCl}) \leq 150 \text{ mM}$. The conditions of these experiments can be found in table 2. A typical assay with four simultaneous measurements is depicted in figure 13. It is obvious that salt has no impact on actin polymerization in the mentioned KCl range.

k_p represents the polymerization constant of the reaction during the elongation phase and steady state (for more on these parameters, see chapters 2.2.3 and 4.5). All comparable k_p s are plotted in figure 14. Below $c(\text{Actin}) = 20 \text{ mM}$ the polymerization speed decreases dramatically or polymerization does not take place. At very high salt concentrations - up to saturation - actin polymerization speed also declines. The results are in agreement with the literature (see chapter 1.3).

The plot of $t_{1/2}$ against $c(\text{KCl})$ (figure 15) confirms these findings.

Pyrene assays of actin polymerization in the absence of FH2 are difficult to reproduce. Therefore usually one will not find different assays from one measurement (multi-cell holder) plotted into the same figure. However, plotting of data points derived from multiple assays allows the conclusion that there is no relevant salt effect between $c(\text{KCl}) = 20 \text{ mM}$ and $c(\text{KCl}) = 100 \text{ mM}$ in the absence of FH2. The critical concentration of actin polymerization is around $c(\text{KCl}) = 10 - 20 \text{ mM}$.

Fluorescence microscopy ($c(\text{Actin}) = 3.04 \text{ }\mu\text{M}$, $c(\text{PyrActin}) = 0.6 \text{ }\mu\text{M}$) confirms that in the range between $c(\text{KCl}) = 40 \text{ mM}$ and $c(\text{KCl}) = 90 \text{ mM}$ the distribution of actin filament lengths is similar or the same. By visual comparison of microscopy images (figure 16), no major difference between the filament distribution becomes apparent. Actin filament length distribution was calculated and fit to exponential functions according to chapter 4.6. The fit did not match well the lower filament size, which presents no surprise (see chapter 4.6). This was especially the case for $c(\text{KCl}) = 10 \text{ mM}$. Therefore, only filaments with a length $> 20 \text{ px}$ ($\approx 1.70 \text{ }\mu\text{m}$) were taken into account for the fit. The size distributions and the fits are shown in figure 17. The size distributions between $c(\text{KCl}) = 40 \text{ mM}$ and $c(\text{KCl}) = 90 \text{ mM}$ have similar fit results (figure 18). The distribution at $c(\text{KCl}) = 10 \text{ mM}$ was difficult to fit and might be different from the distributions at the other concentrations. This can be attributed to the fact that 10 mM is close or slightly below than the critical KCl concentration.

The absence of a salt effect in this concentration range can be confirmed. Addition of high concentrations of NaCl to the solution seems to have the same effect on actin polymerization as KCl (table 2).

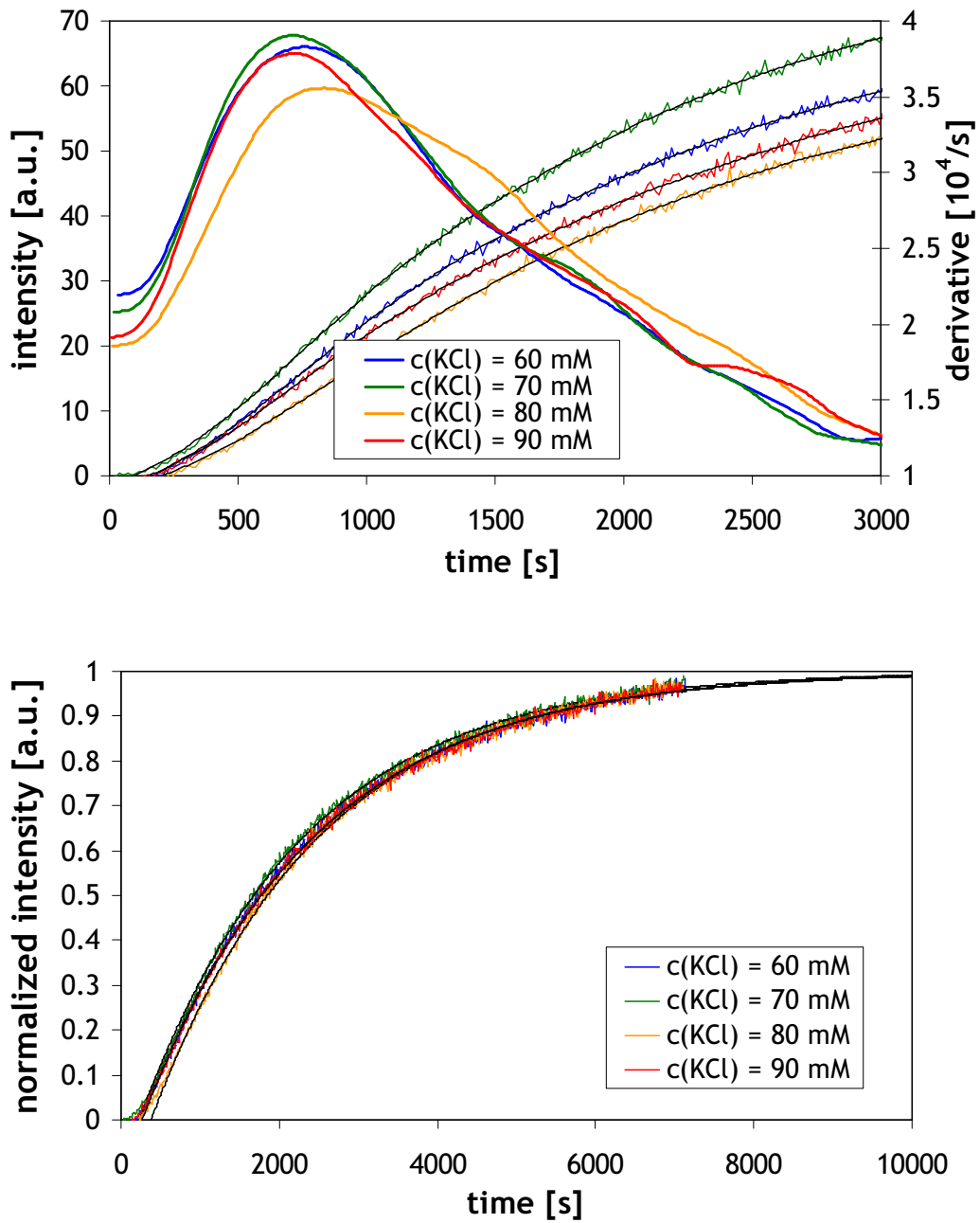


figure 13: Actin polymerization in the absence of FH2 at different KCl concentrations (pyrene assay). No salt effect observable. **Top:** raw data, smoothed curve (black) and derivatives (smooth coloured lines). **Bottom:** normalized raw data (coloured) and fits (black).

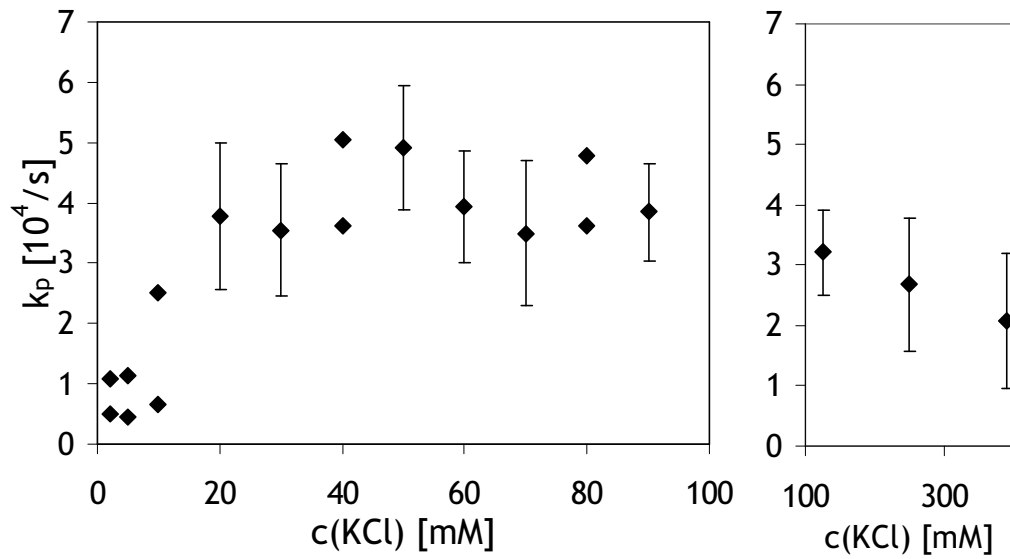


figure 14: Actin polymerization in the absence of FH2: polymerization speed k_p at different KCl concentrations. All data can also be found in table 2. The graph is split for x axis compression at higher $c(KCl)$ concentrations. In the concentration range 20-150 mM, there is no effect of $[KCl]$ on the polymerization speed visible.

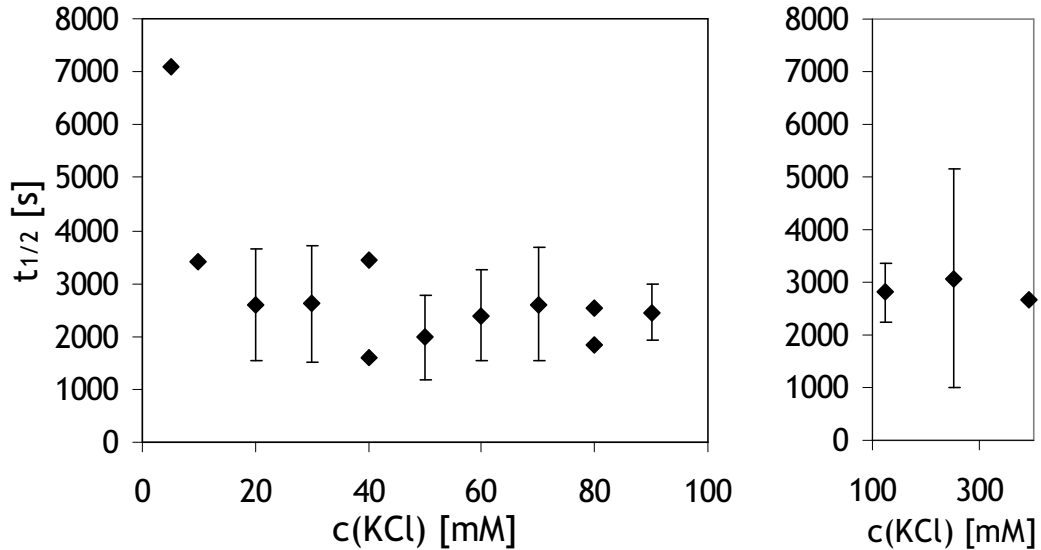
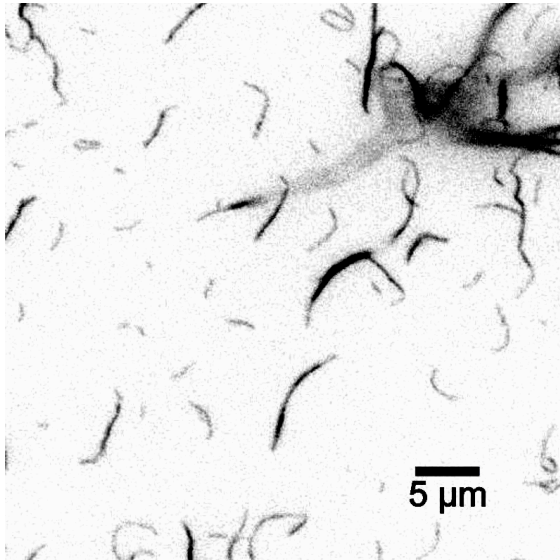
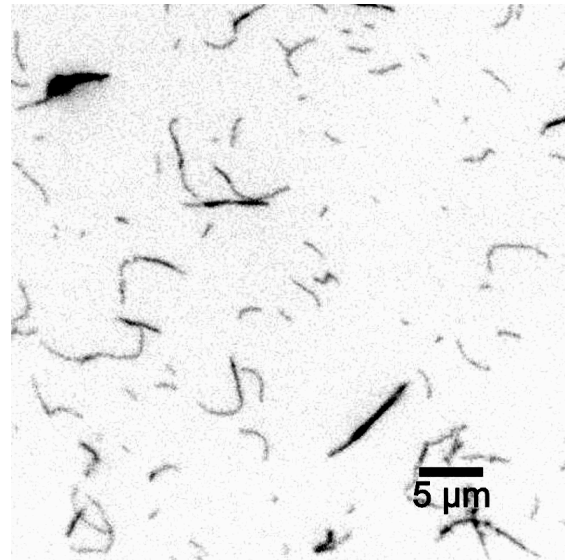


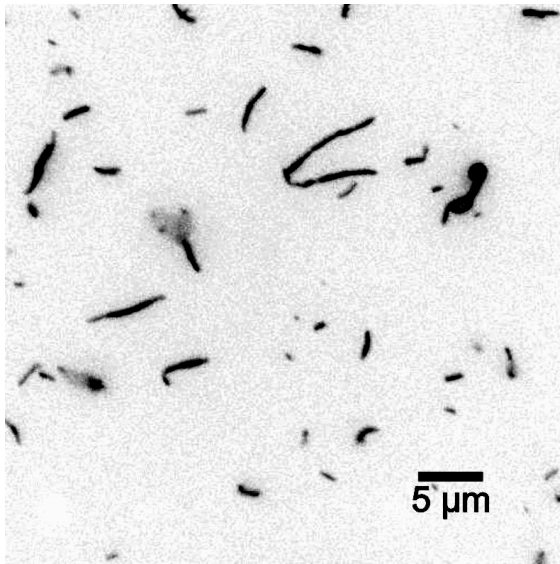
figure 15: Actin polymerization in the absence of FH2: $t_{1/2}$ at different KCl concentrations. All data can also be found in table 2. The graph is split for x axis compression at higher $c(KCl)$ concentrations. In the concentration range ≥ 20 mM, there is no effect of $[KCl]$ on $t_{1/2}$ visible.



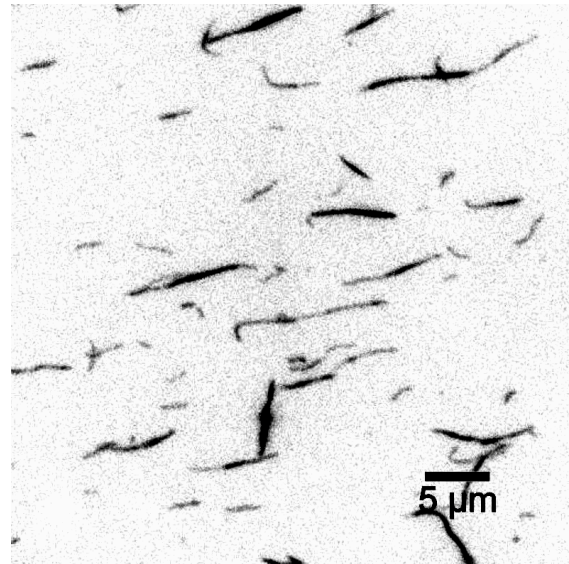
$c(\text{KCl}) = 10 \text{ mM}$



$c(\text{KCl}) = 40 \text{ mM}$



$c(\text{KCl}) = 60 \text{ mM}$



$c(\text{KCl}) = 90 \text{ mM}$

figure 16: Fluorescence microscopy images of actin filaments at different salt concentrations in the absence of FH2. No salt effect is apparent in this concentration range. Images are inverted.

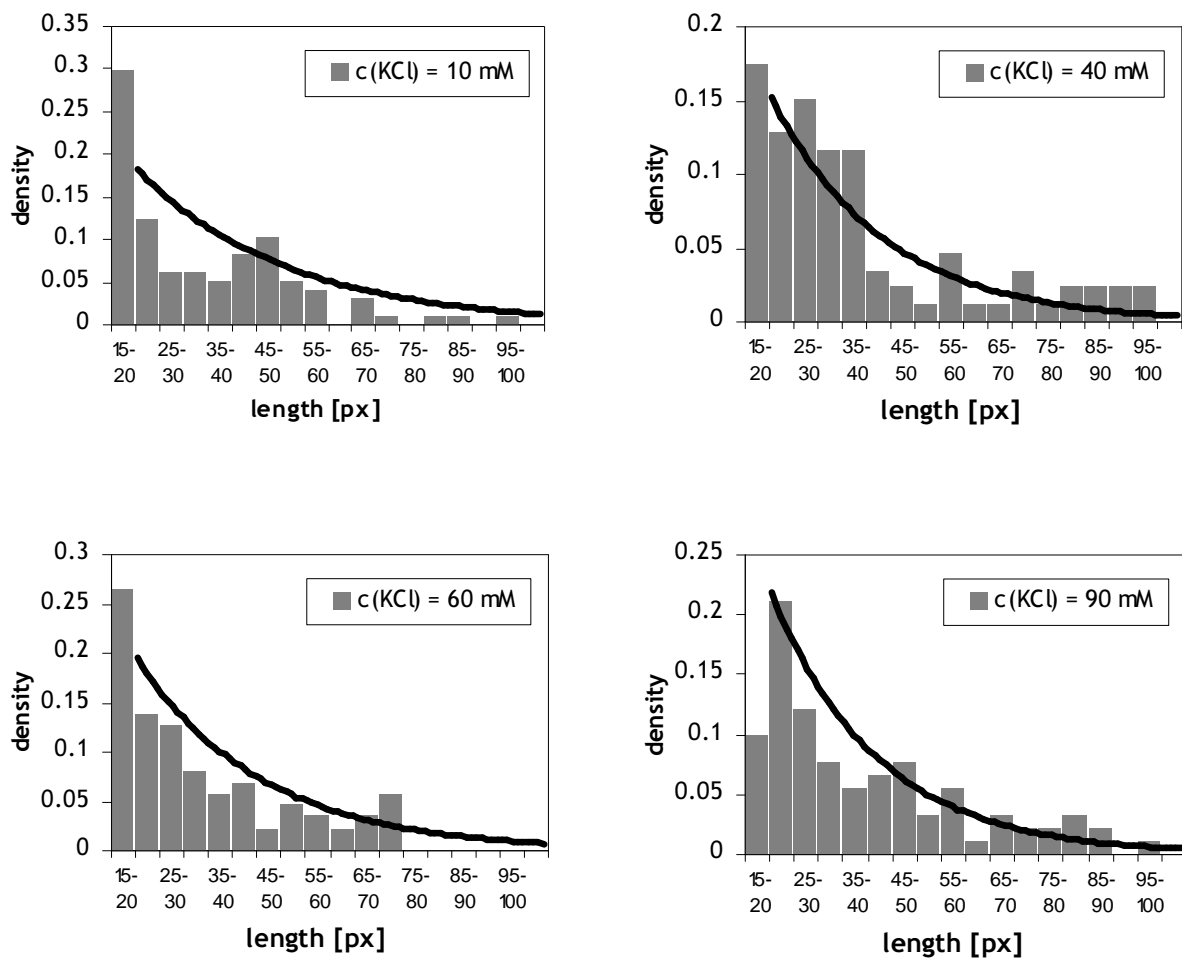


figure 17: Actin filament size distributions and fits in the absence of FH2. Fit curves are printed in black. Fits were performed only for salt concentrations ≥ 20 px (1 px \approx 85 nm). No salt effect is apparent in this concentration range.

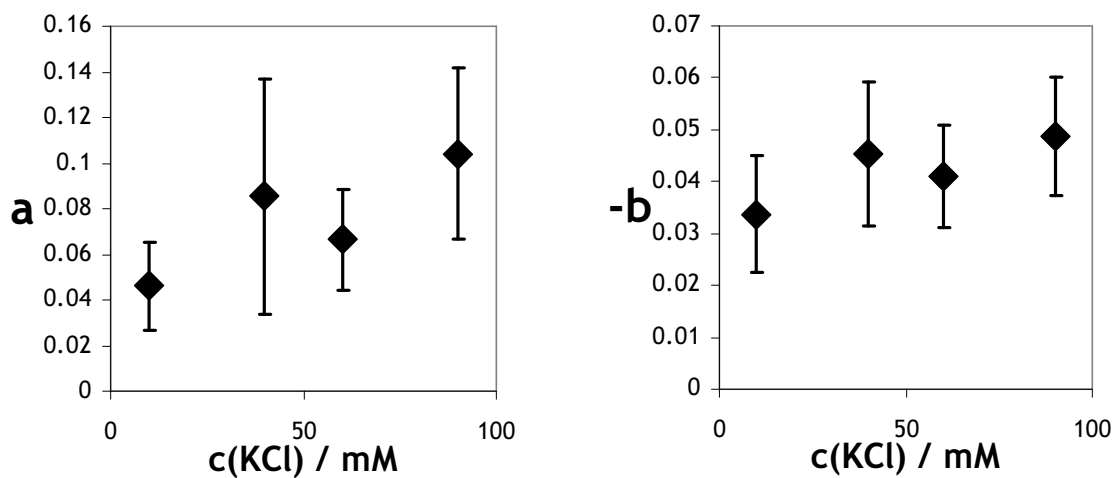


figure 18: Filament size distribution in the absence of FH2, fit results plot. The fit is based on the formula $y = a * \exp(bx)$. No salt effect is apparent in this concentration range, only the a for $c(\text{KCl}) = 10$ mM seems to be low, probably because to the critical KCl concentration (10-20 mM).

2.2.3 Effect of salt on FH2 mediated actin polymerization

In this chapter, actin polymerization experiments in the presence of FH2 are discussed. The KCl concentration was varied between 10 and 90 mM. The experiments were performed at two different FH2 concentrations. In order to further characterize the salt effect, filament length distribution was measured with fluorescence microscopy at different salt concentrations.

The conditions of these experiments can be found in table 2. A typical assay with four simultaneous measurements at $c(\text{FH2}) = 5.4 \text{ nM}$ is depicted at in figure 19. The parameters extracted from all measurements at these FH2 concentrations are plotted in figure 20. More measurements were performed at $c(\text{FH2}) = 13.6 \text{ nM}$ (figure 21 and figure 22). A KCl range from $c(\text{KCl}) = 10 \text{ mM}$ up to $c(\text{KCl}) = 90 \text{ mM}$ is covered.

There is a salt effect observable in the whole tested $c(\text{KCl})$ range.

Polymerization speed, described by m and k_p , was fastest at the lowest measured KCl concentration (10 mM) and slower at the highest measured $c(\text{KCl})$ (90 mM). In the experiment with a combined concentration $c(\text{KCl}) + c(\text{NaCl}) = 200 \text{ mM}$, k_p was even lower. The results for $t_{1/2}$ confirm these findings. k_p represents the elongation phase, but depends on nucleation because nucleation determines the number of growing filaments. t_{lag} , in contrast, depends on the nucleation phase only. t_{lag} data points also show a strong salt effect and therefore point to a salt effect on nucleation (technical details on these parameters: chapter 4.6).

It was not investigated whether the salt effect is specific to KCl. However, in some experiments, NaCl was added, and “common” salt concentrations $c(\text{KCl}) + c(\text{NaCl})$ up to 200 mM were measured (figure 23).

For further understanding and confirming the salt effect, fluorescence microscopy was performed with $c(\text{Actin}) = 3.04 \text{ }\mu\text{M}$ and $c(\text{Pyrene Actin}) = 0.6 \text{ }\mu\text{M}$.

The extent of the salt effect on FH2 mediated actin polymerization became visible already during the measurement (figure 24).

Actin filament lengths were measured and fit to exponential functions according to chapter 4.6. The size distributions and the fits are shown in figure 25. In figure 26 the fits are results are shown.

In order to interpret the these distribution fits, it is important to remember that

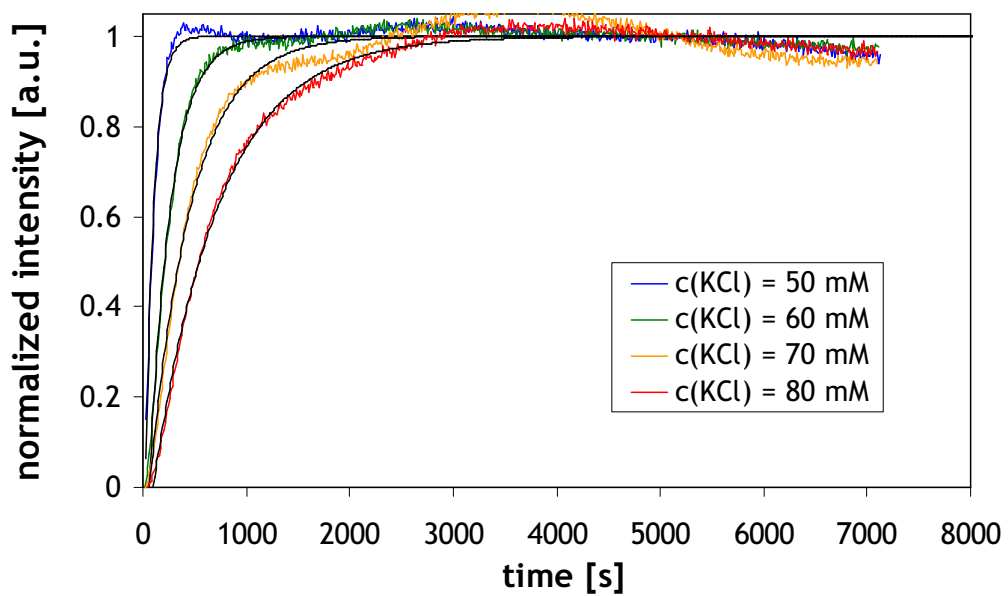
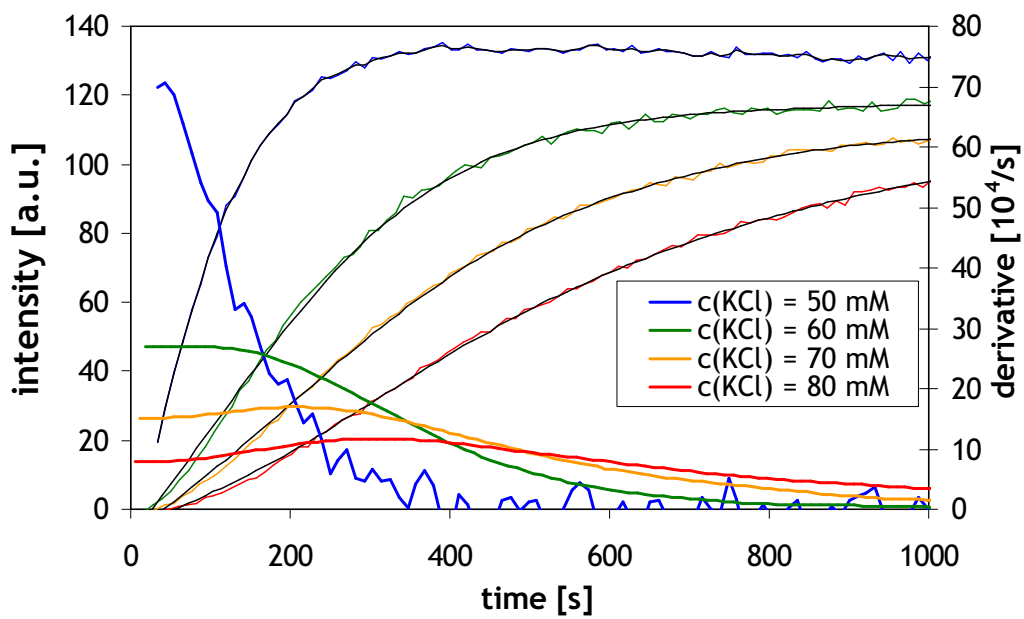


figure 19: Actin polymerization in the presence of FH2 (5.4 nM) at different KCl concentrations (pyrene assay). No salt effect observable. **Top:** raw data, smoothed curve (black) and derivatives (smooth coloured lines). **Bottom:** normalized raw data (coloured) and fits (black).

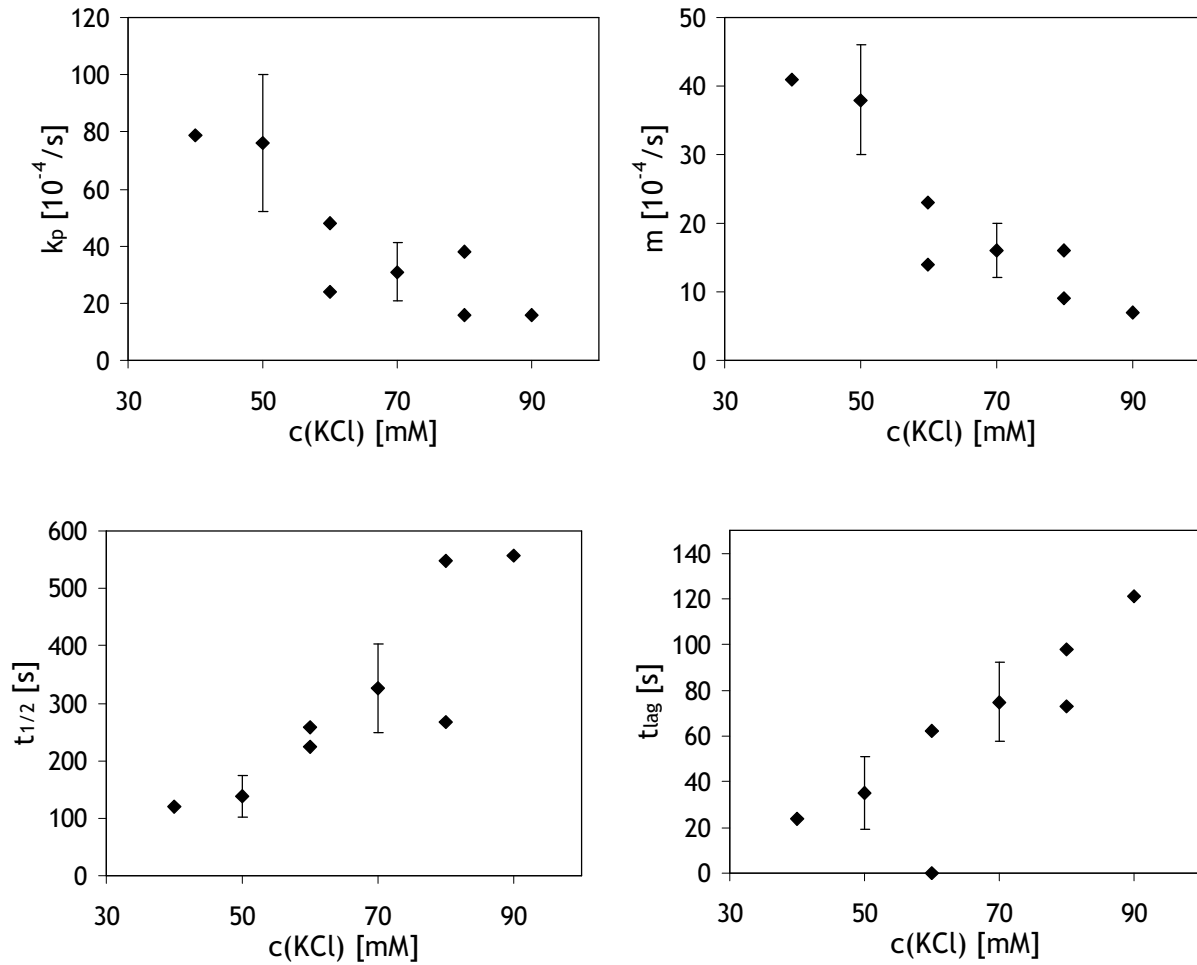


figure 20: Effect of [KCl] on actin polymerization at $c(\text{FH2}) = 5.4 \text{ nM}$. k_p and m both represent the polymerization speed (depends on elongation and the number of nucleated filaments). $t_{1/2}$ is known as a model-free parameter, which also takes the nucleation phases into account. t_{lag} does not depend on elongation. See figure 22 for similar results at $c(\text{FH2}) = 13.6 \text{ nM}$ (more data).

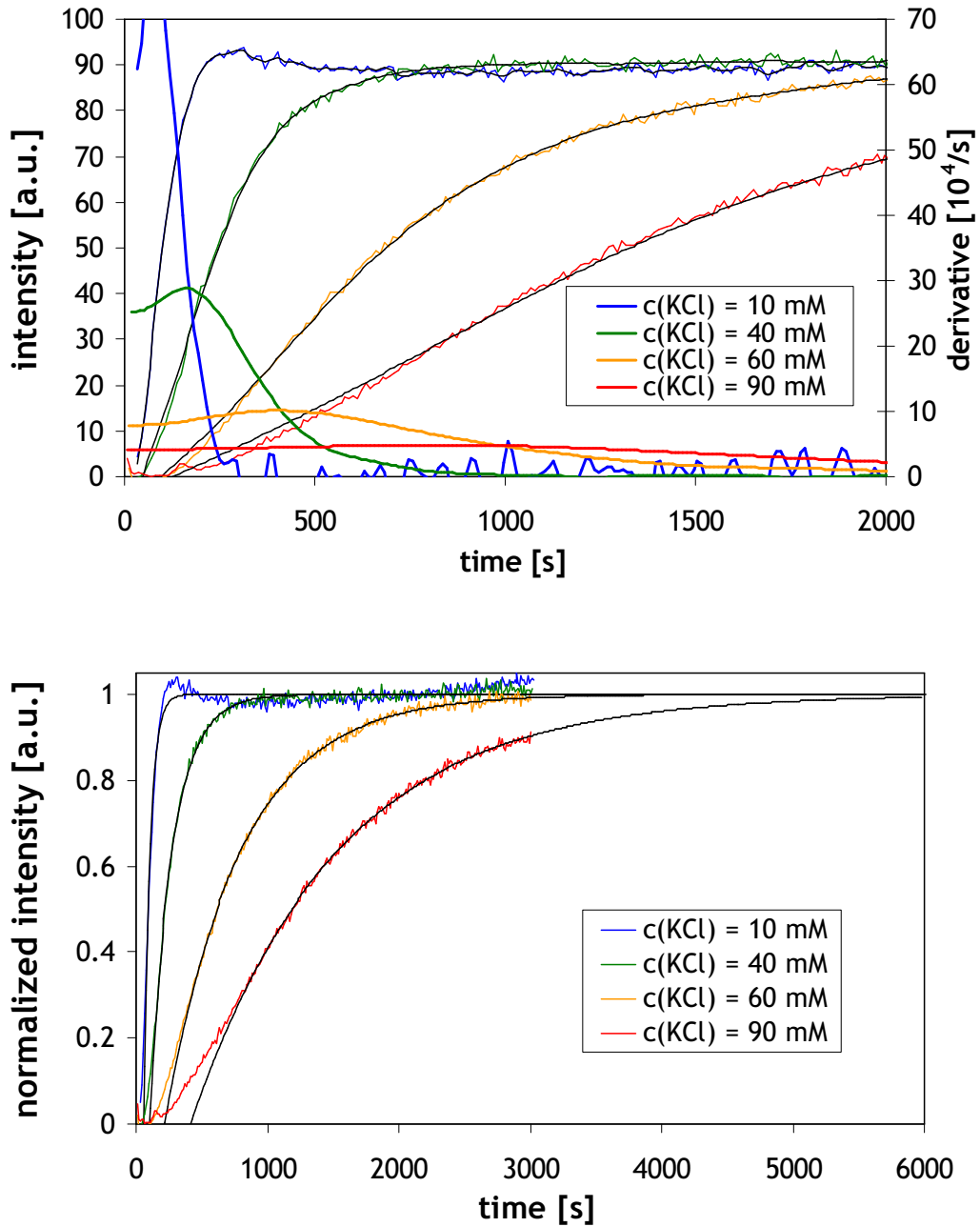


figure 21: Actin polymerization in the presence of FH2 (13.6 nM) at different KCl concentrations (pyrene assay). No salt effect observable. **Top:** raw data, smoothed curve (black) and derivatives (smooth coloured lines). **Bottom:** normalized raw data (coloured) and fits (black).

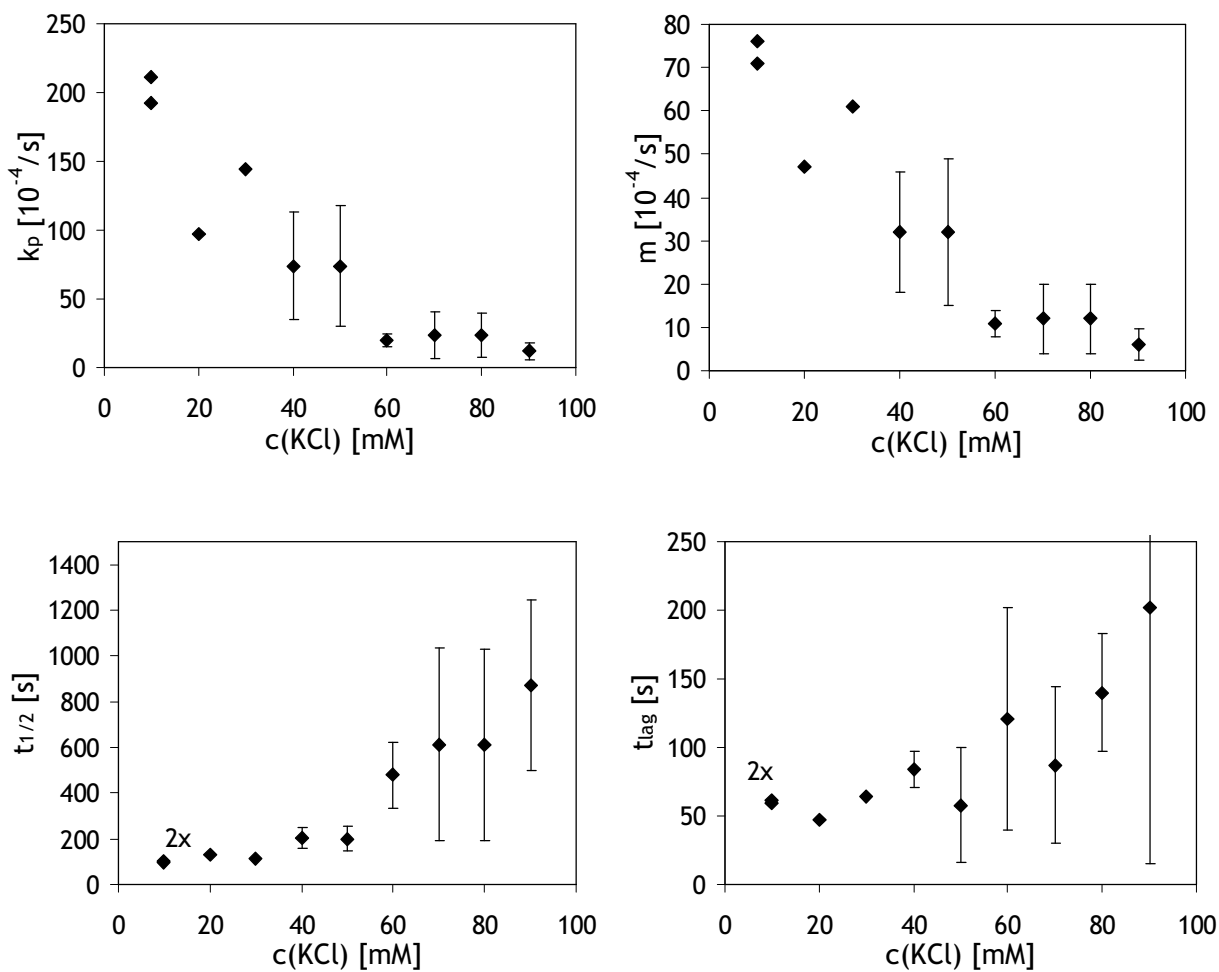


figure 22: Effect of [KCl] on actin polymerization at $c(\text{FH2}) = 13.6$ nM. k_p and m both represent the polymerization speed (depends on elongation and the number of nucleated filaments). $t_{1/2}$ is known as a model-free parameter, which takes also the nucleation phases into account. t_{lag} does not depend on elongation. See figure 20 for similar results at $c(\text{FH2}) = 13.6$ nM (more data).

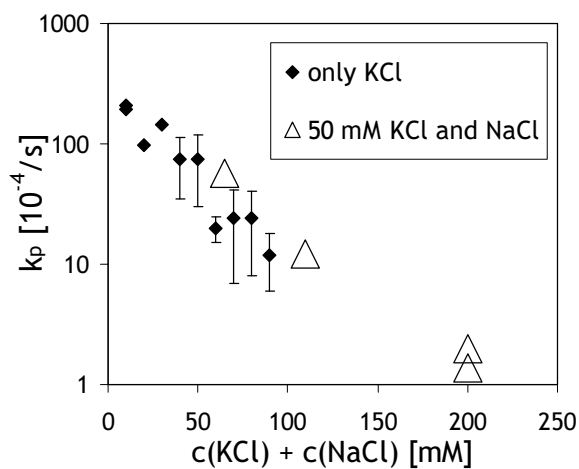
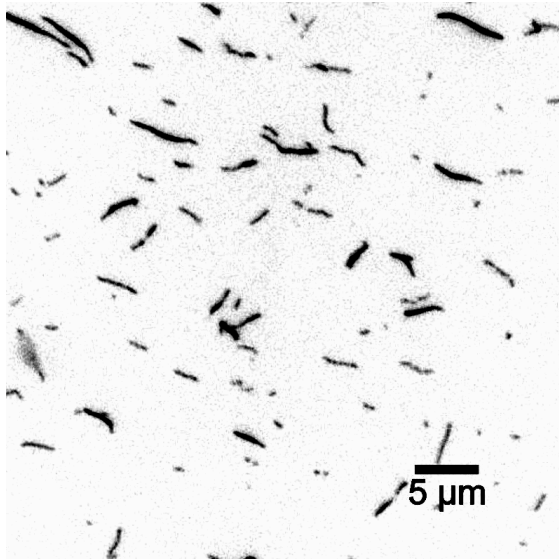
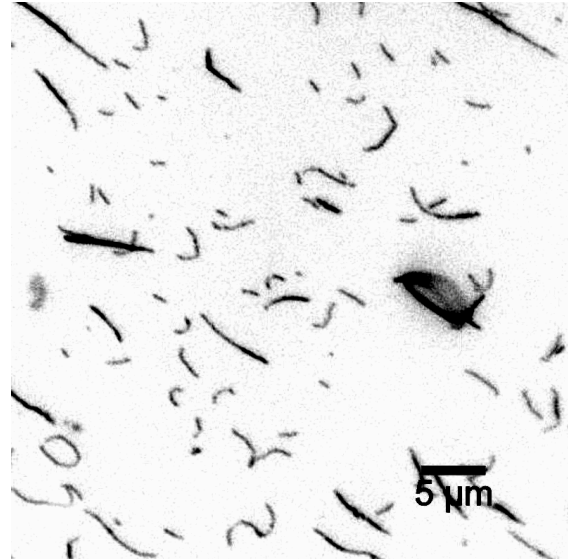


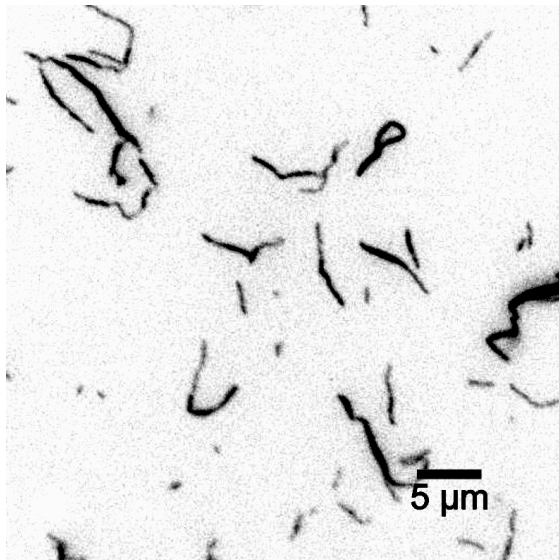
figure 23: Effect of [KCl] and [NaCl] on actin polymerization at $c(\text{FH2}) = 13.6$ nm. The polymerization speed k_p suggests that the salt effect is also relevant at higher concentrations and that it is not limited to KCl.



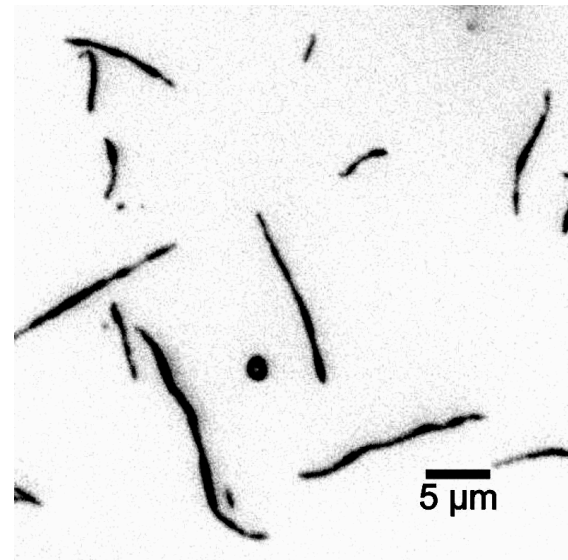
c(KCl) = 10 mM



b: c(KCl) = 40 mM



c(KCl) = 60 mM



c(KCl) = 90 mM

figure 24: Fluorescence microscopy images of actin filaments at different salt concentrations in the absence of FH2. Formin concentration was FH2 mediated with $c(\text{FH2}) = 13.6 \text{ nM}$. At low concentration, short filaments dominate. At higher KCl concentrations, there are fewer and longer filaments. Images are inverted.

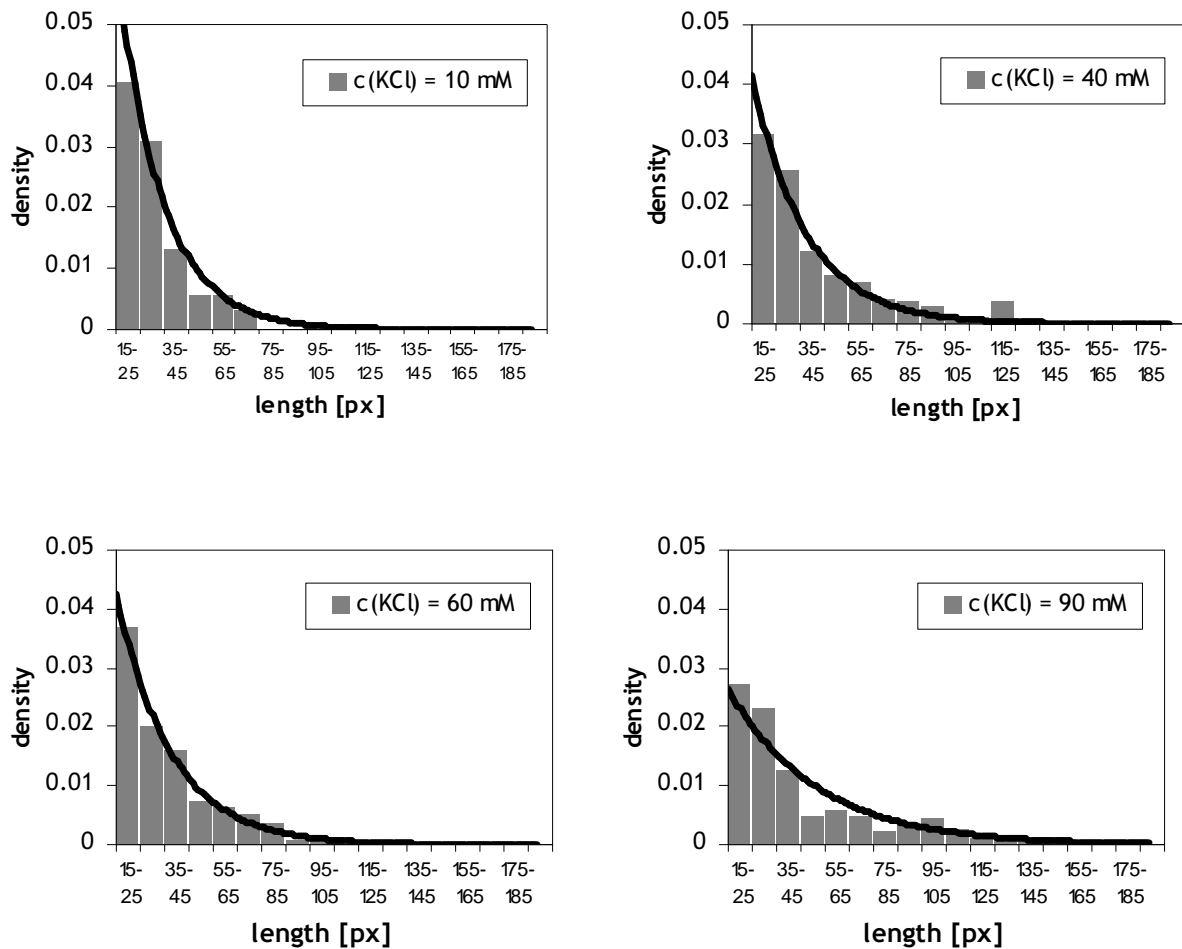


figure 25: Actin filament size distributions of actin filaments after a pyrene assay with $c(\text{FH2}) = 13.6 \text{ nm}$. Fit curves are printed in black. At low KCl concentration, short filaments dominate.

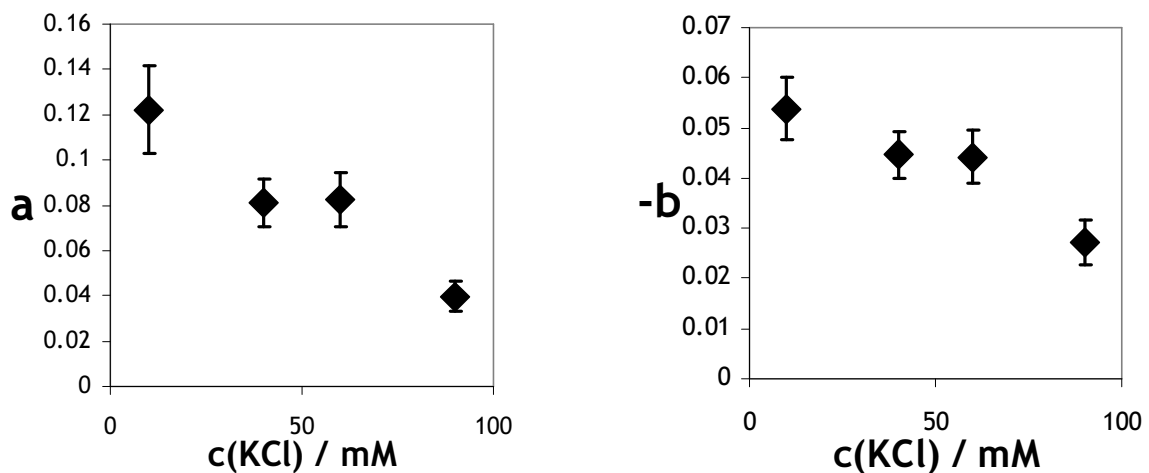


figure 26: Filament size distribution in the presence of FH2 (13.6 nm), fit results plot. The fit is based on the formula $y = a * \exp(bx)$. The salt effect is significant for both fitting parameters. At low concentration, short filaments dominate. At higher KCl concentrations, there are fewer and longer filaments. It can be concluded that KCl inhibits FH2 mediated actin nucleation rather than blocking elongation.

the FH2 domain of Bni1p is known to promote nucleation and slightly block elongation. Pyrene assays showed a higher polymerization speed at low KCl concentrations. Therefore FH2 could enable a higher polymerization speed by two means: It could either promote nucleation even more, or block elongation less. In the first case, lower salt should lead to a higher number of small filaments at low concentration; in the latter case, the filaments should be longer at low concentrations.

Size distributions (figure 26) show that the number of small filaments is higher at a low $c(\text{KCl})$. This shows that there is a salt effect on the nucleation activity of the FH2 domain - salt downregulates nucleation function.

Exponential can only be accurate if the actin polymerization is close to steady state and if annealing and fragmentation are the dominating processes (see chapter 4.6 for details on these processes which will be only mentioned shortly in this chapter). A non-exponential distribution - in extreme case a peak at higher filament lengths - means that these conditions are (still) not realized. However, the fits do match the data reasonably well, and the conclusion remains unequivocal.

It cannot be ruled out that salt blocks the FH2 interaction, also in the sense that FH2 protects barbed actin ends less from annealing. Therefore there could happen more annealing at high salt concentrations. Ring-like structures at higher $c(\text{KCl})$ account for the relevance of this phenomenon (figure 24.d). However, annealing cannot explain the higher polymerization speed observed in pyrene assays. The effect of salt on FH2 nucleation activity is for sure, an effect on annealing might be present on top.

Considering the location and concentration of FH2, it is not probable that fragmentation of actin filaments in the presence differs much from fragmentation in the absence of FH2. Fragmentation is known to be promoted by higher salt concentrations. If the salt effect would be related to fragmentation, one would expect a shift to smaller filaments at higher KCl concentration - the opposite is the case. Fragmentation makes the exponential size distribution possible; however, this distribution is stable in the beginning, and a significant distribution shift to smaller sizes is expected only after several hours.

$c(\text{KCl}) = 10\text{-}20 \text{ mM}$ is the critical concentration for actin polymerization in the absence of FH2. Below this concentration, the formation of alternate actin aggregates hinders actin nucleation (chapter 1.3). Actin polymerization at $c(\text{KCl}) = 10 \text{ mM}$ is particularly fast in the presence of FH2. The formation of aggregates is obviously prevented by stabilisation of actin nuclei by FH2. It cannot be ruled out that FH2 promotes actin nucleation even in the absence of KCl.

In yeast, ion concentrations tend to be higher than in typical *in vitro* experiments (chapter 1.3). The few experiments performed with NaCl and KCl suggest that the salt

effect is not specific and can be observed also at higher ion concentrations. Due to the salt effect found herein, it is recommendable to ensure more realistic salt concentrations for *in vitro* experiments. With higher salt concentrations *in vivo*, less nucleation activity, and eventually more annealing activity is expected. Salt concentrations might also have an effect of *in vitro* and *in vivo* drug function; in attempts to optimize specific FH2 inhibitors (chapter 1.5), salt effects should therefore be taken into account.

A salt effect on nucleation could be explained by reduced electrostatic interaction between actin and FH2: salt covering surface charges of these proteins could reduce the ability of FH2 to recruit actin for nucleation. In order to better understand the electrostatic nature of the salt effect, computational studies were performed; they will be discussed in the next chapter.

2.3 Effect of salt on electrostatic binding free energies and calculation of solvent accessible surface areas (SASAs)

The effect of salt on FH2 mediated actin polymerization could in principle be governed either by its influence on the FH2 dimer structure itself or by the interaction between the FH2 dimer with actin. A reduction of FH2 dimer stability by weakened electrostatic interactions at higher salt concentrations would be reasonable; however, analytical ultracentrifugation showed in the past that the FH2 dimer is very stable even at $c(\text{NaCl})=200$ mM [57]. An electrophoretic mobility assay confirmed the stability of the FH2 dimer [45]. Therefore, electrostatic molecular interactions between FH2 and actin are in the focus of this computational approach to the problem. The knowledge of the Bni1p FH2 dimer structure [45] (PDB number: 1UX4, 1UX5) and identification of conserved amino acids on the exposed parts of the FH2 dimer surface previously led to the identification of two possible regions of electrostatic interaction between FH2 and actin [45]. One is located around the apolar Ile1431 in the knob region, the other around Lys1601 and Lys1359 [36, 45, 46]. Lys1601 residue is located in the *post* region; Lys1359 is located in the lasso subdomain of the other FH2 domain in the dimer. Mutational studies with FH2 domains of Daam1 and Bni1p confirmed the functional importance of these and several near amino acids for regulation of actin nucleation and elongation [36, 45, 46].

A crystal structure of the interaction of an actin molecule with the Bni1p FH2 molecule is available (PDB number: 1Y64) [36]. In order to comprehensively model a salt effect on the nucleation process, it would be necessary to compute different protein complexes of two FH2 domains with up to three actin units, similar to electrostatic calculations for investigating actin nucleation pathways [17]. In this chapter, it will be estimated only how salt could affect the electrostatic interactions between FH2 and actin at a specific patch between these two proteins. The interaction around Ile1431 in the knob region seems to be of mostly hydrophobic nature; in contrast, the interactions around Lys1601 and Lys1359 are probably of electrostatic nature [36]. In the mentioned crystal structure, the latter interaction is readily available and therefore will be used for calculations.

Calculations of electrostatic binding free energies have been focused on a region of the size $24 \text{ \AA} \times 24 \text{ \AA} \times 18 \text{ \AA}$ ($10,368 \text{ nm}^3$) a in the lasso region of Bni1p (FH2 residues 1359-1362, figure 27.a,b). Total electrostatic binding free energies and their Coulomb part were calculated for $c(\text{KCl}) = 10$ mM and $c(\text{KCl}) = 90$ mM ($c(\text{MgCl}_2) = 1.05$ mM). The electrostatic potential was mapped on the surface of the selected region for low and high salt conditions ($\epsilon_r = 2$, figure 27.c-f).

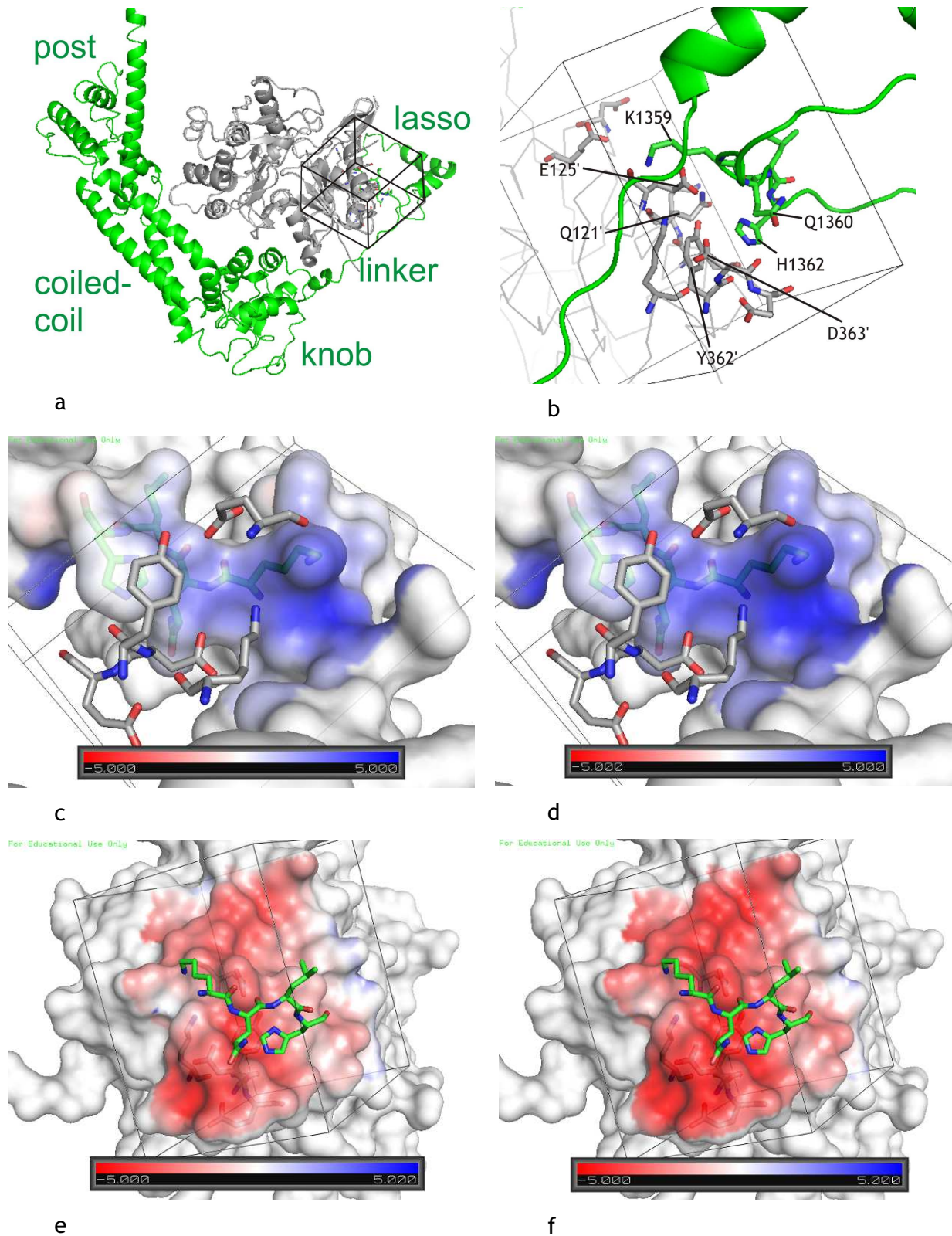


figure 27: Electrostatic interaction between actin and a FH2 molecule at the lasso region at $c(\text{KCl}) = 10 \text{ mM}$ and $c(\text{KCl}) = 90 \text{ mM}$. a. Overview of the interaction (1Y64). Green: FH2; grey: actin; box: analyzed lasso region. b. Interaction at the lasso region at higher magnifications. Colours: see a. Actin amino acids are labelled with a stroke ("'"). c-f: Surface potentials at the lasso interaction site. Blue: positive potential; red: negative potential; actin residues: grey; FH2 residues: green. Box: region for which the electrostatic potential has been calculated (same as in a and b); c and e (left side): $c(\text{KCl}) = 10 \text{ mM}$; d and f (right side): $c(\text{KCl}) = 90 \text{ mM}$. c and d: FH2 surface, calculated for FH2 alone.

Calculated absolute energies depend strongly on various parameters and do not give reliable values; only energy differences are of interest (see chapter 4.7). The total electrostatic binding free energy changes upon salt concentration shift: $\Delta_B\Delta_{\text{Salt}}G_{\text{elec}}(\text{Actin, FH2})$, and their Coulomb part, $\Delta_B\Delta_{\text{Salt}}\Delta_C G_{\text{elec}}(\text{Actin, FH2})$, are listed in table 3 for two different algorithms and several protein dielectrics. The different parameters have been chosen because the setting of these parameters is empirical (chapter 4.7), and only consistent results at different parameters can be considered reliable. $\Delta_B\Delta_{\text{Salt}}G_{\text{elec}}(\text{Actin, FH2})$ is -13.7-15.2 kJ/mol. In other words, the electrostatic interaction between actin and FH2 at this specific patch is estimated to be favoured at lower salt concentrations. This energy difference is reasonable because it is in the energy range of relevant electrostatic protein interactions. It implies a lower K_D and a lower k_-/k_+ ratio at lower salt concentrations (formula 1, chapter 1.3). FH2 can recruit actin more efficiently at lower salt concentrations because the surface protein charges are more exposed and available for electrostatic interaction. The specific interaction patch analyzed herein is probably a major contributor to this salt effect on electrostatic interaction.

It might be of interest to estimate which part of this effect can be attributed to “direct” electrostatic protein interaction (Coulomb interaction). These results ($\Delta_B\Delta_{\text{Salt}}\Delta_C G_{\text{elec}}(\text{Actin, FH2})$ in table 3) show that Coulomb part is the key contributor to this effect. It is more negative than the total electrostatic binding free energy, pointing to a (slightly) opposing role of the solvent.

For visualization, the electrostatic potential was calculated not only for this specific area in the lasso region, but also for the entire actin protein, the entire FH2 protein and the complex of both. The calculation was done for $c(\text{KCl}) = 90 \text{ mM}$ and $c(\text{KCl}) = 10 \text{ mM}$; only the CHARMM27 algorithm and $\epsilon_r = 2$ were used. Visualizations of the resulting electrostatic isosurfaces (at $\pm 1 \text{ kT/e}$) show that the salt effect is evident only

table 3: Calculation of electrostatic binding free energy changes upon shift from $c(\text{KCl})$ from 90 mM to 10 mM at the lasso interaction site. All energies are given in kJ/mol. Energies are calculated with five different ϵ_r and with two different force field algorithms (A = AMBER94, C = CHARMM27). The electrostatic binding free energy $\Delta_B\Delta_{\text{Salt}}\Delta_{\text{elec}}G(\text{Actin, FH2})$ is clearly negative with similar results with different calculation parameters. $\Delta_B\Delta_{\text{Salt}}\Delta_C\Delta_{\text{elec}}G(\text{Actin, FH2})$ energies are similar or more negative; electrostatic Coulomb interactions are responsible for the salt effect at the lasso interaction site.

$\epsilon_r(\text{protein})$	1		2		4		8		12	
force field algorithm	A	C	A	C	A	C	A	C	A	C
$\Delta_B\Delta_{\text{Salt}}G_{\text{elec}}(\text{Actin, FH2})$	-13.7	-14.6	-13.8	-14.6	-14.4	-14.9	-14.8	-15.2	-14.9	-15.2
$\Delta_B\Delta_{\text{Salt}}\Delta_C G_{\text{elec}}(\text{Actin, FH2})$	-19.4	-19.9	-16.3	-16.9	-15.4	-15.9	-15.1	-15.5	-15.0	-15.3

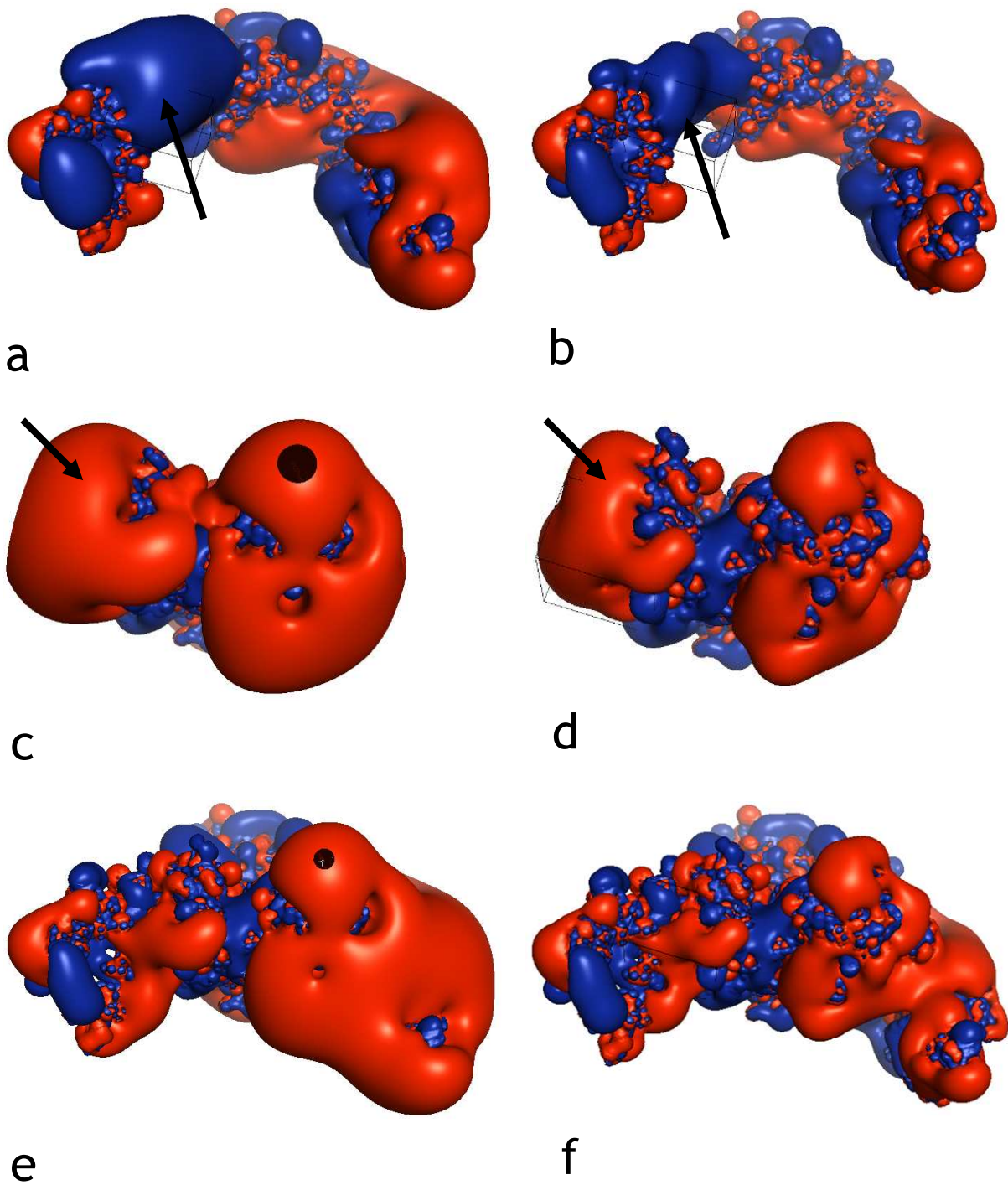


figure 28: Electrostatic isosurfaces of FH2, actin and of the actin-FH2 complex. The arrow highlights the lasso interaction region. Blue: positive isosurface (1 kT/e). Red: negative isosurface (-1 kT/e). a, b: actin; c, d: FH2; e, f: actin-FH2. Left side (a, c, e): $c(\text{KCl}) = 10 \text{ mM}$. Right side (b, d, f): $c(\text{KCl}) = 90 \text{ mM}$.

in a part of the surface (figure 28). Some regions in FH2 remain unchanged. Two obviously bigger potential changes upon salt concentration shift were localized. One of them takes place mainly in the discussed region of interaction at the lasso subdomain. The other region is a FH2 dimerization site. At least a part of the experimentally discovered salt effect can therefore be attributed to electrostatic Coulomb interactions between actin and FH2 at the lasso interaction site. High KCl concentrations disrupt this interaction by reducing the surface charge of the interacting protein sites. Low KCl concentrations lead to a lower binding free energy, to a lower K_D and to a lower k_-/k_+ ratio. This equals to higher actin recruitment by the FH2 domain and to increased FH2-mediated actin nucleation.

In order to further evaluate the nature of the lasso interaction site and to understand why this electrostatic interaction is so significant, ANCHOR server calculations (table 4, experimental details see chapter 4.7) have been performed. They yield Δ SASAs (solvent accessible surface areas) and binding energies for individual amino acid residues. The amino acid with the biggest Δ SASA is FH2 residue 1362. It is part of the lasso interaction site, which has been studied in this chapter. Amino acid at rank 9 (FH2 residue 1359) is also part of this region. Binding energies calculated by the ANCHOR server are favourable only for FH2 residue 1359, unfavourable for FH2 residue 1360 and neutral for FH2 residue 1362. Actin residues have also different binding energies, with low Δ SASAs. However, it has been shown in this chapter that binding energies depend on salt concentration and probably also on pH, especially in this region. A shift of salt concentration could change the amino acid specific binding energy significantly. High Δ SASAs of FH2 residues 1359 and 1360 underline that binding energy changes in this region might have a particularly high impact. Amino acids that moderate binding energies and high Δ SASAs are possible targets for protein-protein inhibitors. In this context, it might be worth recalling Beryllon II, a new FH2 inhibitors (chapter 1.5). The compound has a very large surface; due to the big aromatic, sp_2 hybridized system, it is probably flat. It has many negative charges; it is probable that it is a protein-protein interaction inhibitor targeting an anchor site at the FH2 molecule. The lasso interaction site discussed herein is certainly a good candidate.

table 4: Surface accessible surface areas (Δ SASA) and interaction energies of amino acids in the actin-FH2 complex (1Y64). energy: binding energy calculated by the server, ignoring salt and pH contributions. 73 residues had SASA > 0 and are taken into account in this ranking. **Green highlighting:** residues at the lasso interaction area. Anchor regions or residues are characterized by a large Δ SASA and negative binding energy. Due to the large Δ SASA, anchor regions can be good drug targets or electrostatic interaction partners even when the binding energy per amino acid is not very low. Slightly different salt concentrations might, for example, change the binding energy of residues 1362 (Δ SASA rank 1) and 1359 (Δ SASA rank 9) dramatically so that an interaction is more probable.

chain	residue	position	Δ SASA		energy	
			/ \AA^2	rank	/ kcal/mol	rank
FH2	HIS	1362	112.6	1	0.0	40
FH2	GLN	1427	110.5	2	0.4	61
FH2	ILE	1404	108.9	3	-1.3	10
FH2	ILE	1431	84.6	4	-4.0	6
FH2	LYS	1639	83.7	5	-0.5	21
actin	GLN	354	67.4	6	1.1	67
actin	ASN	128	63.2	7	1.0	66
FH2	LYS	1359	60.8	8	-1.0	11
FH2	LYS	1405	60.7	9	-7.0	1
...						
actin	LYS	359	49.6	22	5.2	73
actin	GLU	125	35.0	28	-3.1	8
actin	ASP	363	28.9	35	-0.4	24
FH2	GLN	1360	25.6	37	1.8	69
actin	TYR	362	9.5	56	0.1	44
actin	GLN	121	0.8	70	0.0	40
actin	TRP	356	0.2	73	0.1	44

3 Summary and Outlook

In this work, structure-function relationships between yeast formin Bni1p and actin polymerization were studied. These studies were intended to be based on cloned and expressed formin constructs derived from yeast Bni1p (*Saccharomyces cerevisiae*). In the first part of this work, it was attempted to clone and express those formin constructs, including the key FH2 domain and a modified FH1 domain. Only the expression of the FH2 domain was successful. This construct was used in the second part of the work, which focused on a previously unknown effect of the KCl concentration on the FH2 mediated actin nucleation.

Cloning and expression of the yeast Bni1p FH2 domain in *E. coli* was successful. Molecular cloning of other derived constructs with a polyproline track and cloning of the 1228-FH2 (FH1-FH2) construct were also successful. However, only some of these constructs were expressed in traces. (P)_x-FH2 constructs with one polyproline track of

variable length and (GS)_x-FH2 constructs with one polyproline track and a variable linker between the track and the FH2 domain have been cloned in a batch approach. This batch cloning approach could be useful in order to find a way for cloning multiple constructs of the type (P)_x-(GS)_y-FH2. (P)_x-FH2, (GS)_x-FH2 and combined constructs would be easy to model for several reasons: The interaction of profilin with polyproline is characterized well, the (GS)_y linker follows a wormlike chain model and FH2 crystal structures are known. Models involving both diffusion and concentration-limited actin recruitment kinetics could be tested with such proteins.

The attempt to clone FH2 constructs with attached G-actin binding proteins (Lifeact, WH2) was unsuccessful. Stop mutations within the FH2 domain point to a very unfavourable effect of these combined constructs, but not Lifeact, WH2 or FH2 alone, on *E. coli*. One may speculate about a functional interaction of these constructs with a protein similar to eukaryotic actin.

Pyrene assays and epifluorescence microscopy revealed a salt effect on FH2 mediated actin nucleation, implying that electrostatic interactions play a major role in this process. A detailed protocol for achieving reproducible pyrene assays was developed. The salt effect clearly significant in two measurement series with different FH2 concentrations and investigated for a potassium chloride (KCl) concentration range between 10 mM and 90 mM. Control experiments without FH2 confirm that the salt effect relates to FH2 function. KCl turned out to be a downregulator of FH2 nucleation activity in this concentration range. A higher KCl concentration leads to a significantly lower actin polymerization speed (k_p , m) and to a bigger lag time (t_{lag}) and bigger $t_{1/2}$. In terms of actin filament length distribution, a higher KCl concentration leads to longer and fewer filaments. Experimental data show that the critical KCl concentration is lowered in the presence of FH2 (if not 0). Some initial experiments with sodium chloride were done in this work; they point to a relevance of this salt effect also at salt concentrations \gg 100 mM. Further work is necessary to prove that the discovered salt effect is not salt-specific. In the future, this salt effect should be considered in *in vitro* experiments on formins. For example, *in vitro* screening for FH2 inhibitors should preferably take place at salt concentrations which mimic *in vivo* conditions.

Computational studies were performed to investigate the electrostatic nature of the salt effect further. Electrostatic surface potential and binding free energy changes upon salt concentration change within a known actin-FH2 complex (1Y64) were calculated. A decrease of the KCl concentration leads to lower binding free energies. This is especially the case for one specific interaction site (lasso site) which was

discussed as an important electrostatic interaction site in the literature. The binding free energy at this site is predicted to drop by 13.7-15.2 kJ/mol upon change of $c(\text{KCl})$ from 90 mM to 10 mM due to increased electrostatic Coulomb interactions. Salt leads to a reduction of surface charges necessary for electrostatic FH2-actin interaction. ANCHOR calculations of solvent accessible surface areas (SASAs) show that this site might be a candidate for protein-protein interaction inhibitors. It would not be surprising if one of the existing inhibitors, for example Beryllon II, interacts with this particular site. In the future, mutational studies at this and other interaction sites could reveal where the inhibitor binds. It would then be possible to predict whether an inhibitor binds to a specific isoform or not by structural comparison of homology models. High SASAs of residues HIS1359 and LYS1362 explain why the lasso interaction site plays a crucial role in the electrostatic FH2-actin interaction and why the interaction might be sensitive to salt concentration shifts.

The experimentally found downregulation of FH2 mediated actin nucleation by KCl can therefore be explained by reduced actin recruitment by the FH2 dimer: KCl diminishes the surface charge of FH2 and actin and thus weakens electrostatic Coulomb interactions. The lasso interaction site is probably affected in particular, with a drop of the electrostatic binding free energy upon reduction of KCl concentration and high solvent accessible surface areas (SASAs) at residues HIS1359 and LYS1362. The salt effect is probably a non-specific salt effect. Results of this work suggest that the presence of FH2 lowers the critical KCl concentration; the new critical KCl concentration - if there is any - remains to be determined. Elongation and nucleation rates could be determined by TIRF measurements in the future. The relevance of this new salt effect *in vivo* remains to be demonstrated.

4 Experimental

4.1 Materials

4.1.1 Enzymes, proteins and chemicals

Enzymes

Phusion High Fidelity DNA Polymerase	Biolabs
Pfu DNA Polymerase	Fermentas
Restriction enzymes	Biolabs, Fermentas, Promega
cOmplete™, Mini Protease Inhibitor Cocktail Tablets	Roche
Taq DNA Polymerase	Biolabs
T4 DNA Ligase	Biolabs

These enzymes are often accompanied by buffers, packed as a Kit. These buffers and Kits are not listed explicitly in chapters 4.1.2 and 4.1.3.

Proteins

Bovine Serum Albumin	Sigma
Acetone Powder (Chicken skeletal muscle)	Lab collection (A. Crevenna)
Pyrene Actin	Lab collection (A. Crevenna)
Mouse anti-His antibody	Core Facility collection / former Nigg lab
Goat anti-mouse antibody	Biorad (Cat. No. 170-5047)

Expression of formin constructs is explained in chapter 4.3. Purification of actin from Chicken Acetone Powder is described in chapter 4.4.

Chemicals

Ampicillin (sodium salt)	Roche (Core Facility: Roth)
ATP-NA	Roche
Chloramphenicol	Fluka (Core Facility: Serva)
DTE	Serva
DTT	Biomol

Synperonic® (cat. no. 15976)	Erbslöh
Tryptone	Bacto
Yeast Extract	BioSpringer or Bacto
other standard laboratory chemicals	Merck, Roth and Sigma Aldrich

4.1.2 Kits, vectors and strains

Agarose Gel Extraction Kit (Jena Bioscience) for isolation of DNA fragments

CloneJet™ Kit, Fermentas

E.Z.N.A.® (Omega Bio-Tek) Plasmid Mini Kit

SimplyBlue™ SafeStain Kit (Invitrogen) for staining SDS gels

pJET1.2/blunt cloning vector (Fermentas) for molecular cloning of PCR products (part of the CloneJet™ Kit, Fermentas)

pQE70 vector (Quiagen, expression vector)

Genomic DNA from *Saccharomyces cerevisiae* wild type strain S288C, from lab collection

One Shot® TOP10 Chemically Competent *E. coli* (part of the TOPO® TA Cloning® Kit, Invitrogen) for molecular cloning of PCR products.

Genotype: F⁻ *mcrA* Δ(*mrr-hsdRMS-mcrBC*) Φ80*lacZ*ΔM15 Δ*lacX74 recA1 araD139* Δ(*ara-leu*)7697 *galU galK rpsL* (Str^R) *endA1 nupG*

E. coli BL21-CodonPlus®(DE3)-RP strain (Stratagene) for expression

Genotype: *E. coli* B F⁻ *ompT hsdS*(rB⁻ mB⁻) *dcm*⁺ Tetr *gal* λ(DE3) *endA Hte* [*argU proL Camr*]

E. coli BL21-CodonPlus®-RP strain (Stratagene) for expression

Genotype: *E. coli* B F⁻ *ompT hsdS*(rB⁻ mB⁻) *dcm*⁺ Tetr *gal endA Hte* [*argU proL Camr*]

4.1.3 Buffers, media and solutions

Blotting transfer buffer

50 mM tris base
40 mM glycine
20% (v/v) methanol

Collection gel buffer

12.6% (v/v) 1M tris-HCl
10% (v/v) acrylamide/bisacrylamide 37.5%/1.4% (w/v)
0.1% (w/v) SDS
pH 6.8

DNA loading buffer 6x

in TE buffer
50% (w/v) sucrose
0.25% (w/v) bromophenol blue

Formin elution buffer

modification of Lysis buffer 3: 250 mM imidazole instead of 10 mM imidazole

Formin expression medium 1

in liquid YT medium
33 mM $\text{MgSO}_4 \times 7 \text{ H}_2\text{O}$
1% (w/v) Ampicillin
0.34% (w/v) Chloramphenicol

Formin expression medium 2

liquid YT medium

4% (v/v) glycerol

0.01% (v/v) Synperonic

5.74 mM $K_2HPO_4 \times 3 H_2O$

33 mM $MgSO_4 \times 7 H_2O$

34 μ g/ml Chloramphenicol

100 μ g/ml Ampicillin

pH = 7

Formin gel filtration & storage buffer

20 mM HEPES

200 mM NaCl

10% (v/v) Glycerol

1 mM EDTA

1 mM TCEP

pH = 7.4

Formin washing buffer

modification of Lysis buffer 3: 20 mM imidazol instead of 10 mM imidazol

G buffer (degassed, stored at 4 °C)

2 mM tris-HCl

0.1 mM $CaCl_2$

0.2 mM ATP

0.5 mM DTT

pH = 8.0

KMEI buffer (10x)

10 mM $MgCl_2$

10 mM EGTA

100 mM imidazole

100 mM - 900 mM KCl (variable)

pH = 7.0

Laemmli buffer (typical composition)

63 mM tris-HCl
4% (v/v) SDS
10% (v/v) glycerol
10% (v/v) mercaptoethanol
0.025% (v/v) Bromophenol Blue
pH = 6.8

Lysis Buffer 1

50 mM NaH₂PO₄
500 mM NaCl
10% (v/v) glycerol
10 mM mercaptoethanol or 1 mM TCEP
10 mM imidazol
5 mM MgCl₂
1% (v/v) protease inhibitor solution with
 1 mM AEBSF-HCl
 0.1% (w/v) Pepstatin
 0.1% (w/v) Leupeptin
 0.2% (w/v) Aprotinin
 0.1% (w/v) DNase
or Roche cOmplete™, Mini Protease Inhibitor Cocktail Tablets
pH = 8

Lysis buffer 2

100 mM HEPES
500 mM NaCl
10 mM imidazol
1% (v/v) protease inhibitor solution with
 1 mM AEBSF-HCl
 0.5% (w/v) Pepstatin
 0.25% (w/v) Leupeptin
 0.2% (w/v) Aprotinin

Lysis Buffer 3

50 mM NaH₂PO₄
500 mM NaCl
10% (v/v) glycerol
10 mM imidazol
5 mM MgCl₂
1% (v/v) protease inhibitor solution with
 1 mM AEBSF-HCl
 0.1% (w/v) Pepstatin
 0.1% (w/v) Leupeptin
 0.2% (w/v) Aprotinin
 0.1% (w/v) DNase
pH = 8

ME buffer (10x)

0.5 mM MgCl₂
2 mM EGTA
pH = 8.0

PBS buffer

140 mM NaCl
2.7 mM KCl
10 mM Na₂HPO₄
1.8 mM KH₂PO₄
pH 7.3-7.4

PBS-T buffer

in PBS buffer
 0.5% (v/v) Tween 20

RF1 buffer

100 mM RbCl
50 mM MnCl₂
30 KOAc
10 mM CaCl₂
15% (w/v) glycerol
pH = 5.8

RF2 buffer

10 mM MOPS
10 mM RbCl
75 mM CaCl₂

SDS running buffer

25 mM tris
192 mM glycine
0.1% (w/v) SDS

Separation gel buffer

37.5% (v/v) 1 M tris-HCl
25% (v/v) acrylamide/bisacrylamide 37.5%/1.4% (w/v)
0.1% (w/v) SDS
pH = 8.8

Solution A

0.1 M Tris-HCl
1.4 mM Luminol
pH = 8.0 - 8.6

Solution B

solvent: DMSO
6.7 mM p-coumaric acid

TBE buffer 10x

440 mM tris base
440 mM boric acid
10 mM EDTA
pH = 8.0

TE buffer 10x

10 mM tris base
1 mM EDTA
pH = 8.0

Terrific Broth medium

1.2% (w/v) Bacto Tryptone
2.4% (w/v) Bacto Yeast Extract
0.4% (v/v) glycerol
17 mM KH_2PO_4
72 mM K_2HPO_4

Tris buffer 1M

619 mM tris-HCl
381 mM tris Base
pH = 8.0

YT medium

0.8% (w/v) Bacto Tryptone
0.5% (w/v) Bacto Yeast Extract
0.5% (w/v) NaCl
often with 100 $\mu\text{g}/\text{ml}$ (alternative: 400 $\mu\text{g}/\text{ml}$ Ampicillin)
often with 34 $\mu\text{g}/\text{ml}$ Chloramphenicol

4.1.4 Oligonucleotides

Oligonucleotides were obtained from Metabion, Martinsried. All oligonucleotides are printed in 5'→3' direction. Sticky ends of aligned primers are highlighted. Code that coincides with the code of the “wild type” formin gene is capitalized.

Important: Restriction sites **BamHI**, **SphI**, **SpeI**, **NgoMIV**, **XmaI** and **PpuMI**. XmaI and NgoMIV are compatible.

Primers for cloning from genomic DNA

FH2

forward primer: **gcatgC**AAATCAAATCAGCTGTAActagtCCATTACTTCCTCAATCGCC
reverse primer: **ggatcc**TTCTTCCACTATTTTCTTATGC

1228-FH1FH2

forward primer: **gcatgC**TCagTACTCAATCATCTGTACTCTCCT
reverse primer: **ggatcc**TTCTTCCACTATTTTCTTATGC

Oligonucleotides for the modification of the FH2 construct (first modification iteration)

Lifeact-FH2

forward: ATGGGTGTCGAGATTTGATCAAGAAATTCGAAAGCATCTCAAAGGAAGAAGCtagcCAAATCAAATCAGCTGTAA
reverse: **ctag**TTACAGCTGATTTGATTTGgctaGCTTCTTCCTTTGAGATGCTTTTCGAATTCTTGATCAAATCTGCGACACCCAT**catg**

WH2-FH2

forward: tcaggaaacaaagcagctccttttgatcaaattagagaggggtgctcagctgaaaaaagtggacagaacgcgtcgCAAATCAAATCAGCTGTAA
reverse: **ctag**TTACAGCTGATTTGATTTGgacgcgcttctgttccacttttttcagctgagcaccctctctaatttgatccaaaagagctgctttgtttcctga**catg**

1321-FH1FH2

forward: CCGCCgGCgCCACCTATGATGCCGGCtagcCAAATCAAATCAGCTGTAA
reverse: **ctag**TTACAGCTGATTTGATTTGgctaGCCGGCATCATAGGTGGcGCcGGCG**catg**

1312-FH1FH2

forward: cTATCTTCATCTACTGATGGCGTCATTCCGCCgGCgCCACCTATGATGCCGGCtagcCAAATCAAATCAGCTGTAA
reverse: **ctag**TTACAGCTGATTTGATTTGgctaGCCGGCATCATAGGTGGcGCcGGCGAATGACGCCATCAGTAGATGAAGATAg**catg**

(P)₄-FH2

forward: ccacctccgcccggctagcCAAATCAAATCAGCTGTAA
reverse: **ctag**TTACAGCTGATTTGATTTGgctagccggcggaggtgg**catg**

(GS)₃-FH2

forward: ccaccgcctcctccgccgggtcaggttctgggtcccAAATCAAATCAGCTGTAA
reverse: **ctag**TTACAGCTGATTTGATTTgggaanatcccagaacctgaccggcggaggaggcgggtgg**catg**

Oligonucleotides for the modification of the (P)₄-FH2 construct (second modification iteration)

(P)₆-FH2

forward: ccaccgcctcctccg
reverse: ccggcggaggaggcgggtggcatg

(P)₈-FH2

forward: ccgccaccaccaccaccaccaccaGctagcCAAATCAAATCAGCTGTAA
reverse: ctacTTACAGCTGATTTGATTTGctagcGctgggtgggtgggtgggtggcggcatg

(P)₁₀-FH2

forward: ccaccgcctccacctccg
reverse: ccggcggagggtggaggcgggtggcatg

(P)₁₂-FH2

forward: ccacctccaccaccgccaccgcctccacctccg
reverse: ccggcggagggtggaggcgggtggcgggtggagggtggcatg

(P)₁₄-FH2

forward: ccaccgcctccacctccaccgcgcctccacctcctccg
reverse: ccggcggaggagggtggaggcggcgggtggagggtggaggcgggtggcatg

Oligonucleotides for the modification of the (GS)₃-FH2 construct (second modification iteration)

(GS)₆-FH2

forward: ccgggtcaggtagtgatcgggttccggctctgg
reverse: gaccagagccggaaccgatccactacctgac

(GS)₉-FH2

forward: ccgggtcaggtagtgatcgggttccggctctggaagtggctcaggttctgg
reverse: gaccagaacctgagccacttccagagccggaaccgatccactacctgac

(GS)₁₂-FH2

forward: ccgggtcaggtagtgatcgggttccggctctggaagtggctcaggtagcgggttccggtagtgatctgg
reverse: gaccagatccactaccggaaccgctacctgagccacttccagagccggaaccgatccactacctgac

(GS)₁₅-FH2

forward: ccgggtcaggtagtgatcgggttccggctctggaagtggctcaggtagcgggttccggtagtgatcgggaagtgggtcaggtctgg
reverse: gaccagagcctgaaccacttccgatccactaccggaaccgctacctgagccacttccagagccggaaccgatccactacctgac

Sequencing primers

1) Primers included in the CloneJet™ Kit, Fermentas

2) Self-designed sequencing primers:

Internal FH2 reverse primer	GATTTTGACAAAACTCAAC
PQE-70 forward primer	gctttgtgagcggataacaa
PQE-70 reverse primer	ggatctatcaacaggagtccaa

4.2 Molecular cloning

4.2.1 General procedure

Molecular cloning experiments followed generally the following procedure:

A PCR of genomic DNA (protocol see below) was performed in order to yield the gene of interest (GOI). Primers for either the FH2 or the 1228-FH1FH2 construct were used. After running a standard Agarose gel electrophoresis (protocol see below), the GOI was cut out under UV illumination and extracted (Agarose Gel Extraction Kit, Jena Bioscience). The PCR product was ligated into a PJET 1.2/blunt vector (Fermentas, protocol see below), then transformed to an *E. coli* TOP10 strain (protocol see below) and grown overnight on YT/Amp plates at 37°C. The next day, 2-12 colonies were picked and grown in liquid YT/Amp (200 rpm shaking) overnight at 37°C. Plasmids were then isolated using E.N.Z.A. Plasmid Miniprep Kit (Protocol I). This protocol was slightly adapted specifically to the amount of processed YT medium. A part of the isolated DNA was used for sequencing (protocol see below), the other part was double digested with SphI (HF) and BamHI; the smaller fragment was isolated (Agarose gel, then extraction) and ligated into a PQE-70 vector (protocol see below), which also had been double digested with SpHI + BamHI. The PQE-70 vector with the construct was transformed into an *E. coli* TOP10 strain (protocol see below). It was grown overnight; 2-12 colonies were picked and grown in liquid YT/Amp overnight. For storage at -80°C, the liquid culture was mixed with the same volume of glycerol (50%) and flash frozen. Plasmids were then isolated as described above. These genomic cloning experiments yielded the FH2 construct and the 1228-FH1FH2 construct.

The plasmids (GOI in PQE-70 vector) were then transformed into the *E. coli* BL21 compatible expression strain (protocol see below). It was grown as described above, but Chloramphenicol was added to the medium in order to keep the pACYC-based plasmid containing extra copies of the *argU* and *proL* tRNA genes.

Alternatively, the GOI was modified in order to yield other constructs. For this, it was double digested with enzymes cutting specifically inside the gene. Two annealed primers were ligated directly to the isolated digestion product (protocol see below). These primers were in big parts complementary, with their sticky ends matching the sticky ends of the digestion product. The further proceeding (starting at transformation of the PQE-70 vector into the *E. coli* TOP10 strain) was the same as above.

These modification steps were performed iteratively in order to yield other, more complex constructs.

The first iteration was based on the FH2 construct:

Beginning of the FH2 construct sequence (the construct is embedded in a PQE-70 vector)

```
5'→3': gcatg|CAAATCAAATCAGCTGTAA|CtagtCCATTACTT(...)
3'→5': c|gtacgTTTAGTTTAGTCGACATTGatc|aGGTAATGAA(...)
```

Digestion of FH2 with **SphI** and **SpeI**, ligation with primers

The following constructs were derived from this FH2 constructs with the corresponding primers:

Lifact-FH2, WH2-FH2, 1321-FH1FH2, 1312-FH1FH2, (P)₄-FH2, (GS)₃-FH2

One second iteration was based on the (P)₄-FH2 construct:

Beginning of the (P)₄-FH2 construct sequence (embedded in a PQE-70 vector)

```
5'→3': gcatg|ccacctccg|ccggctagcCAAATCAAATCAGCTGTAA|CtagtCCATTACTT(...)
3'→5': c|gtacggtggaggccggcc|gatcgGTTTAGTTTAGTCGACATTGatc|aGGTAATGAA(...)
```

Digestion of (P)₄ with **SphI** and **NgoMIV** (compatible with XmaI), ligation with primers. Only (P)₈-FH2: Digestion of (P)₄ with **SphI** and **SpeI**.

The following constructs were derived from these FH2 constructs with the corresponding primers:

(P)₆-FH2, (P)₈-FH2, (P)₁₀-FH2, (P)₁₂-FH2, (P)₁₄-FH2

Another second iteration was based on the (GS)₃-FH2 construct:

Beginning of the (GS)₃-FH2 construct sequence (embedded in a PQE-70 vector)

```
5'→3': gcatg|ccaccgcctcctccgc|ccgggtcaggttctgg|gtcccAAATCAAATCAGCTGTAA|CtagtCC
3'→5': c|gtacggtggcggaggaggccggcc|cagtcgaagaccag|ggTTTAGTTTAGTCGACATTGatc|aGG
```

Digestion of (GS)₃ with **XmaI** (compatible with NgoMIV) and **PpuMI**, ligation with primers; other digestion sites in this construct: **SphI**, **SpeI**.

The following constructs were derived from this FH2 constructs with the corresponding primers:

(GS)₃-FH2, (GS)₆-FH2, (GS)₉-FH2, (GS)₁₂-FH2, (GS)₁₅-FH2

Many constructs of the second modification iterations were yielded by the batch variation of this procedure (see below).

All constructs were sequenced, and test digestions were performed repeatedly during the procedures. All constructs have a HIS-tag at their C-terminal end.

4.2.2 Specific technical protocols

The following technical protocols are listed in this chapter:

Agarose gel electrophoresis

Construct modification

Construct modification (batch modification)

(Double) digestions

E. coli cell density measurements

Ligation of DNA into a PQE-70 plasmid

Ligation of PCR products into a PJET 1.2 vector

Polymerase chain reaction

Preparation of competent *E. coli*

Sequencing

Transformation of *E. coli* strains and plating

Agarose gel electrophoresis

DNA fragment separation was done by standard agarose gel electrophoresis with a standard 1% agarose gel in TBE buffer. A DNA Mix ladder was used. The electric field (100-150V) was applied for 30-45 minutes. Gels were photographed with a GeneFlash gel imaging system (Syngene Bio Imaging).

Construct modification

In this procedure, a gene (“old gene of interest”) in a PQE-70 vector is partially substituted by two annealed, partially complementary primers.

A part of the “old gene of interested” is first removed from the PQE-70 vector by double digestion.

For annealing of the two partially complementary primers, 49 µl ddH₂O were mixed with 0.5 µl of the forward and 0.5 µl of the reverse primer (alternative: 46 µl H₂O and 2 µl of each primer). The mixture was heated to 95 °C in a Thermo Electron PxE 0.2 ThermoCycler for 10 minutes. Then it was cooled stepwise (each step 4 minutes): 90 °C, 85 °C, 80 °C, 78 °C, 76 °C, 74 °C, 72 °C, 70 °C, 69 °C, 68 °C, 67 °C, 66 °C, 65 °C, 64 °C, 63 °C, 62 °C, 61 °C, 60 °C, 58 °C, 57 °C, 56 °C, 55 °C, 53 °C, 51 °C, 49 °C, 47 °C, 45 °C, 43 °C, 40 °C, 35 °C, 30 °C, 25 °C. The mixture then was hold at 4 °C. It was then diluted 1:10 (alternative: no dilution).

For ligation of these annealed primers with the PQE-70 vector, 6.5 μl (alternative: 5 μl) double digested cleaned PQE-70 vector with the partial “old gene of interest”, 1.5 μl of the annealed primer solution (alternative: 3 μl), 1 μl ligase buffer and 1 μl ligase were mixed and kept overnight at 16 °C.

Construct modification (batch modification)

The preceding protocol was varied for a batch approach to get several modifications of the construct simultaneously.

Variations of the preceding protocol for the batch approach:

- Initially, 46 μl H₂O are mixed with 2 μl of each primer.
- After primer annealing (“hold at 4 °C”): Instead of dilution prepare a mix of several annealed primers and continue as if it were a single experiment with only one annealed primer. The use of the resulting library is further explained and discussed in the results part.

(Double) digestions

For digestions and double digestions, recommendations by NEB were followed (NEB online Double Digest Finder), even when the restriction enzyme was not purchased from NEB.

E. coli cell density measurements

E. coli cell densities in liquid culture were measured with a GeneSys spectrophotometer (Thermo Electron) at $\lambda = 600 \text{ nm}$ ($\text{OD}_{600} = 1$ corresponds to ≈ 109 cells/ml).

Ligation of DNA into a PQE-70 plasmid

6 μl of double digested DNA, 2 μl of double digested PQE-70 vector, 0.5 μl T4 ligase and 1 μl ligase buffer were mixed and kept 3 hours at room temperature or (in difficult cases) overnight at 16 °C

Ligation of PCR products into a PJET 1.2 vector

0.5 µl PJET 1.2 vector, 0.5 µl T4 ligase and 1 µl ligase buffer were mixed with 5 µl ddH₂O and kept for 20 minutes at room temperature.

Polymerase chain reaction

A PCR mix (36.5 µl ddH₂O, 1 µl dNTP mix, 1 µl genomic DNA, 0.5 µl of each primer, 10 µl Herculase or Pfu Polymerase buffer) was pre-heated for 8 minutes to 95°C. After adding 1 µl of Herculase DNA Polymerase or Pfu DNA Polymerase, the mix was heated for further two minutes. A Thermo Electron PxE 0.2 ThermoCycler to run 32 cycles of the following programme:

1 minute	Denaturation: 95°C
1 minute	Annealing temperature (58 or 60 °C)
1.5 minutes	Synthesis: 72°C

Afterwards the mixture was kept at 72°C for 10 minutes and then hold at 4 °C.

Preparation of competent *E. coli*

E. coli cultures from agar plates were grown in 5 ml YT medium over night at 37°C. 50 ml YT medium were inoculated with 1 ml of the liquid culture and grown until OD₆₀₀ ≈ 0.5. The cultures and all necessary equipment were cooled and then centrifuged at 3000 rpm in a precooled Biofuge Primo R (Thermo Scientific) for 15 minutes. The pellet was resuspended with cooled RF1 (33 ml) and cooled 45 minutes on ice. Cells were harvested again and resuspended with cooled RF2 (5 ml). After incubation on ice for 15 ml, the cells were aliquoted and shock frozen for storage at -80°C.

Sequencing

For sequencing, 3 µl of the plasmid with the GOI were mixed with 3.5 µl ddH₂O and 1 µl of the sequencing primer. For pJET 1.2/BLUNT vectors, the supplied sequencing primers were used; in one case, an internal FH2 reverse primer was needed for complete sequencing. Modified constructs were sequenced directly from the PQE-70 vectors. Sequencing was not very efficient in those cases, therefore 6.5 µl of the plasmid with the GOI sometimes were supplied instead of water. Sequencing primers for the PQE-70 vector were designed (chapter 4.1.4). The internal FH2 reverse primer mentioned above was also used for sequencing constructs in the PQE-70 vector.

The sequencing reactions were carried out by the Core Facility of Max-Planck Institute of Biochemistry using an ABI-3730 (Perkin Elmers) sequencer and ABI Big Dye 3.1 sequencing chemistry.

Transformation of E. coli strains and plating

2 µl non-PCR plasmid or 10 µl of freshly ligated PCR product were added to 50 µl E. coli competent cells on ice and carefully mixed. After 30 minutes, the mixture was heated to 42°C for 2 minutes and then put on ice for another 2 minutes. After addition of 150 µl YT medium, it was waited further 2 minutes. The mixture was plates on a YT plate with antibiotic(s). The culture grown over night at 37°C.

Choice of antibiotic(s) + strains

For sequencing of GOI in PJET 1.2 vector: E. coli TOP10 strain; Ampicillin

For amplification of PQE-70 vector with construct: E. coli TOP10 strain; Ampicillin

For expression of GOI in PQE-70 vector: E. coli BL21-CodonPlus (DE3) RP strain;

Ampicillin + Chloramphenicol. A DE3 and a non-DE3 strain were used.

4.3 Expression of formin constructs

All expression procedures are based on similar protocols for expression of similar constructs [48, 60].

Test expressions (own laboratory)

An *E. coli* BL21-CodonPlus®(DE3)-RP strain or an *E. coli* BL21-CodonPlus®-RP strain with the construct of interest in a PQE-70 vector was grown from plate culture. As a control, strains with empty PQE-70 vectors or strains with no PQE-70 vectors (no Ampicillin) were used. The liquid medium was YT medium with 100 µg/ml (alternative: 400 µg/ml Ampicillin) and 34 µg/ml Chloramphenicol. At an OD₆₀₀ of ≈ 4 (absolute), [30 µl / OD₆₀₀] of the sample were transferred into 3 ml of fresh medium. Induction was started ≈ 3 hours later. Induction time was variable (f.e. 12, 16 or 24 hours), induction temperatures were 16 °C, 24 °C and 37 °C. IPTG concentration was 0.5 mM. [150 µl / OD₆₀₀] of the sample were spun down (VWR Galaxy 16 DH, 11000 g, 1 min).

For a SDS-PAGE analysis without subsequent Western Blotting the pellet was mixed with 25 µl Laemmli buffer (1x) and shortly (5 min) heated to 95 °C for lysis. After cooling and spinning down (VWR Galaxy 16 DH, 11000 g, 1 min) cellular debris, the supernatant was used for molecular weight determination by SDS-PAGE.

For a SDS-PAGE analysis with subsequent Western Blotting the pellet was first lysed with 25 µl of lysis buffer 1 (with mercaptoethanol). Both buffer variations (different protease inhibitor combinations) were tested. Subsequently, 25 µl of the solution were mixed with 25 µl Laemmli buffer. After spinning down (VWR Galaxy 16 DH, 11000 g, 1 min) cellular debris, the supernatant was used for molecular weight determination by SDS-PAGE and Western Blotting.

The gel for SDS-PAGE was composed of a 10% separation gel (9.9 ml separation gel buffer, 75 µl 10% APS, 5 µl TEMED) and a 4% collection gel (5 ml collection gel buffer, 25 µl 10% APS, 5 µl TEMED). SDS running buffer, 8 µl of PageRuler Prestained Protein Ladder and 10 µl of each sample in Laemmli buffer were used to perform the SDS-PAGE. Subsequently, the gel was either stained with the SimplyBlue™ SafeStain Kit or submitted to Western Blot analysis.

For Western blotting, a standard Semi Dry Blot was performed for transfer on a nitrocellulose membrane (Blotting transfer buffer). The positions of the protein ladder bands (determined by staining with Ponceau S) were marked by piercing the membrane. The membrane was blocked with PBS-T containing 0.5% BSA over night.

Washing buffers were PBS-T buffer or PBS buffer. Antibodies were diluted with PBS-T containing 0.5% BSA. The first antibody was mouse anti-HIS IgG (0.05% v/v), the second antibody was HRP-linked goat anti-mouse IgG (0.033% v/v). A chemilumescence reaction was performed by incubating the membrane with a mixture of 6 ml solution A, 60 µl solution B and 1.8 µl H₂O₂ (30%) for 1 minute. Luminescence images were recorded with a Fujifilm LAS-300 imaging system.

Other test expression experiments and large scale production of FH2 was performed by the Core Facility of the Max Planck Institute for Biochemistry. The procedures were discussed and modified extensively; therefore they are described in the following.

Test expressions (Core Facility of the Max Planck Institute for Biochemistry)

The FH2 construct was test expressed following this protocol:

An *E.coli* BL21-CodonPlus®(DE3)-RP strain with the FH2 construct in a PQE-70 vector from plate culture was induced to express the construct. Formin expression medium 1 was used; IPTG concentration for induction was 0.4 mM. Harvests were done after 2.5 / 4 / 16 / 19 hours at 25 °C. Cells were resuspended in 200 µl Lysis buffer 2. After the addition of 50 mg glass beads (Avestin), the suspension was homogenized in a tissue lyzer (30 Hz, 5 min) and centrifuged for 30 min at 14000 rpm. 10 µl of the supernatant were used for protein chip analysis (HT Protein Express Assay Kit, Caliper). Lysis and chip analysis were also performed for the uninduced sample. For test purification, 30 µl MagneHis particles equilibrated in 2x200 µl binding buffer (MagneHis) were added. The suspension was incubated at on a shaker for 60 minutes (4 °C, 1000 rpm) and then washed twice with 200 µl binding buffer (MagneHis). The bound protein was eluted by 50 µl elution buffer (MagneHis) on a shaker at for 30 min (4 °C, 1000 rpm). The eluate was analyzed by coupled liquid chromatography / mass spectrometry (LC/MS).

The conditions of this protocol were varied in order to test the expression of other constructs than the FH2 construct:

- Expression temperature: 16 °C (personal recommendation by D. Kovar) or 25 °C
- Time between induction and harvest: 2.5, 4, 16 or 20 hours
- strains used for expression: *E.coli* BL21-CodonPlus®(DE3)-RP or *E.coli* BL21-CodonPlus®-RP
- YT medium or Terrific broth medium (personal recommendation by D. Kovar)

Large scale expression and purification of the FH2 construct (Core Facility of the Max Planck Institute for Biochemistry)

Large scale expression was performed in a Labfors 3 (Infors HT) fermenter with Formin expression medium 2. During fermentation, 5 ml 0.01 ml/l Synperonic® (antifoaming agent) was added to the solution. The pH was held at 7 with KOH 20% and H₃PO₄ 20%. The culture was grown for 5.5 hours at 37 °C until OD₆₀₀=9.56. It then was induced with 0.5 mM IPTG at 25 °C for 16 hours (absolute final OD₆₀₀ =57.8). After harvesting by centrifugation (8000 rpm, 10 min, 4 °C), a part of the biomass and uninduced sample was prepared for analysis by a protein chip assay. Another part of the biomass was purified.

10 mg biomass was lysed in 60 ml Lysis Buffer (Avestin beads lysis method) and centrifuged for 30 minutes (20500 rpm, 4 °C).

Nickel Sepharose High Performance beads (GE Healthcare) were added to the supernatant; the mixture was rotated on a wheel for 2 hours (4 °C, 200 rpm / min). It was washed twice with Formin washing buffer and eluted fractionwise with Formin elution buffer (each fraction 1 - 1.5 ml). Intermittent centrifugation steps were always performed for 5 minutes (4 °C, 1000 rpm). Small portions of the eluate fractions were used for Bradford assays and chip analyses (see above). Washing fractions and lysate were also analysed.

Elution fractions were desalted by a Hi Prep 26/10 Desalting column (GE Healthcare) and Sephadex G-25 beads (Formin gel filtration & storage buffer). Protein containing fractions and protein concentration were identified by UV absorption. The protein was analyzed by coupled liquid chromatography / mass spectrometry (LC/MS). Other analytical gel filtrations were performed to check for multimerization of the protein. Cross-linked agarose and dextran beads, the column Superdex 75 10/300 GL (GE Healthcare) and the column Superdex 75 10/300 GL (GE Healthcare) were used.

Directly after production, formin aliquots were flash frozen with liquid nitrogen and stored in the -80 °C fridge. Handling of the FH2 protein is discussed in chapter 4.5.

4.4 Actin purification, labelling, storage and handling

Actin was purified from chicken breast acetone powder according to a modified procedure described by Spudich + Watt [119]. All procedures, including procedures with labelled actin, were done in the cold room and/or on ice. All given concentrations are end concentrations.

Chicken breast acetone powder was put for 30 minutes into a flask with G buffer (20 ml per gram acetone powder). The liquid was then filtered through a bandage, and the wet powder in the bandage was squeezed. This extraction procedure was repeated. After centrifugation for 30 minutes (Sorvall Evolution RC centrifuge, SLA1500 rotor, 30000 g, 4 °C) the supernatant was polymerized at 4 °C by addition of 50 mM KCl and 2 mM MgCl₂. After at least two hours, tropomyosin and troponin were extracted with 800 mM KCl. The flask was put for 1.5 hours on a shaker (\approx 0.5 Hz). The mixture was centrifuged for 3 hours (ThermoScientific WX Ultra90 centrifuge, S52 ST rotor, 156000 g, 4 °C).

The pellet was resuspended with G-buffer and dialyzed against G-buffer for 3 days, changing it every 24 hours. The depolymerized actin was purified by gel filtration (column material: Sephacryl S-300 High Resolution, GE healthcare). The eluate fractions (Fraction Collector Frac-950, Amersham Biosciences) were checked for protein presence by absorption measurements (quartz cuvette, λ = 290 nm). A typical eluate profile and the fractions typically pooled are shown in figure 29. The actin concentration of the pooled fractions was documented.

Several methods for the storage of small actin aliquots (200-300 μ l) were tested. Freeze drying (Christ Alpha 2-4 LSC Freeze dryer) was the method proven to be best for getting actin with a relatively reproducible function in pyrene assays.

Shortly before starting pyrene assays, G buffer was added to freeze dried actin. Actin was then dialysed against G buffer for 3 hours. Absorption (λ = 280 nm, λ = 290 nm) was documented for actin concentration determination. The actin sample was usually considered good only for about 24 hours. A pyrene assay several hours after the absorption measurement required another absorption measurement.

Pyrene Actin (reported labelling efficiency: 85%) was available from the lab collection in frozen aliquots. After defrosting on ice, it was centrifuged for 40 minutes (Themoscientific Sorvall Discovery M120 SE centrifuge, S100-AT3 rotor, 60000 rpm, 4 °C). Absorptions (280, 290, 344 nm) were documented right before the measurements. A pyrene actin lot was used for not more than 5 days.

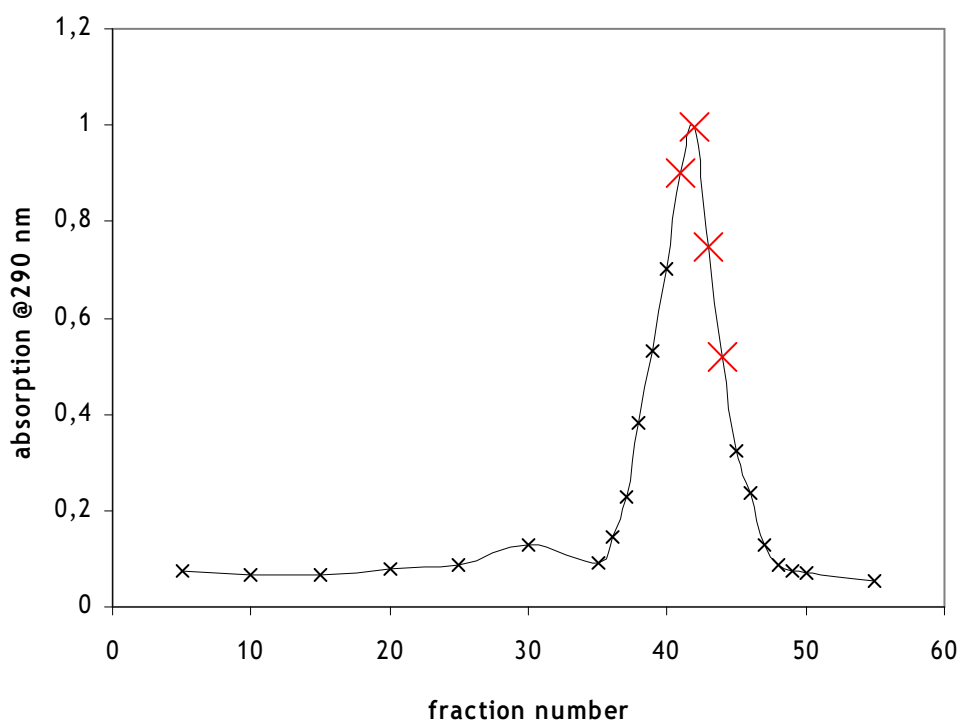


figure 29: Actin purification, typical gel filtration eluate profile. The pooled fractions - later fractions in the big peak - are marked with red crosses. No baseline correction.

4.5 Pyrene assays

Pyrene Assays with formin and actin were found to be very sensitive to reaction conditions. The following very detailed protocol helps to make the data as reproducible as possible.

Assays were performed with an Cary Eclipse Fluorospectrometer and a 4-cell sample holder. The cell holder temperature was set to 20 °C. Detector voltage was set to 700 mV. Excitation wavelength was 365 nm, emission wavelength was 407 nm. In the first hour of the measurement, the maximum possible number of data points was collected. Afterwards, data points were collected every 10 seconds. Maximum measurement time was 12 hours.

KMEI buffers with variable KCl concentrations between 100 mM and 900 mM (end concentrations: 10 x diluted) were used in the experiments.

Before the start of the experiment, actin absorption ($\lambda = 290$ nm) and pyrene actin absorptions ($\lambda = 290$ nm, $\lambda = 344$ nm) were measured. With the absorption data, actin concentrations of both protein solutions and pyrene actin concentrations were calculated ($\epsilon_{\text{PyAc},344} = 22000 \text{ M}^{-1}\text{cm}^{-1}$, $\epsilon_{\text{PyAc},290} = 22000 \text{ M}^{-1}\text{cm}^{-1}$). $A_{344}(\text{PyAc}) \cdot 0.127$ was

subtracted from A_{290} when calculating the Actin concentration in Pyrene Actin solution.

70 μl of protein mix of actin and pyrene actin in G buffer were prepared in order to reach certain actin and pyrene concentrations.

FH2 protein concentration was not measured prior to the assay; it was empirically found that it is most effective to refer to the FH2 concentration (54.34 μM) measured after protein production (shortly before it was frozen).

A starter mix of 10 μl FH2 in G buffer and 10 μl KMEI buffer (with $10 \text{ mM} < c(\text{KCl}) < 90 \text{ mM}$). In few experiments, the starter mix contained also 15 mM to 150 μM NaCl.

70 μl of the pyrene assay protein starter mix were mixed with 10 μl ME buffer for Ca^{2+} exchange and filled into a quartz cuvette. Exactly five minutes later, the fluorescence measurement was started. After 60 seconds, 20 μl of the starter mix were added. Usually four measurements were done simultaneously.

For the analysis of pyrene assay data, normalization is necessary. Normalization reference should be the plateau of the measured intensity curve. Some of the experiments were performed at conditions that did not permit a visual determination of the plateau because it was not reached at the end of the measurement (f.e. due to extreme salt concentrations). Therefore it was necessary to fit the experiment to a model.

Due to the exponential character of elongation kinetics (see chapter 1.1), it can be approximated by a multi-step reaction with a stationary state.

$$c_t(\text{Actin}) = c_{\text{max}}(\text{Actin}) \cdot (1 - \exp(-k_p \cdot t))$$

[2] k_p = polymerization rate; t = time

$c(\text{Actin})$ = concentrations of actin monomers which are part of f-actin

The concentration of actin monomers in f-actin (not g-actin) is proportional to the intensity measured in pyrene assays, the formula can be adapted accordingly. Moreover, the above formula still does not take into account that this reaction is delayed due to the nucleation processes. This delay can be implemented in the formula as a lag phase:

$$I_t = I_{\text{max}} \left(1 - \exp(-k_p \cdot (t - t_{\text{lag}})) \right)$$

[3] I = intensity; I_{max} = maximum intensity

k_p = polymerization constant; t = time;

t_{lag} = lag time

The curve has only an exponential shape exponential when the elongation process dominates; therefore, the fit is performed only for data after the inflection point, which is determined by calculating the derivative of the smoothed data. Matlab (The MathWorks™, Matlab®, Version 7.7.0.471, 2008) was used for data processing. Data processing steps are visualized in figure 30. The general procedure will be commented in this chapter, more specific comments can be found in the code (see Appendix, chapter 5.1).

Smoothing with the Matlab function *spaps* requires a smoothing parameter, which was chosen in order to fit the data close to the inflection point well and to yield a satisfyingly smooth derivative. This method normally yielded unequivocal results for t_{max} ; however, the derivative turned out to be very sensitive on smoothing parameter settings.

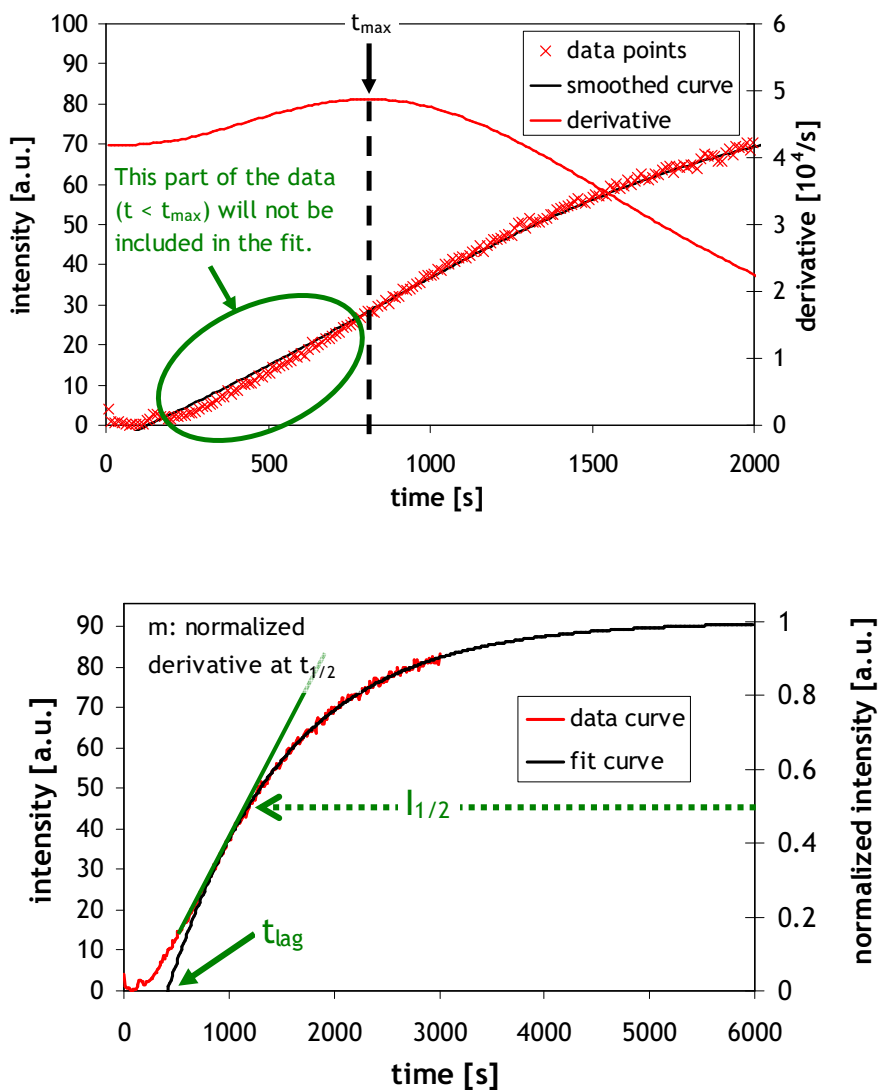


figure 30: Essential steps in pyrene assay data processing. Top: data smoothing and derivative of the smoothed curve. Determination of t_{max} . Bottom: Fit to the data (only $> t_{max}$, secondary scale: after normalization). Determination of m at $t_{1/2}$ ($t_{1/2} = t$ at $I_{1/2}$) Illustration of t_{lag} , which is derived from the fit. I_{max} ($2 * I_{1/2}$) and k_p (not shown) are also derived from the fit.

Once I_{\max} is determined by the fit, the $t_{1/2}$ can be determined (at $t_{1/2}$). The slope m at $t_{1/2}$ is a common empirical parameter, which represents the polymerization speed [48]. This slope turns out to be very sensitive to the derivative, which is based on the smoothed data. It turned out that m at $t_{1/2}$ is often very different than m at t_{\max} (especially at extreme salt conditions which often occur in this work). The first order reaction constant k_p (from the fit) is yielded from the fit and also represents polymerization speed, based on the assumption that the polymerization kinetics after t_{\max} is exponential. A more exact description of elongation kinetics would be possible with the two constants k^+ and k^- . Association velocity is given by $c(\text{free Actin}) \cdot k^+$ and is therefore concentration dependent. Dissociation velocity is directly given by k^- and not concentration dependent. The equation above does not take this difference into account, therefore sufficiently high actin concentrations ($3 \mu\text{M}$) will be chosen so that the fit will match well especially in regions where $k_+ \cdot c(\text{Actin}) \gg k_-$.

The parameter turned out to be relatively insensitive to the smoothing parameter. Both k_p and m will be given in the results part.

t_{lag} is classically derived from $t_{1/2}$ and m at m with the formula

$$[4] \quad t_{\text{lag}} (\text{classical}) = -\frac{0.5 - m \cdot t_{1/2}}{m}$$

Due to the aspects mentioned above, this parameter often did yield hardly reproducible or sometimes even negative results (m at $t_{1/2}$ smaller than m at t_{\max}) for t_{lag} . Therefore the t_{lag} values yielded from the fit curve were used. t_{lag} is in this work defined as the time at which the exponential curve of the elongation process crosses the time axis (formula 4).

4.6 Fluorescence microscopy

An actin polymerization assay with or without formin was run. When a steady state was reached (no formin: after 120 minutes), $5 \mu\text{l}$ Alexa488-phalloidin were added to the polymerization assay product ($100 \mu\text{l}$). $5 \mu\text{l}$ polylysine solution were put on a coverslip. After 10 minutes the solution was diluted 100 fold with the same buffer which was used for actin polymerization. The solution was spread on the polylysine covered coverslip. Images of 40-50 different fields of view were taken with the epifluorescence microscope.

Actin filament lengths were measured manually with ImageJ (Wayne Rasband, National Institutes of Health, USA, Version 1.43u). In order to avoid human bias, the experimental conditions were not revealed during the measurements. The following filaments were excluded from counting:

- short filaments < 15 px (~ 1.3 nm). The problem with short filaments is the image quality of some images. In those images, the short filaments were hardly distinguishable from background or unidentified aggregates. It is common to exclude very short filaments from length distribution determinations [120] .
- branched filaments
- circular filaments
- filaments with a pronounced serpentine shape
- any filament that was not unambiguously a single filament
- filaments leaving the image (manual correction of the viewing field was not done to avoid human bias)

These conditions left only little space for interpretation and therefore minimized human bias. However, the number of long filaments will be underestimated because most exclusions apply more often to very long filaments. Therefore a comparison of filament length distributions can also be of qualitative nature. The number of count filaments was 100-122 for experiments without and 218-299 for experiments with FH2 mediated actin polymerization. The number of viewing fields was 5-8 for experiments without FH2 and 7-20 for experiments with FH2 mediated actin polymerization.

In the beginning of actin polymerization experiments, the filament size distribution is not exponential. Close to steady state, fragmentation and annealing dominate the size distribution [121].

Without fragmentation, a wide and irregular peak at higher filament lengths would be expected [121]. Fragmentation leads to an exponential size distribution at steady state [121]. An effect of formins on fragmentation is not expected due to the position of the formin at the barbed (+) end. Therefore, an exponential size distribution was assumed at steady state. After several hours at steady state, the exponential size distribution constant was shown to change; it is shifted to lower filament sizes with time [120]. This size shift depends on $c(\text{KCl})$ and is more pronounced at high salt concentrations [120]. Therefore, size distributions were measured very soon after reaching steady state to avoid a fragmentation-mediated shift of the exponential distributions to lower sizes. However, the size distribution of actin filaments < 3 μm cannot undoubtedly be described by a a single exponential [120], though an exponential fit is expected to be good enough for empirical size distribution description.

The size distribution was fit to the equation

$$[5] \quad y = a \cdot \exp(bx)$$

y is a probability density, x is the filament length in pixels (1 px \approx 85 nm), b is negative.

For this operation, the Matlab (The MathWorks™, Matlab®, Version 7.7.0.471, 2008) Curve Fitting Toolbox™ (least-squares method) was used. For visual confirmation of monomodal distribution, histograms with a bin size of 10 px or 15 px were also generated.

Annealing is a common process occurring in F-actin solutions. It has a big impact on actin filament size distribution [122]. Formin proteins can partially protect actin from annealing [117]. Therefore, it is difficult to compare length distributions of formin-mediated actin polymerizations with those of non-formin-mediated polymerizations. In order to protect samples from annealing, particular attention was paid to treat them equally. Especially mechanical fragmentation by repeated uptake with a pipette was avoided as much as possible. After 1:100 dilution annealing events are expected to be rare.

4.7 Calculation of electrostatic energies and calculation of solvent accessible surface areas (SASAs)

All electrostatic energy calculations are based on PDB protein structure 1Y64, which contains the interaction of an actin molecule with a Bni1p FH2 domain [36]. Two isolated structures, namely actin only and FH2 only, were generated from this dataset. The actin structure contains a modified histidine residue and a tetramethyl rhodamine dye; however, interactions between actin and the FH2 domain take place in areas of the protein that are not close to these modifications. Two other PDB protein structures, one with actin alone and one with FH2 alone, were derived from this file with PyMol™ (The PyMOL Molecular Graphics System, Version 1.3, Schrödinger, LLC).

For electrostatic energy calculations, a force field has to be calculated first. Several force field algorithms are available [123]. The force field of the protein was calculated with the PDB2PQR server application [124, 125]. PropKa [126] was used for assigning protonation at pH = 7.1 (same pH during actin polymerization experiments). Electrostatic energies and the electrostatic surface energies were calculated with APBS 1.3 [127]. The input file for this program was generated with PyMOL ABPS Tools 2.1 (MG Lerner and HA Carlson. APBS plugin for PyMOL, 2006, University of Michigan, Ann Arbor) and modified manually. All electrostatic energy calculations were performed for two different KCl concentration levels (10 and 90 mM, and $c(\text{MgCl}_2) =$

1.05 mM). In order to derive binding energies, energies were calculated for the FH2/actin complex, for FH2 alone and for Actin alone.

The electrostatic energies were first calculated for one small area of protein interaction. For these calculations, an automatically-configured focussing multigrid method, the non-linear Poisson-Boltzmann equation and multiple Debye-Hückel spheres were chosen. The calculations were performed for force fields calculated by two different standard algorithms, CHARMM27 and AMBER94. The choice of the protein dielectric ϵ_r is not trivial [128]. Assuming an approximately apolar environment inside the protein, it could be set to 1 [123, 128]. The standard choice for the dielectric by ABPS and PDB2PQR is 2. Other sources suggest an ϵ_r between 2 and 4 [129, 130]. According to the APBS documentation higher ϵ_r (up to 20) take into account intramolecular motion to a greater extent. The electrostatic calculations were therefore performed for several ϵ_r (1, 2, 4, 8, 12). The solvent dielectric (water) was set to the standard value of 78, while the solvent radius was set to 1.4 for water and to 0 for vacuum (vacuum calculations are needed for electrostatic solvation energy calculations).

Surface potential was visualized with PyMOL ABPS Tools 2.1 (MG Lerner and HA Carlson. APBS plugin for PyMOL, 2006, University of Michigan, Ann Arbor). The electrostatic energies for these visualizations were calculated for the whole proteins and for the protein complex using the standard protein dielectric $\epsilon_r = 2$. One visualization type was the colouring of the solvent accessible potential. The other visualization type was the depiction of isosurfaces at ± 1 kT/e.

For the evaluation of electrostatic energies, it is important to note that their absolute values are inaccurate and not useful. They always have to be put in relation to other values.

The main question to be addressed is: Is the binding of actin and FH2 energetically more favourable at low salt concentrations than at high concentrations ?

The binding free energy of Actin and FH2 is

$$[6] \quad \Delta_B G_{elec}(Actin, FH2) = G_{elec}(ActFH2)_{water} - (G_{elec}(Actin) + G_{elec}(FH2))_{water}$$

If this energy is negative, a binding of actin and FH2 is energetically favourable. In this work, electrostatic energy changes upon salt transfer are defined as

$$[7] \quad \Delta_{salt} G_{elec} = G_{elec, lowsalt} - G_{elec, highsalt}$$

In order to evaluate whether $\Delta_B G_{elec}(Act, FH2)$ is more favourable at low salt concentrations than at high salt concentrations, the difference between $\Delta_B G_{elec}(Act, FH2)$ at low and at high salt concentrations must be calculated:

[8]

$$\Delta_B \Delta_{salt} G_{elec} (Actin, FH2) = \Delta_{salt} G_{elec} (ActFH2)_{water} - (\Delta_{salt} G_{elec} (Actin)_{water} + \Delta_{salt} G_{elec} (FH2)_{water})$$

$$\text{Note: } \Delta_{salt} \Delta_B G_{elec} (Act, FH2) = \Delta_B \Delta_{salt} G_{elec} (Act, FH2)$$

A negative value of $\Delta_B \Delta_{salt} G_{elec} (Actin, FH2)$ would mean (considering equations [8] and [9]) that a salt concentration change from high to low salt would favour the interaction between Actin and FH2 (= lower their electrostatic binding free energy).

Electrostatic solvation energies can be generally calculated with

$$[9] \quad \Delta_S G_{elec} = G_{elec,water} - G_{elec,vacuum}$$

The electrostatic binding free energy of Actin and FH2 can be split into a solvation and a Coulomb part:

$$[10] \quad \Delta_B G (Actin, FH2) = \Delta_B \Delta_S G (Actin, FH2) + \Delta_B \Delta_C G (Actin, FH2)$$

The solvation part of the electrostatic binding free energy upon transfer from high to low salt is - in analogy to [8]:

[11]

$$\Delta_B \Delta_{salt} \Delta_S G_{elec} (Actin, FH2) = \Delta_{salt} \Delta_S G_{elec} (ActFH2) - (\Delta_{salt} \Delta_S G_{elec} (Actin) + \Delta_{salt} \Delta_S G_{elec} (FH2))$$

In order to estimate the Coulomb part of the electrostatic binding free energy upon the transfer from high to low salt, the salt concentration has to be implemented into the reshuffled equation [11], and with equation [12] the following equation is yielded:

$$[12] \quad \Delta_B \Delta_{salt} \Delta_C G_{elec} (Actin, FH2) = \Delta_B \Delta_{salt} G_{elec} (Actin, FH2) - \Delta_B \Delta_{salt} \Delta_S G_{elec} (Actin, FH2)$$

These calculations of $\Delta_B \Delta_{salt} G_{elec} (Actin, FH2)$ and $\Delta_B \Delta_{salt} \Delta_C G_{elec} (Actin, FH2)$ have only been performed for a single specific interaction area between Actin and FH2.

Solvent accessible surface areas (SASA) were computed for the Actin-FH2 complex of the 1Y64 crystal structure by the ANCHOR web server [108].

5 Appendix

5.1 Matlab code for processing pyrene assay data

see chapter 4.5 for further information

```
clear all
DataPath = 'C:\workdir\Pyrene Assays\data\';
%Read ConditionFile content: one line per dataset, with the 12 columns: data (file) name,
number (1-4) of dataset within the file with the filename in column 1, smoothing parameter, and
9 columns with fitting options (start values and boundaries for the three parameters to be
determined in the fit):
ConditionFile = C:\workdir\Pyrene Assays\data\conditions.csv';
ConditColumnNum=12;
ConditionString=textread(ConditionFile,'%s','delimiter',' ');
NumberDatasets=length(ConditionString)/ConditColumnNum;
%Transfer the contents of the file to appropriate variables:
for j=1:NumberDatasets;
    condit(j).name=ConditionString((j-1)*ConditColumnNum+1);
    condit(j).num=str2num(char(ConditionString((j-1)*ConditColumnNum+2)));
    condit(j).SmoothParameter=str2num(char(ConditionString((j-1)*ConditColumnNum+3)));
    condit(j).fit(1:9)=str2num(char(ConditionString((j-1)*ConditColumnNum+3+[1:9])));
end
%now, every dataset will be analyzed one by one:
for j=1:NumberDatasets
    %One data file can contain the data of up to four assays. The
    %following algorithm helps to read out the data of these assays. The
    %operation is only performed once per data file, namely when the
    %dataset condition points to the first dataset in the data file:
    if condit(j).num == 1;
        data_file = char(strcat(DataPath,condit(j).name, '.csv'));
        filecontents = csvread(data_file, 2, 0);
        File_Line_Number=size(filecontents,1)-1; File_Col_Number=size(filecontents,2);
        for k=1:File_Line_Number;
            for i=1:File_Col_Number-(mod(File_Col_Number,2) == 1);
                rawdata(j-1+round(i/2)).dat(round(i/2-0.1)-round(i/2)+2,
                    1+round(i/2)).num*2-mod(i,2));
            end
        end
    end
    %At the start of the experiment, there is a time gap > 20s in the measurement
    measurements were paused while adding starter solution); determine this time point
    (k) and calculate the baseline from all intensity values before this time point:
    BaselineInt(j,1)=0; stopmodul=0; k=0;
```

```

while stopmodul==0;
k=k+1;
if k>1;if rawdata(j).dat(1, k)-rawdata(j).dat(1, k-1)>20;stopmodul=1;
else;BaselineInt(j,:)=BaselineInt(j,:)+rawdata(j).dat(2, k-1);
end/end;

end; BaselineInt(j,:)=BaselineInt(j,:)/(k-2);
%In very few experiments there were problems before the experiment (f.e. bubbles) which made correct
%measurement impossible; the unusable baseline before experiment start was manually replaced by 0. The
%following algorithms identifies this replacement and calculates a baseline by taking the average intensity
%of the first 5 intensity data points after experiment start. The raw data before experiment start are
%replaced with this baseline values in order to avoid problems with the derivative:
l=k;
if BaselineInt(j, :)==0; while rawdata(j).dat(2, l-1)==0; l=l+1; end
BaselineInt(j,:)=mean(rawdata(j).dat(2,[l:l+5]));
rawdata(j).dat(2,[l:(l-1)])=BaselineInt(j,:); end;
%Correction of the starting time t0. Three components add up to this correction: Time loss due to addition
%of the starter mix (depending on cuvette position); time loss due to a delay between the starter
%mix addition and beginning of the measurement; time loss due to processive measurement (depending on
%cuvette position);
tzerokorr(j)=(condit(j).num==1)*33+ (condit(j).num==2)*18 + (condit(j).num==3)*11+(condit(j).num==4)*6;
%x (t) and y(intensity) values are cut here for further processing: baseline correction, starting time
%correction, removal of the data before experiment start:
x_data(j).dat([1:size(rawdata(j).dat, 2)-k+1])=(rawdata(j).dat(1,k:size(rawdata(j).dat, 2))-[....]
rawdata(j).dat(1,k)+tzerokorr(j));
y_data(j).dat([1:size(rawdata(j).dat, 2)-k+1])=(rawdata(j).dat(2,k:size(rawdata(j).dat, 2))-[....]
BaselineInt(j,:));
%data smoothing:
[smooth_a,smooth_b] = spaps(x_data(j).dat(:)', y_data(j).dat(:)', condit(j).SmoothParameter);
y_smoothed(j).dat=smooth_b';
%calculate derivative from smoothed data:
[gradient_a,gradient_b]=gradient([x_data(j).dat(:),y_smoothed(j).dat]);
y_derivative(j).dat=gradient_b(:,2)./gradient_b(:,1);
%determination of tmax (t of maximum derivation):
tmax(j)=min(find(y_derivative(j).dat(:) == max(y_derivative(j).dat([1:size(y_derivative(j).dat(:))]))));
%In very few cases (for example at c(KCl) = 2 mM in the absence of FH2, the slope was changing very slowly,
and
%the maximum was not reached at the end of the measurements. A fit was made possible by setting tmax to a
%value before the end of the measurement:

```

```

if tmax(j) == size(y_derivative(j).dat(:), 1);
    tmax(j) = size(y_derivative(j).dat(:), 1)-round(size(y_derivative(j).dat(:), 1)/3);end;
%calculation of m at tmax:
m_t_max(j)=y_derivative(j).dat(min(tmax(j))/y_smoothed(j).dat(tmax(j)));
%fit options setting, and fitting of data to fit function:
fitopt1 = fitoptions('Method', 'NonlinearLeastSquares', 'Lower', [condit(j).fit(1:3)], [...]
    'Upper', [condit(j).fit(4:6)], 'Startpoint', condit(j).fit(7:9));
fitopt2 = fitype('a*(1-exp(-b*(x-c)))', 'options', fitopt1);
[res(j).x, res(j).y] = fit(x_data(j).dat([tmax(j):size(x_data(j).dat(:), 1)]), [...]
    y_data(j).dat([tmax(j):size(x_data(j).dat(:), 1)]), fitopt2);
%data output from fit: y max, kp, t lag from fit, and confidence intervals:
ymax(j)=res(j).x.a; kp(j)=res(j).x.b; t_lag_fit(j)=res(j).x.c; confid_intervals=confint(res(j).x);
%normalizing y data to ymax for output:
y_data(j).dat(:)=y_data(j).dat(:)/ymax(j); y_smoothed(j).dat(:)=y_smoothed(j).dat(:)/ymax(j);
y_derivative(j).dat(:)=y_derivative(j).dat(:)/ymax(j);
%In very few cases (described at the end of the previous page), tmax was never reached) there were no data to
%determine t1/2 and m at t1/2).
%These cases are found by the following condition - m and t1/2 are set 0:
if max(y_smoothed(j).dat(:)) < 0.5; t_half(j) = 0; m_t_half(j)=0; else;
%In the cases a fit was successful, t1/2 and m at t1/2 were determined:
t_half(j)=x_data(j).dat(find(y_smoothed(j).dat(:)>=0.5, 1));
m_t_half(j)=y_derivative(j).dat(find(y_smoothed(j).dat(:)>=0.5, 1)); %das ist m bei t1/2
end;
end
end

```

5.2 List of figures

figure 1: Structure of the actin filament and actin polymerization.	- 7 -
figure 2: Roles of profilin, cofilin and Srv2 in actin turnover.	- 10 -
figure 3: Classification of nucleation factors.	- 11 -
figure 4: Function and localization of f-actin and its nucleators in mammalian cells.	- 12 -
figure 5: Classification of elongation factors.	- 12 -
figure 6: Domains of mammalian mDia1.	- 14 -
figure 7: Structure of the dimerized Bni1p FH2 domain.	- 14 -
figure 8: Structure of the FH2-actin complex and flexibility of the FH2 dimer.	- 16 -
figure 9: FH1-dependent and independent actin subunit addition pathways.	- 16 -
figure 10: Inhibitors of formin-mediated actin polymerization.	- 23 -
figure 11: Cloning and expression of formin constructs in this work.	- 26 -
figure 12: Western Blot of a formin test expressions.	- 27 -
figure 13: Actin polymerization in the absence of FH2 at different KCl concentrations (pyrene assay). No salt effect observable.	- 33 -
figure 14: Actin polymerization in the absence of FH2: polymerization speed k_p at different KCl concentrations.	- 34 -
figure 15: Actin polymerization in the absence of FH2: $t_{1/2}$ at different KCl concentrations.	- 34 -
figure 16: Fluorescence microscopy images of actin filaments at different salt concentrations in the absence of FH2.	- 35 -
figure 17: Actin filament size distributions and fits in the absence of FH2.	- 36 -
figure 18: Filament size distribution in absence of FH2, fit results plot.	- 36 -
figure 19: Actin polymerization in the presence of FH2 (5.4 nM) at different KCl concentrations (pyrene assay).	- 38 -
figure 20: Effect of [KCl] on actin polymerization at $c(\text{FH2}) = 5.4 \text{ nM}$.	- 39 -
figure 21: Actin polymerization in the presence of FH2 (13.6 nM) at different KCl concentrations (pyrene assay).	- 40 -
figure 22: Effect of [KCl] on actin polymerization at $c(\text{FH2}) = 13.6 \text{ nM}$.	- 41 -
figure 23: Effect of [KCl] and [NaCl] on actin polymerization at $c(\text{FH2}) = 13.6 \text{ nM}$.	- 41 -
figure 24: Fluorescence microscopy images of actin filaments	

at different salt concentrations in the absence of FH2.	- 42 -
figure 25: Actin filament size distributions of actin filaments after a pyrene assay with $c(\text{FH2}) = 13.6 \text{ nm}$.	- 43 -
figure 26: Filament size distribution in the presence of FH2 (13.6 nM), fit results plot.	- 43 -
figure 27: Electrostatic interaction between actin and a FH2 molecule at the lasso region at $c(\text{KCl}) = 10 \text{ mM}$ and $c(\text{KCl}) = 90 \text{ mM}$.	- 47 -
figure 28: Electrostatic isosurfaces of FH2, actin and of the actin-FH2 complex.	- 49 -
figure 29: Actin purification, typical gel filtration eluate profile.	- 74 -
figure 30: Essential steps in pyrene assay data processing.	- 76 -

5.3 List of tables

table 1: Specific associations of human formins to disease.	- 21 -
table 2: Pyrene assays - overview of conditions and results.	- 31 -
table 3: Calculation of electrostatic binding free energy changes upon shift from $c(\text{KCl})$ from 90 mM to 10 mM at the lasso interaction site.	- 48 -
table 4: Surface accessible surface areas (ΔSASA) and interaction energies of amino acids in the actin-FH2 complex (1Y64).	- 51 -

5.4 Abbreviations

ADP	adenosine diphosphate
AEBSF	4-(2-Aminoethyl) benzenesulfonyl fluoride
ABP	actin binding protein
AML	acute myeloid leukaemia
APS	ammonium persulfate
ATP	adenosine triphosphate
DAD	diaphanous auto-regulatory domain
DD	dimerization domain
DID	diaphanous inhibitory domain
CLL	chronic lymphocytic leukaemia
dNTP	deoxyribonucleoside triphosphate
DMSO	dimethyl sulfoxide
DNA	deoxyribonucleic acid
DTE	dithioerythritol
DTT	dithiothreitol
EDTA	ethylenediaminetetraacetic acid
EGTA	ethylene glycol tetraacetic acid
F-actin	filamentous actin

F-buffer	filamentous actin buffer
FH1/FH2 domain	Formin Homology 1/2 domain
G-actin	globular actin
ΔG_b	binding free energy
G-buffer	globular actin buffer
GOI	gene of interest
GTP	guanosine triphosphate
HEPES	4-(2-hydroxyethyl)-1-piperazineethanesulfonic acid
I_{max}	maximum intensity
IPSS	International Prognostic Score System
IPTG	isopropyl B-D-1-thiogalactopyranoside
k_+	on-rate
k_-	off-rate
K_D	dissociation constant
k_p	polymerization constant
LB	Lysogeny Broth
LC/MS	liquid chromatography / mass spectrometry
MDS	myelodystplastic syndrome
ME	magnesium exchange
MPN	myeloproliferative neoplasm
MOPS	3-(N-morpholino)propanesulfonic acid
NFA	nucleotide-free actin
PBS	(phosphate buffered saline)
PCR	polymerase chain reaction
PIP	phosphatidylinositol phosphate
PIP ₂	phosphatidylinositol 4,5-bisphosphosphate
SASA	solvent accessible surface area
SDS	sodium dodecyl sulfate
SDS-PAGE	sodium dodecyl sulfate polyacrylamide gel electrophoresis
SLIC	sequence and ligation independent cloning
$t_{1/2}$	time at half maximum intensity
t_{lag}	lag time
TBE	tris/borate/EDTA
TCEP	tris(2-carboxyethyl)phosphine
TE	tris/EDTA
TEMED	tetramethylethylenediamine
TIRF	total internal reflection fluorescence
Tris	tris(hydroxymethyl)aminomethane
WH2 domain	WASP Homology 2 domain
YT	Yeast Tryptone

5.5 Abstract

Formin proteins are actin nucleators and elongators which can be found in most eukaryotic cells. In this work, structure-function relationships between yeast formin Bni1p and actin polymerization were studied.

In the first part of this work, it was attempted to clone and express formin constructs derived from yeast Bni1p (*Saccharomyces cerevisiae*), including the key FH2 domain and a modified FH1 domain. Biomathematical models involving both diffusion and concentration-limited actin recruitment kinetics could be tested with such proteins. Cloning was mostly successful, but only the FH2 domain alone was expressed.

In the second part of this work, a salt effect on FH2 mediated actin nucleation was discovered by means of pyrene assays and epifluorescence microscopy. Potassium chloride (KCl) is a downregulator of FH2 nucleation activity: a higher KCl concentration leads to a significantly lower actin polymerization speed (k_p , m), to a bigger lag time (t_{lag}) and to a bigger $t_{1/2}$, with the respective actin filament length distributions. The salt effect was shown to be significant in a KCl concentration range from 10 mM to 90 mM at two different FH2 concentration, but not in absence of FH2. The critical KCl concentration is lowered in the presence of FH2. Some initial experiments with sodium chloride point to a non-specific nature of this salt. This is in agreement with the electrostatic nature of the salt effect, which was studied further by computational means: A decrease of the KCl concentration leads to lower binding free energies of the protein-protein interactions in the crystallographically characterized actin-FH2 complex 1Y64. This is especially the case for the electrostatic Coulomb interaction of a specific area ("lasso" site). ANCHOR calculation results of solvent accessible surface areas (SASAs) corroborate the importance of this site.

The experimentally found downregulation of FH2 mediated actin nucleation by KCl can therefore be explained by reduced actin recruitment by the FH2 dimer: KCl diminishes the surface charge of FH2 and actin and thus weakens electrostatic Coulomb interactions.

In future, this newly discovered salt effect should be considered in experiments on formins, for example when performing *in vitro* screens for FH2 inhibitors. The relevance of this new salt effect *in vivo* remains to be demonstrated.

5.6 Zusammenfassung in deutscher Sprache

Forminproteine sind Aktinnukleatoren und -elongatoren, die in fast allen eukaryotischen Zellen vorkommen. Es wurden in dieser Arbeit Struktur-Funktionsbeziehungen zwischen dem Hefeformin Bni1p und der Aktinpolymerisation untersucht.

Im ersten Teil der Arbeit wurde versucht, verschiedene Forminkonstrukte des Hefeformins bni1p (*Saccharomyces cerevisiae*) mit der Schlüssel-domäne FH2 und gegebenenfalls modifizierter FH1-Domänen zu exprimieren, um damit biomathematische Modelle testen zu können, die sowohl eine diffusions- als auch eine konzentrationslimitierte Kinetik der Aktinrekrutierung annehmen. Die meisten Klonierungen gelangen, exprimiert werden konnte jedoch nur die FH2-Domäne allein. Pyrene-Assays und epifluoreszenzmikroskopische Aufnahmen konnten im zweiten Teil der Arbeit einen bisher nicht bekannten Salzeffekt auf die FH2-vermittelte Aktinnukleation nachweisen. Der Salzeffekt wurde für Kaliumchlorid (KCl) im Konzentrationsbereich $10 \text{ mM} < c(\text{KCl}) < 90 \text{ mM}$ untersucht und war signifikant für zwei Versuchsserien mit unterschiedlichen FH2-Konzentrationen, jedoch nicht in Abwesenheit von FH2. KCl reguliert im genannten Konzentrationsbereich die Aktinnukleationsaktivität von FH2 herunter: Eine höhere KCl-Konzentration führt zu einer signifikant niedrigeren Polymerisationsgeschwindigkeit (k_p , m), zu einer größeren lag time (t_{lag}) und zu einer größeren $t_{1/2}$, mit einer dazu passenden Längenverteilung der Aktinfilamente. Die kritische KCl-Konzentration sinkt in Anwesenheit von KCl. Erste Experimente mit Natriumchlorid deuten an, dass der Effekt unspezifisch ist. Das passt zu der elektrostatischen Natur dieses Salzeffektes, die auch bioinformatisch untersucht wurde: Für eine niedrigere KCl-Konzentration wurden niedrigere freie Bindungsenergien für die Protein-Protein-Interaktion eines kristallographisch beschriebenen Aktin-FH2-Komplexes (1Y64) berechnet. Das gilt insbesondere für die elektrostatischen Coulomb-Wechselwirkungen eines bestimmten Bereiches (Lasso). ANCHOR-Berechnungen der exponierten Proteinoberflächen (SASAs) weisen ebenfalls auf die Bedeutung dieses Bereiches hin.

Die Herunterregulierung der FH2-vermittelten Aktinnukleation durch Kaliumchlorid kann daher mit einer reduzierten Aktinrekrutierung durch das FH2-Dimer erklärt werden: KCl vermindert die Oberflächenladung von FH2 und Aktin und schwächt so elektrostatische Coulomb-Wechselwirkungen.

In der Zukunft sollte dieser neu gefundene Salzeffekt bei *in vitro* - Experimenten mit Forminen berücksichtigt werden, zum Beispiel beim Screening nach FH2-Inhibitoren. Es ist künftig ferner von Interesse, welche Folgen dieser neu gefundene Salzeffekt auf die FH2-vermittelte Aktinnukleation *in vivo* hat.

5.7 Curriculum vitae

Dipl.-Chem. Hans Koss

geboren am 21. Dezember 1982 in Ahlen
Flat 2, 77 Benwell Road, N7 7BW London, Vereinigtes Königreich
hans.koss@gmx.net

Ausbildung

- seit 2011 **Wellcome Trust MPhil/PhD-Programm in Strukturbiologie, Bioinformatik und chemischer Biologie**
am University College London, am Birkbeck College London und am National Institute of Medical Research.
- 2004 - 2011 **Studium der Humanmedizin**
an der Ludwig-Maximilians-Universität München (seit 2006)
an der Charité Berlin (2004 - 2006)
Approbation (2011)
2. Abschnitt der Ärztlichen Prüfung (2011; "gut")
1. Abschnitt der Ärztlichen Prüfung (2006; "gut")
- 2004 - 2010 **Studium der Chemie**
an der Ludwig-Maximilians-Universität München (2006-2010)
an der Technischen Universität Berlin (2004-2006)
Diplom (2010, "sehr gut");
Vordiplom (2006; "gut")
- 2002 - 2004 **Studium der Biochemie** an der Freien Universität Berlin
Vordiplom (2004; "sehr gut")
- 2001 Abitur in Ahlen (1.0, Jahrgangsstufenbester)

Forschungspraktika, Diplomarbeit, medizinische Doktorarbeit

- seit 04/2009 medizinische Doktorarbeit: Mechanismus der Aktinpolymerisation mit Hefeformin Bni1p: Effekt der Kaliumchloridkonzentration auf die FH2 vermittelte Aktinnukleation
experimentelle Arbeit bis 2010, eingereicht im Februar 2012
(Prof. Dr. M. Schleicher, Institut fuer Anatomie und Zellbiologie, Ludwig-Maximilians-Universität München; Dr. R. Wedlich-Söldner, Max-Planck-Institut für Biochemie, Martinsried)
- 11/2009 - 05/2010 Diplomarbeit: Untersuchung kommensurabler und inkommensurabel modulierter Strukturvarianten modulierter Strukturvarianten von $Sr_5Al_{5+x}Si_{21-x}N_{35-x}O_{2+x} \cdot Eu^{2+}$ ($x \approx 0$) mittels Röntgenbeugung und Transmissionselektronenmikroskopie (PD Dr. O. Oeckler, Ludwig-Maximilians-Universität München)
- 08/2008 - 09/2008 Synthese und Charakterisierung von Polymer Brushes
Prof. Dr. Dr. B. Rieger, Technische Universität München
- 04/2008 - 07/2008 Synthese mesoporöser Silicapartikel unter Verwendung neuartiger Polymere
Prof. Dr. T. Bein, Ludwig-Maximilians-Universität München
- 2007 Röntgenbeugungs- und transmissionselektronenmikroskopische Untersuchungen an Oxonitridosilicaten mit irregulären Strukturen
Prof. Dr. W. Schnick, Ludwig-Maximilians-Universität München

Klinische und andere Erfahrungen

- 02/2010 - 01/2011 Praktisches Jahr an der Ludwig-Maximilians-Universität München:
2 Monate Viszeral- und Thoraxchirurgie, 2 Monate Neurochirurgie, 4 Monate Innere Medizin, 4 Monate Pathologie

03/2009	Famulatur: Hämatologie/Onkologie (Ludwig-Maximilians-Universität München)
03/2008	Famulatur: Nephrologisches Team (Mount Sinai Hospital, New York City, USA)
02/2008	Famulatur: Innere Medizin (Ludwig-Maximilians-Universität München)
09/2007	Famulatur: Nephrologische Ambulanz Prof. Dr. M. Fischereeder, Ludwig-Maximilians-Universität München
08/2007	Famulatur: Radiologie (Ludwig-Maximilians-Universität München)
08/2005 - 09/2005	Pflegepraktikum: Hospital Salgado Filho, Rio de Janeiro, Brasilien
08/2004 - 09/2004	Pflegepraktikum: Universitätsklinikum, Alcalá de Henares, Spanien
2001 - 2002	Anderer Dienst im Ausland: Behindertenwerkstätten, Madrid, Spanien

Publikationen (peer-reviewed)

- (2) H. Koss, W. Schnick, P. Schmidt, O. Oeckler. *Investigation of incommensurate structure variants of $Sr_5Al_{5+x}Si_{21-x}N_{35-x}O_{2+x} \cdot Eu^{2+}$ ($x \approx 0$) by means of transmission electron microscopy. Appl. Cryst., in Vorbereitung.*
- (1) O. Oeckler, J. Kechele, H. Koss, P. Schmidt, W. Schnick. *$Sr_5Al_{5+x}Si_{21-x}N_{35-x}O_{2+x} \cdot Eu^{2+}$ ($x \approx 0$) - a Novel Green Phosphor for White Light pLEDs with a Disordered Intergrowth Structure. Chem. Eur. J. 2009, 15, 5311.*

Konferenzbeiträge

- (3) O. Oeckler, M. Seibald, J. A. Kechele, F. Stadler, T. Rosenthal, H. Koss, W. Schnick. *Real-structure effects of luminescent layered oxonitridosilicates. 26th European Crystallographic Meeting, Darmstadt 2010.*
- (2) J. A. Kechele, O. Oeckler, H. Koss, P.J. Schmidt, W. Schnick. *$Sr_5Al_{5+x}Si_{21-x}N_{35-x}O_{2+x} \cdot Eu^{2+}$ ($x \approx 0$): a disordered intergrowth structure with excellent luminescent properties. 12th European Conference on Solid State Chemistry, Münster 2009.*
- (1) O. Oeckler, J. A. Kechele, F. Stadler, T. Rosenthal, H. Koss, W. Schnick. *Crystal chemistry of disordered layer-like oxonitridosilicates. 24th European Crystallographic Meeting, Marrakesch 2007. Preis für das beste Poster.*

Sprachkenntnisse

Deutsch (Muttersprache)
 Englisch (TOEFL iBT: 110 Punkte, fließend)
 Spanish (fließend)
 Französisch (sichere Basis)
 Portugiesisch (sichere Basis)

Stipendien

Wellcome Trust MPhil/PhD-Stipendium (2011-2015, \approx 143.000 €)
 Friedrich Naumann Stiftung für die Freiheit (2006-2011, ideelle Förderung und \approx 5200 €)
 Jubiläumstipendium des Verbandes der Chemischen Industrie (2002-2004, \approx 10.000 €)
 e-fellows.net (seit 2002, \approx 1500 €)

Interessen

Klavier spielen (Klassik, Jazz)
 Salsa tanzen
 Politik

London, 18. Februar 2012

Dipl.-Chem. Hans Koss

6 References

1. Straub, F.B., *Actin*. Stud. Inst. Med. Chem. Univ. Szeged, 1942. **II**: p. 3-15.
2. Szent-Györgyi, A., Stud. Inst. Med. Chem. Univ. Szeged, 1942. **I**: p. 67.
3. Pollard, T.D. and J.A. Cooper, *Actin, a Central Player in Cell Shape and Movement*. Science, 2009. **326**(5957): p. 1208-1212.
4. Chhabra, E.S. and H.N. Higgs, *The many faces of actin: Matching assembly factors with cellular structures*. Nature Cell Biology, 2007. **9**(10): p. 1110-1121.
5. Galletta, B.J. and J.A. Cooper, *Actin and endocytosis: mechanisms and phylogeny*. Current Opinion in Cell Biology, 2009. **21**(1): p. 20-27.
6. Weisman, L.S., *Organelles on the move: insights from yeast vacuole inheritance*. Nature Reviews Molecular Cell Biology, 2006. **7**(4): p. 243-252.
7. Irazoqui, J.E. and D.J. Lew, *Polarity establishment in yeast*. Journal of Cell Science, 2004. **117**(11): p. 2169-2171.
8. Pruyne, D., et al., *Stable and dynamic axes of polarity use distinct formin isoforms in budding yeast*. Molecular Biology of the Cell, 2004. **15**(11): p. 4971-4989.
9. Pollard, T.D. and G.G. Borisy, *Cellular motility driven by assembly and disassembly of actin filaments*. Cell, 2003. **112**(4): p. 453-465.
10. Le Clainche, C. and M.F. Carrier, *Regulation of actin assembly associated with protrusion and adhesion in cell migration*. Physiological Reviews, 2008. **88**(2): p. 489-513.
11. Carballido-Lopez, R., *The bacterial actin-like cytoskeleton*. Microbiology and Molecular Biology Reviews, 2006. **70**(4): p. 888-909.
12. Pollard, T.D., *Polymerization of ADP-Actin*. Journal of Cell Biology, 1984. **99**(3): p. 769-777.
13. De la Cruz, E.M., et al., *Polymerization and structure of nucleotide-free actin filaments*. Journal of Molecular Biology, 2000. **295**(3): p. 517-526.
14. Dominguez, R., *Actin filament nucleation and elongation factors - structure-function relationships*. Critical Reviews in Biochemistry and Molecular Biology, 2009. **44**(6): p. 351-366.
15. Kasai, M., F. Oosawa, and S. Asakura, *Cooperative nature of G-F transformation of actin*. Biochimica Et Biophysica Acta, 1962. **57**(1): p. 22-31.
16. Wegner, A. and J. Engel, *Kinetics of cooperative association of actin to actin-filaments*. Biophysical Chemistry, 1975. **3**(3): p. 215-225.
17. Sept, D. and J.A. McCammon, *Thermodynamics and kinetics of actin filament nucleation*. Biophysical Journal, 2001. **81**(2): p. 667-674.
18. Kinoshita, H.J., et al., *Actin filament barbed end elongation with nonmuscle MgATP-actin and MgADP-actin in the presence of profilin*. Biochemistry, 2002. **41**(21): p. 6734-6743.
19. Whalen, R.G., G.S. Butlerbrowne, and F. Gros, *Protein synthesis and actin heterogeneity in calf muscle-cells in culture*. Proceedings of the National Academy of Sciences of the United States of America, 1976. **73**(6): p. 2018-2022.
20. Garrels, J.I. and W. Gibson, *Identification and characterization of multiple forms of actin*. Cell, 1976. **9**(4): p. 793-805.
21. Kasai, M., F. Oosawa, and S. Asakura, *G-F Equilibrium in Actin Solutions under Various Conditions*. Biochimica Et Biophysica Acta, 1962. **57**(1): p. 13-21.
22. Pardee, J.D. and J.A. Spudich, *Mechanism of K+-Induced Actin Assembly*. Journal of Cell Biology, 1982. **93**(3): p. 648-654.
23. Frieden, C., *Polymerization of Actin - Mechanism of the Mg-2+-Induced Process at Ph-8 and 20-Degrees-C*. Proceedings of the National Academy of Sciences of the United States of America-Biological Sciences, 1983. **80**(21): p. 6513-6517.

24. Oda, T., et al., *The nature of the globular-to fibrous-actin transition*. Nature, 2009. **457**(7228): p. 441-445.
25. Zimmerle, C.T. and C. Frieden, *Effect of Ph on the Mechanism of Actin Polymerization*. Biochemistry, 1988. **27**(20): p. 7766-7772.
26. Maruyama, K. and K. Tsukagoshi, *Effects of Kcl, Mgcl2, and Cacl2 Concentrations on the Monomer-Polymer Equilibrium of Actin in the Presence and Absence of Cytochalasin-D*. Journal of Biochemistry, 1984. **96**(3): p. 605-611.
27. Pollard, T.D. and M.S. Mooseker, *Direct measurement of actin polymerization rate constants by electron microscopy of actin filaments nucleated by isolated mico villus cores*. Journal of Cell Biology, 1981. **88**(3): p. 654-659.
28. Bonder, E.M., D.J. Fishkind, and M.S. Mooseker, *Direct measurement of critical concentrations and assembly rate constants at the 2 ends of an actin filament*. Cell, 1983. **34**(2): p. 491-501.
29. Dominguez, R., *Actin-binding proteins - a unifying hypothesis*. Trends in Biochemical Sciences, 2004. **29**(11): p. 572-578.
30. Yarmola, E.G., S. Parikh, and M.R. Bubb, *Formation and implications of a ternary complex of profilin, thymosin beta(4), and actin*. Journal of Biological Chemistry, 2001. **276**(49): p. 45555-45563.
31. Bamburg, J.R., A. McGough, and S. Ono, *Putting a new twist on actin: ADF/cofilins modulate actin dynamics*. Trends in Cell Biology, 1999. **9**(9): p. 364-370.
32. Quintero-Monzon, O., et al., *Reconstitution and Dissection of the 600-kDa Srv2/CAP Complex - roles for oligomerization and cofilin-actin binding in driving actin turnover*. Journal of Biological Chemistry, 2009. **284**(16): p. 10923-10934.
33. Chesarone, M.A. and B.L. Goode, *Actin nucleation and elongation factors: mechanisms and interplay*. Current Opinion in Cell Biology, 2009. **21**(1): p. 28-37.
34. Pruyne, D., et al., *Role of formins in actin assembly: Nucleation and barbed-end association*. Science, 2002. **297**(5581): p. 612-615.
35. Sagot, I., et al., *An actin nucleation mechanism mediated by Bni1 and profilin*. Nature Cell Biology, 2002. **4**(8): p. 626-631.
36. Otomo, T., et al., *Structural basis of actin filament nucleation and processive capping by a formin homology 2 domain*. Nature, 2005. **433**(7025): p. 488-494.
37. Campellone, K.G. and M.D. Welch, *A nucleator arms race: cellular control of actin assembly*. Nature Reviews Molecular Cell Biology, 2010. **11**(4): p. 237-251.
38. Breitsprecher, D., et al., *Clustering of VASP actively drives processive, WH2 domain-mediated actin filament elongation*. Embo Journal, 2008. **27**(22): p. 2943-2954.
39. Barzik, M., et al., *Ena/VASP proteins enhance actin polymerization in the presence of barbed end capping proteins*. Journal of Biological Chemistry, 2005. **280**(31): p. 28653-28662.
40. Woychik, R.P., et al., *Formins - Proteins Deduced from the Alternative Transcripts of the Limb Deformity Gene*. Nature, 1990. **346**(6287): p. 850-853.
41. Liu, R., et al., *Formins in development: Orchestrating body plan origami*. Biochimica Et Biophysica Acta-Molecular Cell Research, 2010. **1803**(2): p. 207-225.
42. Higgs, H.N. and K.J. Peterson, *Phylogenetic analysis of the formin homology 2 domain*. Molecular Biology of the Cell, 2005. **16**(1): p. 1-13.
43. Goode, B.L. and M.J. Eck, *Mechanism and function of formins in the control of actin assembly*. Annual Review of Biochemistry, 2007. **76**: p. 593-627.
44. Moseley, J.B. and B.L. Goode, *Differential activities and regulation of Saccharomyces cerevisiae formin proteins Bni1 and Bnr1 by Bud6*. Journal of Biological Chemistry, 2005. **280**(30): p. 28023-28033.
45. Xu, Y.W., et al., *Crystal structures of a formin homology-2 domain reveal a tethered dimer architecture*. Cell, 2004. **116**(5): p. 711-723.

46. Lu, J., et al., *Structure of the FH2 domain of Daam1: Implications for formin regulation of actin assembly*. Journal of Molecular Biology, 2007. **369**(5): p. 1258-1269.
47. Shimada, A., et al., *The core FH2 domain of diaphanous-related formins is an elongated actin binding protein that inhibits polymerization*. Molecular Cell, 2004. **13**(4): p. 511-522.
48. Paul, A. and T. Pollard, *The role of the FHI domain and profilin in formin-mediated actin-filament elongation and nucleation*. Current Biology, 2008. **18**(1): p. 9-19.
49. Rivero, F., et al., *A comparative sequence analysis reveals a common GBD/FH3-FHI-FH2-DAD architecture in formins from Dictyostelium, fungi and metazoa*. BMC Genomics, 2005. **6**(28).
50. Kitayama, C. and T.Q.R. Uyedat, *ForC, a novel type of formin family protein lacking an FHI domain, is involved in multicellular development in Dictyostelium discoideum*. Journal of Cell Science, 2003. **116**(4): p. 711-723.
51. Higgs, H.N., *Formin proteins: a domain-based approach*. Trends in Biochemical Sciences, 2005. **30**(6): p. 342-353.
52. Wedlich-Soldner, R., et al., *Spontaneous cell polarization through actomyosin-based delivery of the Cdc42 GTPase*. Science, 2003. **299**(5610): p. 1231-1235.
53. Dong, Y., D. Pruyne, and A. Bretscher, *Formin-dependent actin assembly is regulated by distinct modes of Rho signaling in yeast*. Journal of Cell Biology, 2003. **161**(6): p. 1081-1092.
54. Evangelista, M., et al., *Bni1p, a yeast formin linking Cdc42p and the actin cytoskeleton during polarized morphogenesis*. Science, 1997. **276**(5309): p. 118-122.
55. Otomo, T., et al., *Crystal Structure of the Formin mDial in Autoinhibited Conformation*. Plos One, 2010. **5**(9).
56. Otomo, T., et al., *Structural basis of Rho GTPase-mediated activation of the formin mDial*. Molecular Cell, 2005. **18**(3): p. 273-281.
57. Moseley, J.B., et al., *A conserved mechanism for Bni1- and mDial-induced actin assembly and dual regulation of Bni1 by Bud6 and profilin*. Molecular Biology of the Cell, 2004. **15**(2): p. 896-907.
58. Zigmond, S.H., et al., *Formin leaky cap allows elongation in the presence of tight capping proteins*. Current Biology, 2003. **13**(20): p. 1820-1823.
59. Li, F. and H.N. Higgs, *The mouse formin mDial is a potent actin nucleation factor regulated by autoinhibition*. Current Biology, 2003. **13**(15): p. 1335-1340.
60. Kovar, D.R., et al., *Control of the assembly of ATP- and ADP-actin by formins and profilin*. Cell, 2006. **124**(2): p. 423-435.
61. Kovar, D.R. and T.D. Pollard, *Insertional assembly of actin filament barbed ends in association with formins produces piconewton forces*. Proceedings of the National Academy of Sciences of the United States of America, 2004. **101**(41): p. 14725-14730.
62. Paul, A.S. and T.D. Pollard, *Review of the Mechanism of Processive Actin Filament Elongation by Formins*. Cell Motility and the Cytoskeleton, 2009. **66**(8): p. 606-617.
63. Vavylonis, D., et al., *Model of formin-associated actin filament elongation*. Molecular Cell, 2006. **21**(4): p. 455-466.
64. Petrella, E.C., et al., *Structural requirements and thermodynamics of the interaction of proline peptides with profilin*. Biochemistry, 1996. **35**(51): p. 16535-16543.
65. Schmidt, R.F., G. Thews, and F. Lang, *Physiologie des Menschen*. 28th ed. 2000, Berlin and Heidelberg: Springer Verlag.
66. Coulibaly, B., et al., *Lethal injection of potassium chloride: first description of the pathological appearance of organs*. Journal of Applied Toxicology, 2010. **30**(4): p. 378-380.

67. Jones, R.P. and G.M. Gadd, *Ionic Nutrition of Yeast - Physiological-Mechanisms Involved and Implications for Biotechnology*. Enzyme and Microbial Technology, 1990. **12**(6): p. 402-418.
68. Petrezselyova, S., J. Zahradka, and H. Sychrova, *Saccharomyces cerevisiae BY4741 and W303-1A laboratory strains differ in salt tolerance*. Fungal Biology, 2010. **114**(2-3): p. 144-150.
69. Megnet, R., *Mutants of Yeast Schizosaccharomyces Pombe Requiring High Concentration of Potassium*. Experientia, 1964. **20**(11): p. 638-639.
70. Conway, E.J. and M. Downey, *pH values of the yeast cell*. Biochemical Journal, 1950. **47**(3): p. 355-360.
71. Navarrete, C., et al., *Lack of main K plus uptake systems in Saccharomyces cerevisiae cells affects yeast performance in both potassium-sufficient and potassium-limiting conditions*. Fems Yeast Research, 2010. **10**(5): p. 508-517.
72. Mulet, J.M., et al., *A novel mechanism of ion homeostasis and salt tolerance in yeast: the Hal4 and Hal5 protein kinases modulate the Trk1-Trk2 potassium transporter*. Molecular and Cellular Biology, 1999. **19**(5): p. 3328-3337.
73. Drenckhahn, D. and T.D. Pollard, *Elongation of Actin-Filaments Is a Diffusion-Limited Reaction at the Barbed End and Is Accelerated by Inert Macromolecules*. Journal of Biological Chemistry, 1986. **261**(27): p. 2754-2758.
74. Grazi, E., A. Aleotti, and A. Ferri, *Characterization of the ATG-G-Actin Aggregates Formed at Low Kcl Concentration*. Biochemical Journal, 1984. **219**(1): p. 273-276.
75. Zimmerle, C.T. and C. Frieden, *Effect of Temperature on the Mechanism of Actin Polymerization*. Biochemistry, 1986. **25**(21): p. 6432-6438.
76. Lichko, L.P., L.A. Okorokov, and I.S. Kulaev, *Participation of Vacuoles in Regulation of Levels of K⁺, Mg²⁺ and Ortho-Phosphate Ions in Cytoplasm of the Yeast Saccharomyces-Carlsbergensis*. Archives of Microbiology, 1982. **132**(3): p. 289-293.
77. Rodriguez-Navarro, A., *Potassium transport in fungi and plants*. Biochimica Et Biophysica Acta-Reviews on Biomembranes, 2000. **1469**(1): p. 1-30.
78. Yu, J.H., et al., *Cortical actin dynamics driven by formins and myosin V*. Journal of Cell Science, 2011. **124**(9): p. 1533-1541.
79. DeWard, A.D., et al., *The role of formins in human disease*. Biochimica Et Biophysica Acta-Molecular Cell Research, 2010. **1803**(2): p. 226-233.
80. Pellman, D., N.J. Ganem, and Z. Storchova, *Tetraploidy, aneuploidy and cancer*. Current Opinion in Genetics & Development, 2007. **17**(2): p. 157-162.
81. Gundersen, G.G. and F. Bartolini, *Formins and microtubules*. Biochimica Et Biophysica Acta-Molecular Cell Research, 2010. **1803**(2): p. 164-173.
82. Olson, M.F. and E. Sahai, *The actin cytoskeleton in cancer cell motility*. Clinical & Experimental Metastasis, 2009. **26**(4): p. 273-287.
83. Narumiya, S., M. Tanji, and T. Ishizaki, *Rho signaling, ROCK and mDia1, in transformation, metastasis and invasion*. Cancer and Metastasis Reviews, 2009. **28**(1-2): p. 65-76.
84. Wehrle-Haller, B. and B.A. Imhof, *Actin, microtubules and focal adhesion dynamics during cell migration*. International Journal of Biochemistry & Cell Biology, 2003. **35**(1): p. 39-50.
85. Lee, S.J., et al., *Diaphanous-Related Formin 2 and Profilin I Are Required for Gastrulation Cell Movements*. Plos One, 2008. **3**(10).
86. Alberts, A.S., et al., *Dia-interacting protein modulates formin-mediated actin assembly at the cell cortex*. Current Biology, 2007. **17**(7): p. 579-591.

87. Freeman, M.R., et al., *Oncosome Formation in Prostate Cancer: Association with a Region of Frequent Chromosomal Deletion in Metastatic Disease*. *Cancer Research*, 2009. **69**(13): p. 5601-5609.
88. Yayoshi-Yamamoto, S., I. Taniuchi, and T. Watanabe, *FRL, a novel formin-related protein, binds to Rac and regulates cell motility and survival of macrophages*. *Molecular and Cellular Biology*, 2000. **20**(18): p. 6872-6881.
89. Favaro, P.M.B., et al., *Human leukocyte formin: a novel protein expressed in lymphoid malignancies and associated with Akt*. *Biochemical and Biophysical Research Communications*, 2003. **311**(2): p. 365-371.
90. Siminovitch, K.A., et al., *The mDial Formin Is Required for Neutrophil Polarization, Migration, and Activation of the LARG/RhoA/ROCK Signaling Axis during Chemotaxis*. *Journal of Immunology*, 2009. **182**(6): p. 3837-3845.
91. Lodish, H.F., P. Ji, and S.R. Jayapal, *Enucleation of cultured mouse fetal erythroblasts requires Rac GTPases and mDia2*. *Nature Cell Biology*, 2008. **10**(3): p. 314-321.
92. Horiuchi, H., et al., *Biochemical characterization of the Rho GTPase-regulated actin assembly by diaphanous-related formins, mDia1 and daam1, in platelets*. *Journal of Biological Chemistry*, 2008. **283**(13): p. 8746-8755.
93. Herold, G., *Innere Medizin*. 2010, Gerd Herold Verlag: Köln. p. 98.
94. Hasle, H., et al., *The International Prognostic Scoring System (IPSS) for childhood myelodysplastic syndrome (MDS) and juvenile myelomonocytic leukemia (JMML)*. *Leukemia*, 2004. **18**(12): p. 2008-2014.
95. List, A., et al., *Efficacy of lenalidomide in myelodysplastic syndromes*. *New England Journal of Medicine*, 2005. **352**(6): p. 549-557.
96. Eisenmann, K.M., et al., *5q-myelodysplastic syndromes: chromosome 5q genes direct a tumor-suppression network sensing actin dynamics*. *Oncogene*, 2009. **28**(39): p. 3429-3441.
97. Copeland, J.W. and K.G. Young, *Formins in cell signaling*. *Biochimica et Biophysica Acta - Molecular Cell Research*, 2010. **1803**(2): p. 183-190.
98. Dettenhofer, M., F. Zhou, and P. Leder, *Formin 1-Isoform IV Deficient Cells Exhibit Defects in Cell Spreading and Focal Adhesion Formation*. *Plos One*, 2008. **3**(6).
99. Schirenbeck, A., et al., *The Diaphanous-related formin dDia2 is required for the formation and maintenance of filopodia*. *Nature Cell Biology*, 2005. **7**(6): p. 619-625.
100. WynshawBoris, A., et al., *The role of a single formin isoform in the limb and renal phenotypes of limb deformity*. *Molecular Medicine*, 1997. **3**(6): p. 372-384.
101. Evans, J.A., et al., *Severe acro-renal-uterine-mandibular syndrome*. *American Journal of Medical Genetics*, 2000. **93**(1): p. 67-73.
102. Lynch, E.D., et al., *Nonsyndromic deafness DFNA1 associated with mutation of a human homolog of the Drosophila gene diaphanous*. *Science*, 1997. **278**(5341): p. 1315-1318.
103. Bione, S., et al., *A human homologue of the Drosophila melanogaster diaphanous gene is disrupted in a patient with premature ovarian failure: Evidence for conserved function in oogenesis and implications for human sterility*. *American Journal of Human Genetics*, 1998. **62**(3): p. 533-541.
104. Riedl, J., et al., *Lifeact mice for studying F-actin dynamics*. *Nature Methods*, 2010. **7**(3): p. 168-169.
105. Blanchoin, L. and R. Boujemaa-Paterski, *Inhibitors Target Actin Nucleators*. *Chemistry & Biology*, 2009. **16**(11): p. 1125-1126.
106. Arkin, M.R. and A. Whitty, *The road less traveled: modulating signal transduction enzymes by inhibiting their protein-protein interactions*. *Current Opinion in Chemical Biology*, 2009. **13**(3): p. 284-290.

107. Wells, J.A. and C.L. McClendon, *Reaching for high-hanging fruit in drug discovery at protein-protein interfaces*. Nature, 2007. **450**(7172): p. 1001-1009.
108. Meireles, L.M.C., A.S. Domling, and C.J. Camacho, *ANCHOR: a web server and database for analysis of protein-protein interaction binding pockets for drug discovery*. Nucleic Acids Research, 2010. **38**: p. W407-W411.
109. Lipinski, C.A., et al., *Experimental and computational approaches to estimate solubility and permeability in drug discovery and development settings*. Advanced Drug Delivery Reviews, 1997. **23**(1-3): p. 3-25.
110. Pollard, T.D., et al., *Characterization of two classes of small molecule inhibitors of Arp2/3 complex*. Nature, 2009. **460**(7258): p. 1031-U121.
111. Rizvi, S.A., et al., *Identification and Characterization of a Small Molecule Inhibitor of Formin-Mediated Actin Assembly*. Chemistry & Biology, 2009. **16**(11): p. 1158-1168.
112. Baell, J.B., *Observations on screening-based research and some concerning trends in the literature*. Future Medicinal Chemistry, 2010. **2**(10): p. 1529-1546.
113. Gauvin, T.J., et al., *Isoform-selective chemical inhibition of mDia-mediated actin assembly*. Biochemistry, 2009. **48**(40): p. 9327-9329.
114. Zimmermann, G.R., J. Lehar, and C.T. Keith, *Multi-target therapeutics: when the whole is greater than the sum of the parts*. Drug Discovery Today, 2007. **12**(1-2): p. 34-42.
115. Neuweiler, H., et al., *Dynamics of unfolded polypeptide chains in crowded environment studied by fluorescence correlation spectroscopy*. Journal of Molecular Biology, 2007. **365**(3): p. 856-869.
116. Riedl, J., et al., *Lifeact: a versatile marker to visualize F-actin*. Nature Methods, 2008. **5**(7): p. 605-607.
117. Kovar, D.R., et al., *The fission yeast cytokinesis formin Cdc12p is a barbed end actin filament capping protein gated by profilin*. Journal of Cell Biology, 2003. **161**(5): p. 875-887.
118. Kudla, G., et al., *Coding-Sequence Determinants of Gene Expression in Escherichia coli*. Science, 2009. **324**(5924): p. 255-258.
119. Spudich, J.A. and S. Watt, *Regulation of Rabbit Skeletal Muscle Contraction .I. Biochemical Studies of Interaction of Tropomyosin-Troponin Complex with Actin and Proteolytic Fragments of Myosin*. Journal of Biological Chemistry, 1971. **246**(15): p. 4866-4871.
120. Schmoller, K.M., et al., *Fragmentation Is Crucial for the Steady-State Dynamics of Actin Filaments*. Biophysical Journal, 2011. **101**(4): p. 803-808.
121. Fass, J., et al., *Stochastic simulation of actin dynamics reveals the role of annealing and fragmentation*. Journal of Theoretical Biology, 2008. **252**(1): p. 173-183.
122. Andrianantoandro, E., et al., *Kinetic mechanism of end-to-end annealing of actin filaments*. Journal of Molecular Biology, 2001. **312**(4): p. 721-730.
123. Mackerell, A.D., *Empirical force fields for biological macromolecules: Overview and issues*. Journal of Computational Chemistry, 2004. **25**(13): p. 1584-1604.
124. Dolinsky, T.J., et al., *PDB2PQR: an automated pipeline for the setup of Poisson-Boltzmann electrostatics calculations*. Nucleic Acids Research, 2004. **32**: p. W665-W667.
125. Dolinsky, T.J., et al., *PDB2PQR: expanding and upgrading automated preparation of biomolecular structures for molecular simulations*. Nucleic Acids Research, 2007. **35**: p. W522-W525.
126. Li, H., A.D. Robertson, and J.H. Jensen, *Very fast empirical prediction and rationalization of protein pK(a) values*. Proteins-Structure Function and Bioinformatics, 2005. **61**(4): p. 704-721.

127. Baker, N.A., et al., *Electrostatics of nanosystems: Application to microtubules and the ribosome*. Proceedings of the National Academy of Sciences of the United States of America, 2001. **98**(18): p. 10037-10041.
128. Schutz, C.N. and A. Warshel, *What are the dielectric "constants" of proteins and how to validate electrostatic models?* Proteins-Structure Function and Genetics, 2001. **44**(4): p. 400-417.
129. Neves-Petersen, M.T. and S.B. Petersen, *Protein electrostatics: A review of the equations and methods used to model electrostatic equations in biomolecules - Applications in biotechnology*. Biotechnology Annual Review, Vol 9, 2003. **9**: p. 315-395.
130. Bayandorian, H., et al., *APBSCommand Software 2.2.0 Documentation* (http://mccammon.ucsd.edu/pmv_apbs/#Introduction).